

Inverting In-situ Anisotropy in Global Subduction Slabs Using Deep Earthquakes and Imaging Binary Mixtures and Fractures

by
Jiaxuan Li

A dissertation submitted to the Department of Earth and Atmospheric Sciences
College of Natural Sciences and Mathematics
in partial fulfillment of the requirements for the degree of

DOCTOR OF PHILOSOPHY

in Geophysics

Chair of Committee: Yingcai Zheng

Committee Member: Hua-wei Zhou

Committee Member: Leon Thomsen

Committee Member: Thomas Lapen

Committee Member: Chengbin Peng

University of Houston

May 2020

Copyright 2020, Jiaxuan Li

Acknowledgments

I feel so fortunate to meet my advisor Dr. Yingcai Zheng. He is always patient and available for help with any questions I have. He is so smart and has very sharp and unique intuition on research problems in many different fields. I always feel benefited a lot after discussing research problems with him. He is always willing to provide firm support to any difficulties I had. And he always respects my decision as long as it is beneficial to my career development. He trains student in a unique way. He encourages us to do novel research, make presentations, write papers, read proposals and write proposals, during which process I feel I have built up knowledge and gained so much invaluable experience. I cannot express my gratitude enough to his advising.

I want to express my gratitude to my committee member Dr. Leon Thomsen for his support and many fruitful discussions of my research. I also want to thank Dr. Leon Thomsen for helping me review my thesis and providing many great comments and suggestions. I still remember when my paper had been rejected by three journals, he encouraged me that 'It will take some time for people to accept new but good things'. I am thankful to Dr. Hua-Wei Zhou for not only many enlightened suggestions on my research, but also many instructions on how to be 'professional' in my career. I sincerely thank Dr. Tom Lapen for his support and contributions to my research on the interpretation of my results about deep earthquakes. I am also thankful to Dr. Chengbin Peng, for providing useful suggestions during my proposal and opportunities to some other interesting research.

I want to express my gratitude to Dr. Xinding Fang for his many help on the finite-difference modeling. Dr. Fang is a very reliable collaborator and always responds very quickly on research problems. I would like to thank Dr. Jonny Wu for his help on providing tomography dataset that is helpful to my research. I would like to thank Dr. Hao Hu for many effective helps on solving programming issues and discussing research problems. And I would like to thank all my friends for the joyful days we experienced together in Houston.

My deepest gratitude goes to my parents for their consistent support on my study abroad. And I am so grateful to my wife Yuhan for her deep love and firm support, and for our cute son Qingning.

ABSTRACT

Since 1970, it has been recognized that a large portion of deep earthquakes, including intermediate-depth (100~300km in depth) and deep-focus (>300km depth) deep earthquakes are found to radiate seismic energy differently (with non-double-couple radiation patterns). Motivated by these observations, I proposed and examined a hypothesis that the deep earthquakes are caused by shear faulting in a tilted transversely isotropic medium to produce these non-double-couple radiation patterns. I used the moment tensors from Global CMT catalog to invert for the in-situ anisotropic structure for 22 deep earthquake groups in 6 global subduction slabs. I found that the anisotropy enabled systematic production of the non-double-couple radiation patterns with simple shear faulting. In most studied regions (for both depth between 100 km~300 km and >300km), the inverted TTI symmetry axes are almost perpendicular to the local slab interface. Among all the anisotropy parameters, the *SH*-wave anisotropy is best determined and has a typical value of 25% (5%-46%) which is strong. The inferred anisotropy can systematically explain the non-double-couple radiation pattern without invoking exotic source processes.

The second topic in my thesis is concerning the mixing of heterogeneities of variable seismic velocities. The Earth's mantle has small scale heterogeneities caused by incomplete mixing of different rock constituents. Using the power spectrum of the Earth's heterogeneities obtained in observations, I developed a novel method to invert for the volumetric proportion and velocities of the two mixing endmembers and to reconstruct the stochastic mixing structure for a binary mixing scenario. The method should find wide applications in many branches of geosciences.

The third topic is on applying a novel machine learning algorithm to identify discrete fractures from the double-beam interference images. The ability to obtain discrete fracture network in space is a significant improvement over the traditional double-beam method which can only give average fracture orientation and density parameters.

Table of Contents

Acknowledgments.....	iii
ABSTRACT	v
Table of Contents.....	vii
List of Tables.....	xi
List of Figures	xii
1 Deep earthquakes hosted in highly anisotropic rock fabric of subducting slabs.....	1
1.1 Introduction	1
1.2 Methods.....	4
1.2.1 Theory	4
1.2.2 Decomposition of moment tensor	5
1.2.3 Inverting the source region anisotropic parameters using moment tensors:	6
1.2.4 Elastic tensor in a TTI medium.....	8
1.2.5 Two-step in situ anisotropy inversion using earthquake moment tensors	10
1.3 Synthetic tests of the inversion method.....	12
1.4 Strong in-situ anisotropy revealed by deep earthquake moment tensors in six global subduction zones	15
1.4.1 Data selection.....	15

1.4.2	Inverted anisotropy around deep earthquakes.....	16
1.4.3	Anisotropy around intermediate-depth deep earthquakes.....	27
1.4.4	Anisotropy around deep-focus deep earthquakes	28
1.4.5	Rock physics model for large shear anisotropy	31
1.4.6	Relationship between moment magnitude and f_{CLVD} values.....	31
1.5	A regional study using F-net moment tensors	34
1.6	Full moment tensor in a transversely isotropic medium	40
1.6.1	Relationship between ISO and CLVD	40
1.6.2	Deviatoric part of the moment tensor	43
1.7	Discussion.....	46
1.8	Conclusions	48
2	Effects of Heterogeneity, Anisotropy and Station Coverage on Moment Tensor Inversion of Deep Earthquakes.....	50
2.1	Introduction	50
2.2	Methods:	52
2.2.1	Model Setup	52
2.2.2	Inversion Methods.....	56
2.3	Numerical Results	58
2.3.1	Case 1: Perfect station coverage	58
2.3.2	Case 2: Stations only in the lower hemisphere	60
2.3.3	Case 3: Azimuth-biased station coverage	62

2.3.4	Case 4: Same station distribution as Case 3 with Green’s function considering slab effects	63
2.4	Discussion.....	64
2.5	Conclusions.....	67
3	Effect of strong intra-slab anisotropic structure on subduction zone shear-wave-splitting measurements.....	69
3.1	Introduction.....	69
3.2	Methods.....	70
3.2.1	Solution of Green-Christoffel equation.....	70
3.2.2	Propagator matrix in layered medium.....	73
3.3	Numerical results	76
3.4	Conclusions.....	80
4	Generation of a stochastic binary field that fits a given heterogeneity power spectrum	82
4.1	Summary.....	82
4.2	Introduction.....	82
4.3	Methods.....	84
4.3.1	Definition of heterogeneity power spectrum and two-point correlation function.	84
4.3.2	Problem statement and binary field construction.....	85

4.3.3	Step1: Determination of velocities and volume fractions of the mixing endmembers.....	86
4.3.4	Step2: Determination of the stochastic structure of binary-mixing field.....	88
4.4	Examples.....	90
4.4.1	Gaussian Type:.....	91
4.4.2	von Karman Type:	94
4.5	Discussion and Conclusions.....	97
5	Physics-Guided Machine Learning Identification of Discrete Fractures From Double Beam Images	99
5.1	Summary.....	99
5.2	Introduction	99
5.3	Methods.....	102
5.3.1	Review of fracture characterization using the DB method	102
5.3.2	Translation of DBI into DFN using neural networks.....	106
5.4	Examples	107
5.4.1	Simple example for DBI obtained by Born scattering	107
5.4.2	Example for DBI obtained by finite-difference modeling	112
5.5	Conclusions	114
6	Bibliography.....	116

List of Tables

Table 1.1 Inverted γ, σ , TTI symmetry axes orientation, and number of earthquakes used in inversion for all 22 studied groups. The angles, θ and ϕ , include the mean value and standard error calculated from 50 bootstrap samples. The γ and σ show the mean values and standard errors $d\gamma$ and $d\sigma$ calculated from the results of 100 bootstrap samples. The last column shows whether there exists ambiguity in the orientation of TTI symmetry axes. None represents no ambiguity. The angles in the last column represent an alternative orientation of the TTI symmetry axis. For MJK2, the local minimum/global minimum is about ~89%. For TG1, the local minimum/global minimum is about ~96%. .
.....26

Table 1.2 Inverted γ, σ , TTI symmetry axes orientation, and the number of earthquakes used in inversion for all 25 studied groups. The γ and σ show the mean values and standard errors $d\gamma$ and $d\sigma$ calculated from the results of 100 bootstrap samples. The last column shows whether there exists ambiguity in the orientation of TTI symmetry axes.....39

List of Figures

Figure 1.1 (a) Histogram of f_{CLVD} component for 10,909 moment tensors from the G CMT catalog for earthquakes with a depth greater than 50 km from 1976 to 2013. Only about 28% moment tensors have $|f_{CLVD}| < 0.05$ and about 18% have $|f_{CLVD}| > 0.2$. (b)

Histogram of f_{CLVD} for 1,057 moment tensors used in this study. About 41% moment tensors have CLVD component smaller than 0.05.....3

Figure 1.2 Lower hemispheric stereographic projection of the normalized misfit $\Delta_1(\theta, \phi)$ in Step 1 with different noise levels (**a**, **b**, **c**). Here ϕ is the azimuth of the anisotropy symmetry axis and θ is 90° subtracting the plunge angle of the axis. These plots show the stereographic projection of misfit for different TTI symmetry axes (θ, ϕ) . The white dot represents the intersection between the true TTI symmetry axis in the model and the lower hemisphere. (**a**) Misfit Δ_1 using moment tensors with no noise. (**b**) Misfit Δ_1 using moment tensors with 10% Gaussian noise. (**c**) Misfit Δ_1 using moment tensors with 20% Gaussian noise.....13

Figure 1.3 Histograms of inverted Thomsen parameters ϵ , γ , δ , and $\epsilon - \delta$ using the bootstrap samples in Step 2 of the synthetic test. I randomly searched for the optimized elastic constants within the searching range of Thomsen parameters and calculated the corresponding Thomsen parameters at the TTI symmetry axis inverted in Step 1. These plots show the histograms of ϵ , γ , δ , and $\epsilon - \delta$ values for the bootstrap method with 100 bootstrap samples. (**a-d**) Histograms of ϵ , γ , δ , and $\epsilon - \delta$ for moment tensors with no noise. (**e-h**) Histograms of ϵ , γ , δ , and $\epsilon - \delta$ for moment tensors with 10% Gaussian

noise. **(i-l)** Histograms of ϵ , γ , δ , and $\epsilon - \delta$ for moment tensors with 20% Gaussian noise.14

Figure 1.4 Global map view of all 6 subduction regions in this study. The colored patches here represent the subducting slab interfaces. The color changing from light green to pink represent depth from shallow to deep. Blue dots represent all 1,057 deep earthquakes used in this study.....16

Figure 1.5 Inverted TTI anisotropy symmetry axes (colored arrowheads) with respect to slab geometry. **(a)**, MJK earthquake groups 1–7. **(b)**, AL groups 1 and 2. **(c)**, TG groups 1–8. **(d)**, VA groups 1 and 2. **(e)**, MO groups 1 and 2. **(f)**, IND group 1. Light green surfaces are the subducting slabs. Gray dashed lines are depth contour lines (every 100 km from the Earth’s surface). Earthquakes (colored dots) are divided into different groups with different colors indexed by the corresponding group numbers shown in the open boxes (intermediate depth) as well as the shaded boxes (deep focus).19

Figure 1.6 **(a-v)** 2-D vertical cross-sections of 22 regions in our study. Each cross-section contains the center and the slab normal for each deep earthquake group. The gray circles represent deep earthquakes projected on the cross-section plane. The bold black lines represent the intersections of the slab interfaces by Gudmundsson and Sambridge (1998) and the cross-section planes. The red arrows represent the projection of inverted TTI anisotropy symmetry axes on the cross-section planes, and the blue arrows represent the normal of the slab interfaces in each region. The background P-wave tomographic model is created from the GAP_P4 Model by Fukao and Obayashi (2013). The color scale is $\pm 1.5\%$ in P-wave velocity perturbation where the red represents slower and blue represents faster regions.20

Figure 1.7 Apparent non-DC events caused by shear dislocations in anisotropic media. **(a)**, Comparison between the observed and synthetic radiation patterns (‘beach ball’ representations of the lower hemispheric stereographic projection of the P-wave initial motion) for eight randomly selected earthquakes in the TG4 group. The grey regions represent outward motion and the white regions represent inward motion. The observed beach balls are from the CMT catalogue. The synthetic beach balls were modelled using the inverted anisotropy and best-fit shear dislocation faulting geometry for each event. The synthetic beach balls fit the observed ones well. **(b)** Cross-plot between the apparent CLVD components of observed moment tensors and those of synthetic moment tensors for all the earthquakes in 22 earthquake groups. Each circle represents one earthquake. The red line is the orthogonal regression line for all 1,057 earthquakes in this study.....21

Figure 1.8 Summary of inverted anisotropy parameters. **(a)** The angles between TTI symmetry axes and the normal directions of the slab interfaces in all studied regions. See Figure 1.5 for groups’ names. **(b)** The anisotropy strength γ in all studied regions. Horizontal lines represent depth ranges of different earthquake groups. **(c)** The anisotropy strength σ in all studied regions. Horizontal lines represent depth ranges of different earthquake groups. **(d)** Relationship between γ and σ . The background gray-colored circle represents the mean earthquake depth in the corresponding group.....22

Figure 1.9 PBT axes (P: maximum compression axis, T: tension axis, B: perpendicular to P and T axes) and inverted anisotropy symmetry axes (red star) plotted on a stereographic projection of the lower hemisphere, for all six deep-focus earthquake groups including: **(a)** MJK6, **(b)** MJK7, **(c)** TG8, **(d)** MO2 **(e)** TG6 and **(f)** TG7. The black solid line represents the slab interface.23

Figure 1.10 Cross plot between inverted (a) γ values and TTI symmetry axis angles and (b) σ values and TTI symmetry axis angles for all 22 groups (black circles) in this study. No clear trends between γ or σ values and angles are found.....24

Figure 1.11 Inversion results of reselected earthquakes following the more strict criteria where the relative error in the moment tensors defined by Vavrycuk (2004) is less than 10%. (a) Comparison between number of reselected earthquakes (New Events) and earthquakes used in this study (Original Events) for all 22 groups. The number of all reselected earthquakes is 762. (b) Comparison of angles between inverted TTI symmetry axes and the corresponding slab normal for reselected earthquakes (New Angles) and earthquakes used in this study (Original Angles) for all 22 groups. (c) Comparison between inverted γ values from reselected earthquakes (New Results) and from earthquakes used in this study (Original Results) for all 22 groups. The mean and median values for new γ values are about 27.5%. (d) Cross plot between apparent CLVD components of observed MTs and those of synthetic MTs for all reselected earthquakes in 22 earthquake groups. The red line is the orthogonal regression line for all 762 reselected earthquakes with a slope of about 0.96. (e) Rose diagram to show angles between P, B, and T axes of the synthetic moment tensors and those of the observed moment tensors for all reselected earthquakes. Those three grey arrows represent the 0° angles between P, B, and T axes of the synthetic moment tensors and those of the observed moment tensors.25

Figure 1.12 Schematic diagram of the origin of anisotropy. The gray dotted line represents our division between intermediate-depth and deep-focus earthquake events; the dark green dashed line represents the 410km phase change boundary. Short blue lines in the downgoing slab represent the inferred fabric in the slab. (a) The red stars represent

intermediate-depth earthquake groups with inverted TTI symmetry axes perpendicular to the slab interface. **(b)** The purple stars represent deep-focus earthquake groups with inverted TTI symmetry axes perpendicular to the slab interface. **(c)** And the black stars represent the deep-focus earthquake groups with TTI symmetry axes parallel to the slab interface.....30

Figure 1.13 Relationship between the moment magnitude and f_{CLVD} value for the selected 1057 deep earthquakes. (a-d) f_{CLVD} histogram of deep earthquakes within different moment magnitude ranges **(a)** M_W between 5.0 and 5.4. **(b)** M_W between 5.4 and 5.8. **(c)** M_W between 5.8 and 6.2. **(d)** M_W between 6.2 and 6.6. **(e)** Probability distribution within different f_{CLVD} - M_W bins. The bin interval for M_W is 0.4 and bin interval for f_{CLVD} is 0.02. Each magenta scatter represents one selected deep earthquake.....33

Figure 1.14 Rectangular fault dimension for different moment magnitude. The red solid line represents the length of the fault. The blue dashed line represents the width of the fault. ...
.....34

Figure 1.15 Intra-slab anisotropy inverted using earthquake moment tensors from the F-net. Earthquakes (colored dots) are clustered into different groups with different colors indexed by the corresponding group numbers shown in the open boxes. Colored arrowheads represent inverted TTI anisotropy symmetry axes. Light green surfaces are the subducting slabs. Gray dashed lines are depth contour lines (every 100km from the Earth's surface).35

Figure 1.16 2-D vertical cross-sections of 25 groups in our preliminary study. Each cross-section contains the center and the slab normal for each deep earthquake group. The gray

circles represent deep earthquakes projected on the cross-section plane. The bold black lines represent the intersections of the slab interfaces (Gudmundsson and Sambridge, 1998) and the vertical cross-section planes. The magenta arrows represent the projection of inverted TTI anisotropy symmetry axes on the cross-section planes, and the green arrows represent the normal of the slab interfaces in each region. The background P-wave tomographic model is created from the GAP_P4 Model by (Fukao and Obayashi, 2013). The color scale is $\pm 1.5\%$ in P-wave velocity perturbation where the red represents slower and blue represents faster regions.37

Figure 1.17 The angles between TTI symmetry axes and the normal direction of slab interfaces in all 25 groups. The plot inside the black box shows the upper hemisphere stereographic projection of TTI symmetry axes (red circles). The center of the plot represents slab normal. Right direction represents the strike of the slab. Upper direction represents the up dipping of the slab. **b)** The anisotropy strength γ in all 25 groups. Horizontal lines represent depth ranges of different earthquake groups.....38

Figure 1.18. Variation of ISO (a) and CLVD (b) with respect to the change of rake angle θ and dipping angle ϕ of a shear slip in the VTI medium. The C_{33} and C_{44} are density normalized to be $100 \text{ km}^2/\text{s}^2$ and $30 \text{ km}^2/\text{s}^2$ The Thomsen parameters are: $\epsilon = 0.05, \gamma = 0.25, \delta = -0.05$43

Figure 1.19. Normalized ratio r calculated for different ϵ and δ and $C_{44}C_{33} = 0.3$. The white dots cover area with $r < 0.85$. For negative δ and large ϵ , the ratio r is close to 1, which means that SV-wave anisotropy almost linearly varies with parameter X2.....46

Figure 1.20 West-East vertical cross section of earthquake events in Japan. Earthquakes are within the region with latitude between 38.5°N to 40.9°N , longitude between 140°E to

143°E. Grey circles represent earthquakes from Japan Meteorological Catalog (JMA) with a magnitude between 1.0 and 6.6 from 1998-01-01 to 2017-12-31. Blue circles represent earthquakes from JMA with a magnitude between 3.0 and 6.6. Red circles represent earthquake events with a magnitude between 3.0 and 6.6 recorded in both JMA and F-net. In cross section, radii of circles indicate earthquake magnitudes. We can clearly see two layers of earthquake events, i.e. the double-Benioff zone.47

Figure 2.1. (a) The source and receiver geometry in FD forward modeling. Red star represents the source. Blues circles represent the receivers. The 441 receivers are evenly distributed on a sphere with a radius of 500km centered at the source. The background $VP = 8km/s$ and $VS=4.5 km/s$. (b) P and S velocities in the heterogeneous slab for model-1, 2, 4, and 5 (Figure 2.2 a, b, d, e). The highest velocities in the slab are $VP = 8.4km/s$ and $VS=4.7 km/s$, which represent about 5% high-velocity anomaly in the coolest part of the slab.53

Figure 2.2. Five different models (only show P wave velocities) with a heterogeneous slab or an anisotropic structure. The dipping angle of the slab is 40°. The red star represents the source location. The size of heterogeneous slab is $100km \times 600km \times 600km$. The anisotropic structure is chosen to be tilted transversely isotropic (TTI) medium, which is described by the VP and VS (same as background VP and VS) along the TTI symmetry axis, and three Thomsen parameters ϵ, γ, δ . In Model-2, 3, and 4, the TTI symmetry axis is perpendicular to the slab interface. In Model-5, the TTI symmetry axis is parallel to the slab interface. For Model-2 and 3, the dimension of the anisotropic patch is $30km \times 30km \times 30km$ and the three Thomsen parameters are $\epsilon = 20\%, \gamma = 20\%, \delta = 0\%$, which represents a strong in-situ anisotropic structure. For model-4, the anisotropic

patch is $150\text{km} \times 150\text{km} \times 20\text{km}$ and the $\varepsilon = 0\%$, $\gamma = 6\%$, $\delta = 0\%$, $\sigma = 0\%$, which represents a weak outside slab anisotropic structure. For Model-5, the $\varepsilon = 0\%$, $\gamma = 5\%$, $\delta = 0\%$, $\sigma = 0\%$, which represents a weakly anisotropic MOW inside the slab. **(a)** Model-1 with only heterogeneous slab. **(b)** Model-2 with only strong anisotropic patch in the source region. **(c)** Model-3 with both heterogeneous slab and strong anisotropic patch in the source region. **(d)** Model-4 with heterogeneous slab and weakly anisotropic patch outside the slab. **(e)** Model-5 with heterogeneous slab and weakly anisotropic MOW inside the slab. **(f)** 2D velocity profile of Model-5. The distance of three tips of MOW A, B, and C to the slab upper interface is 20km, 0km, and 40km.55

Figure 2.3. Lower hemisphere projection of station distributions for three cases. Upper direction represents North and right direction represent East. Red triangles represent receivers in the upper hemisphere, blue triangles represent lower hemisphere. **(a)** Perfect station coverage including all 441 stations. **(b)** 40 stations in the lower hemisphere are randomly selected. The stations are evenly distributed by azimuth and distance. **(c)** Azimuth-biased station coverage with 40 stations in the lower hemisphere in the southern part selected.59

Figure 2.4. Comparison between CLVD components of inverted moment tensors and CLVD components of true moment tensors for 24 earthquake events for five models with perfect station coverage. **(a)** Comparison for Model-1. Inverted CLVD components are very close to the true ones, which are essentially zeros. **(b)** Comparison for Model-2. Inverted CLVD components are close to the true ones. Non-zeros CLVDs are caused by the anisotropic structure in the source region. **(c)** Comparison for Model-3. Inverted CLVD components are still close to the true ones. The error is a bit larger than the results

in Model-2. **(d)** Comparison for Model-4. The results are similar to the ones in Model-1.
(e) Comparison for Model-5. Inverted CLVD components are very close to the true ones.

.....60

Figure 2.5. Comparison between CLVD components of inverted moment tensors and CLVD components of true moment tensors for 24 earthquake events for five models. The moment tensors are inverted using 40 randomly selected stations only in lower hemisphere. For this station coverage, the inverted CLVD components have larger errors for all 4 Models. But the results are still reasonable. **(a-e)** Comparison for Model-1~5. .62

Figure 2.6. Comparison between CLVD components of inverted moment tensors and CLVD components of true moment tensors for 24 earthquake events for five models. The moment tensors are inverted using 40 randomly selected azimuth-biased stations. This poor station distribution contributes large artifacts to the inverted CLVD components. **(a-e)** Comparison for Model-1~5.63

Figure 2.7. Comparison between CLVD components in inverted moment tensors and true CLVDs. I used the same station coverage as the one in Figure 2.6. But I used different Green's function which takes effect of the heterogeneous slab into account. Although a poor station coverage is used, I got an even better result for Model-1 and 4. For Model-3 and 5, the error is decreased a little bit. **(a)** Comparison for Model-1. **(b)** Comparison for Model-3. **(c)** Comparison for Model-4. **(d)** Comparison for Model-5.64

Figure 2.8. **(a-d)** Comparison between the inverted CLVD component in Model-1 and Model-4 for 4 cases. The inverted CLVDs in Model-4 are highly correlated with the ones in Model-1.67

Figure 3.1. Propagator matrix in a two-layered model.75

Figure 3.2 3D modeling of SWS for plane wave propagation through a dipping anisotropic layer. A vertical cross-section showing the anisotropic layer (part of the slab) and incident wave geometry. The slab is dipping to the west. The station (triangle) is 28km west of the trench. The middle layer is 20 km thick and has a tilted transverse isotropy (TTI) anisotropy (with symmetry axis normal to the slab) with the P-wave anisotropy $\varepsilon = 0.3$, the SH-wave anisotropy $\gamma = 0.3$, and the Thomsen $\delta = 0$ (see (1.15) for definition). Along the TTI symmetry axis, its P-wave velocity, V_P is 8.4 km/s and S-wave velocity, V_S is 4.67 km/s. The SV-wave anisotropy σ is about 0.54 calculated using equation (1.16). The upper and lower layers are isotropic and have $V_P=8$ km/s and $V_S=4.45$ km/s. Rock density is set to be uniform (3400kg/m^3) in the whole model.78

Figure 3.3 Lower hemisphere stereographic projection of the upgoing incident SV wave directions (i.e., locations of the blue bars) at the station. The orientation of the blue bar represents the projection of fast wave polarization on the ground. The length of blue bars (see the 0.5s scale at the lower right location) represents the traveltime difference between the fast and slow shear waves. The graph inside the black box shows the schematic diagram of the geometry of the slab and incident plane wave with different propagation directions. I did not compute all possible incident angles but only those corresponding to the blue bars.79

Figure 3.4 Seismic rays (SKS) through the Earth from different earthquakes to one seismic station in Japan.80

Figure 4.1. **(a)** A Gaussian correlation function. **(b)** Relationship of binary velocities v_a (red dashed line) and v_b (blue dash-dotted line) with the volume fraction of phase-a ϕ_a for this Gaussian type. The black solid line represents the background velocity v_0 93

Figure 4.2. Gaussian type binary field. **(a)** Comparison of the observed correlation function ($S^{(a)}$, black solid line), initial correlation function (blue dash-dotted line), and final correlation function of the indicator field after 2 million simulated annealing iterations (S^{SA} , red circles); **(b)** Correlation misfit, E (equation (4.16)), with the iteration number; **(c)** Initial random binary velocity with volume fraction $\phi_a = 0.3$ for phase-a. **(d)** Final binary velocity field $V^{(B)}(x,z)$ using SA. **(e)** One realization of the continuous velocity field given the observed $B(r)$ and background velocity v_0 . In **(c)** and **(d)**, the yellow region denotes phase-a and red region denotes phase-b.93

Figure 4.3. **(a)** von Karman correlation function. **(b)** Relationship of binary velocities v_a (red dashed line) and v_b (blue dash-dotted line) with the volume fraction of phase-a ϕ_a for the von Karman type medium. The black solid line represents the background velocity v_0 95

Figure 4.4. von Karman binary field. **(a)** Comparison of the observed correlation function (black solid line), initial correlation function (blue dash-dotted line), and final SA correlation function (red circles) of binary indicator field after 3 million iterations. **(b)** Misfit E (equation (4.16)) with the iteration number. **(c)** Initial random binary velocity

field with volume fraction $\phi_a = 0.3$. **(d)** Final binary-mixing velocity field $V^{(B)}(x, z)$ after 3 million steps of SA. **(e)** One random realization of continuous velocity field given observed $B(r)$ and background velocity v_0 . In **(c)** and **(d)**, the yellow region denotes phase-a and red region denotes phase-b.96

Figure 5.1. Schematic diagram of the DB imaging method. Stars and triangles represent source and receivers respectively. a is the local fracture spacing in the target area. $\hat{\phi}$ the fracture normal direction.104

Figure 5.2. One example of the absolute value of the complex-valued DBI pattern (Hu *et al.*, 2018). **(a)** Map view of the fracture distribution. The horizontal and circled lines represent vertical fractures. Color represents fracture compliance. Two targets blocks T1 and T2 (each target contains two sets of fractures) are selected to generate DBI patterns in **(b)** and **(c)**. The radial direction indicates the scanned fracture spacing a (i.e., 40-120 m), the tangential direction indicates scanned fracture orientation $\hat{\phi}$. If there exists a fracture set within the scanned fracture spacing and orientation range, there will be high-amplitude bright spots which represents the relative magnitude of compliance for this set of fracture. Two picked bright spots indicate two detected sets of fractures.105

Figure 5.3. The architecture of the DBNN. The dropout is applied to both the input layer and hidden layer to avoid overfitting.107

Figure 5.4. Mean square error of predictions for training dataset and test dataset in 5000 epochs during the training process.108

Figure 5.5. Comparison of predicted fractures and true fractures using training dataset for DBNN with one hidden layer, dropout, and activation. Yellow color represents fracture.

Dark blue represents no fracture. Each fracture image has 21×21 pixels. And each pixel has a dimension of 5 meter by 5 meter.109

Figure 5.6. Comparison of predicted fractures and true fractures using test dataset for DBNN with one hidden layer, dropout, and activation. Yellow color represents fracture. Dark blue represents no fracture.110

Figure 5.7. Comparison of predicted fractures and true fractures using training dataset for simpler regression DBNN model. Yellow color represents fracture. Dark blue represents no fracture.111

Figure 5.8. Comparison of predicted fractures and true fractures using test dataset for simpler regression DBNN model. Yellow color represents fracture. Dark blue represents no fracture.112

Figure 5.9 **a)** 3D view of 5-layer model for finite-difference modeling and source (red asterisks) and receiver (blue dots) geometry. Randomly spaced vertical fractures are located in a non-flat layer. **b)** 2D view of 5-layer model with P-wave velocity V_P , S-wave velocity V_S and density ρ .(Hu *et al.*, 2018) **c)** Map view of fracture distribution. The horizontal lines and circles are fractures. Red color represents high fracture compliance. Blue color represents low fracture compliance.113

Figure 5.10 **(a)** True fracture distribution map (21-by-21 target blocks). Yellow color represents fractures. Dark blue represents no fracture. **(b)** Predicted fractures by trained neural network with DBIs obtained from FD modeling data as input.114

1 Deep earthquakes hosted in highly anisotropic rock fabric of subducting slabs

1.1 Introduction

Deep earthquakes are defined as those deeper than ~60km. Below this depth in the Earth, normal mantle rock is ductile due to high temperature and high confining pressure; this inhibits brittle failure at typical mantle strain rates (Hacker *et al.*, 2003). Yet about 30% of the global earthquakes from the International Seismological Centre (ISC) catalog ($m_b \geq 5.3$) are deep earthquakes (Frohlich, 2006) associated with subducting slabs. In addition, a striking characteristic of deep earthquakes is that they radiate seismic energy differently from what would be expected by a planar shear dislocation rupture in a homogenous isotropic medium, producing a “double-couple (DC) radiation pattern” (Knopoff and Randall, 1970; Kuge and Kawakatsu, 1993; Julian *et al.*, 1998; Richardson and Jordan, 2002; Frohlich, 2006; Houston, 2015). Instead, seismic-wave energy radiation produced from most deep earthquakes shows an apparent deviation from the ideal double-couple behavior, called non-DC radiation. This apparent non-DC radiation pattern of *deep earthquakes* has been an ongoing research topic since the early 1970s (Knopoff and Randall, 1970). The non-DC components are ubiquitous for both intermediate-depth and deep-focus earthquakes (Kuge and Kawakatsu, 1993).

Apparent non-DC radiation patterns have previously been explained by *ad hoc* mechanisms for each particular earthquake (or for a set of earthquakes in a local region). In most cases, they were attributed to complex source processes, which include, for example, faulting with multiple sub-faults (Frohlich, 1994; Kuge and Lay, 1994), phase assemblage

changes (Evison, 1963; Kirby, 1987; Green, 2007; Schubnel *et al.*, 2013), and less frequently to lithologic heterogeneities or faulting in an anisotropic medium (Kawasaki and Tanimoto, 1981; Vavrycuk, 2004). While each of these can certainly cause the non-DC radiation, a systematic approach to understanding global non-DC slab earthquakes has been lacking. Vavrycuk (2004) proposed a procedure to use seismic radiation patterns to invert for orthorhombic anisotropy in the Tonga slab but the global application of this idea has not been explored.

In this chapter, I proposed and tested the hypothesis that pure shear-dislocation faulting in an anisotropic medium can systematically generate the observed apparent non-DC radiation patterns globally. In particular, I focused on a particular type of anisotropy with tilted transversely isotropic (TTI) symmetry, because it has the fewest degrees of freedom. A medium with such symmetry could be laminated fabric defined by aligned minerals (such as sheet silicates), and/or lithologic layering. The TTI anisotropy is characterized by five independent elastic constants plus two angles, θ , φ , for the orientation of the symmetry axis (not necessarily related to the slab orientation). The five constants are denoted by the P - and S -wave velocities propagating along the symmetry axis and three Thomsen parameters, ε , γ , and δ (Thomsen, 1986), with ε measuring the P -wave anisotropy, γ the SH -wave anisotropy, and δ affecting both P and SV waves. Equivalently, the anisotropy may be characterized by ε , γ , and σ (the SV -wave anisotropy),

In seismic wave radiation, an earthquake can be equivalently represented by a set of force couples, known as the moment tensor. A general moment tensor can be decomposed into the sum of a DC and a non-DC part, which includes a volumetric component and a Compensated

Linear Vector Dipole (CLVD) component (Knopoff and Randall, 1970; Julian *et al.*, 1998). Since 1982, the Global Centroid-Moment-Tensor Project (CMT; initially known as the Harvard CMT) has been routinely publishing moment tensors inverted from long-period data on earthquakes recorded at seismic stations worldwide (Dziewonski *et al.*, 1981; Julian *et al.*, 1998; Ekström *et al.*, 2012). In the CMT catalog, non-DC components are ubiquitous (Figure 1.1) and they are equivalent to the CLVD components because the volumetric components are assumed to be zero. The strength of the CLVD component is measured by the scalar f_{CLVD} , defined in equation (1.5).

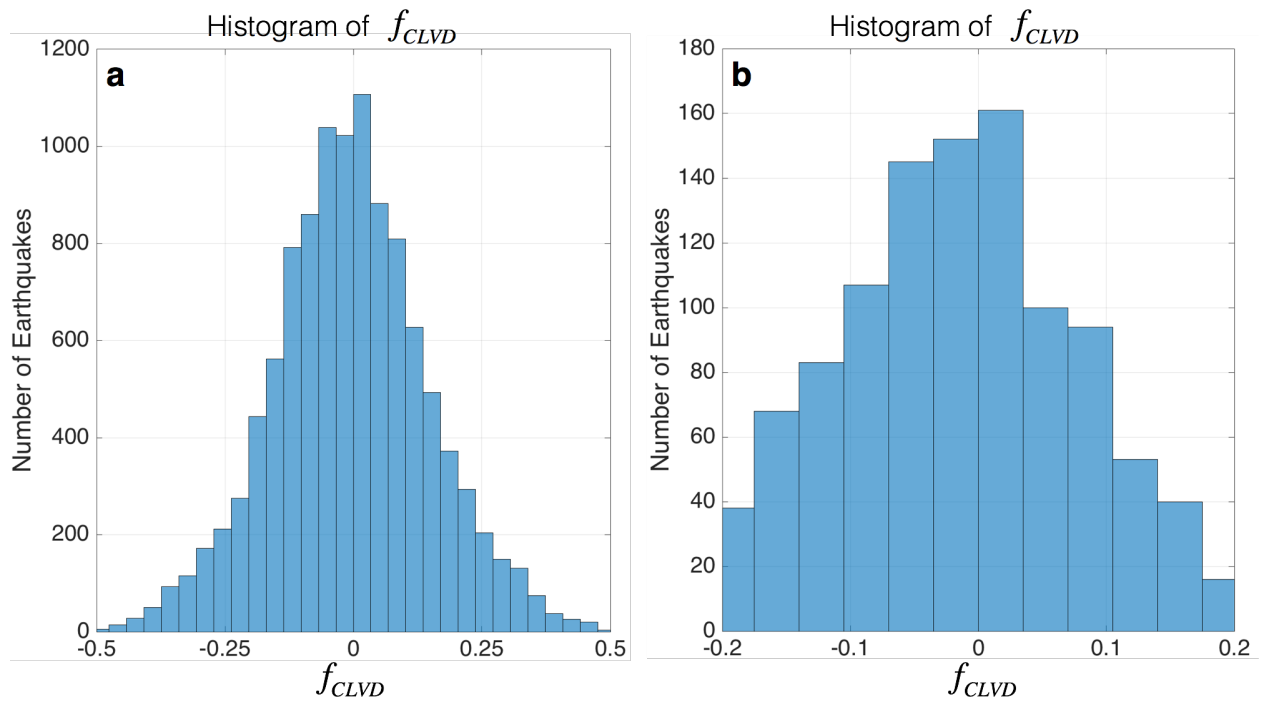


Figure 1.1 (a) Histogram of f_{CLVD} component for 10,909 moment tensors from the G CMT catalog for earthquakes with a depth greater than 50 km from 1976 to 2013. Only about 28% moment tensors have $|f_{CLVD}| < 0.05$ and about 18% have $|f_{CLVD}| > 0.2$. (b) Histogram of f_{CLVD}

for 1,057 moment tensors used in this study. About 41% moment tensors have CLVD component smaller than 0.05.

1.2 Methods

To test our hypothesis, I used the moment tensors from the Global CMT catalog to invert for the *in situ* seismic anisotropy around *deep earthquakes*. The assumptions are:

- (i). deep earthquakes are caused by the shear dislocation faulting mechanism;
- (ii). there is only one common type of TTI anisotropy for a group of earthquakes of neighboring positions in a slab.

1.2.1 Theory

The inversion method is based on the explicit relationship between the moment tensor m_{ij} of an earthquake and the elastic stiffness constants c_{ijkl} :

$$m_{ij} = usc_{ijkl}n_k v_l, \quad i, j, k, l = 1, 2, 3 \quad (1.1)$$

with $i, j, k, l = 1, 2, 3$ representing three spatial directions (Aki and Richards, 2002). Here u is the magnitude of the slip of the dislocation faulting, s is the area of the slippage, n_k is the fault surface unit normal and v_l is the slip unit vector. (Repeated indices imply summation.) This standard theory assumes that the magnitude of u is constant within the area s (although a more realistic theory would assume that u reduces smoothly to zero at the edges of s).

1.2.2 Decomposition of moment tensor

The 3-by-3 moment tensor m_{ij} is symmetric and has three eigenvalues, $|\Lambda_1| \geq |\Lambda_2| \geq |\Lambda_3|$. Without loss of generality, the full moment tensor m_{ij} in its eigen coordinate system can be decomposed into three parts (1.2): the isotropic part, the compensated linear vector dipole part (CLVD) and the double-couple part (DC). The deviatoric part of the moment tensor includes the latter two parts, CLVD and DC.

$$\begin{pmatrix} \Lambda_1 & 0 & 0 \\ 0 & \Lambda_2 & 0 \\ 0 & 0 & \Lambda_3 \end{pmatrix} = \Lambda_{ISO} \begin{pmatrix} 1 & 0 & 0 \\ 0 & 1 & 0 \\ 0 & 0 & 1 \end{pmatrix} + \Lambda_{CLVD} \begin{pmatrix} 2 & 0 & 0 \\ 0 & -1 & 0 \\ 0 & 0 & -1 \end{pmatrix} + \Lambda_{DC} \begin{pmatrix} 1 & 0 & 0 \\ 0 & 0 & 0 \\ 0 & 0 & -1 \end{pmatrix}, \quad (1.2)$$

with:

$$\begin{aligned} \Lambda_{ISO} &= \frac{1}{3}(\Lambda_1 + \Lambda_2 + \Lambda_3) \\ \Lambda_{CLVD} &= -\Lambda_3 + \frac{1}{3}(\Lambda_1 + \Lambda_2 + \Lambda_3). \\ \Lambda_{DC} &= \Lambda_3 - \Lambda_2 \end{aligned} \quad (1.3)$$

For the full moment tensor, I followed the definition for the percentage of ISO, CLVD, and DC proposed by Vavrycuk (2005) as:

$$\begin{aligned} \text{ISO} &= \frac{\Lambda_{ISO}}{|\Lambda_1|} \\ \text{CLVD} &= 2 \frac{\Lambda_{CLVD} - \Lambda_{ISO}}{|\Lambda_1|} (1 - \text{ISO}) . \\ \text{DC} &= 1 - |\text{ISO}| - |\text{CLVD}| \end{aligned} \quad (1.4)$$

Since the isotropic components of moment tensors in the GCMT catalog are set to be zero, f_{CLVD} was used to measure the non-DC departure from the ideal DC case (Julian *et al.*, 1998):

$$f_{CLVD} = \frac{1}{2} \text{CLVD} = -\frac{\Lambda_3}{|\Lambda_1|}. \quad (1.5)$$

The f_{CLVD} ranges from -0.5 to 0.5, with a value 0 for a pure DC source mechanism. The two extreme values ± 0.5 are for pure CLVD source mechanisms. Positive f_{CLVD} corresponds to extensional polarity for major dipole of the CLVD component (Julian *et al.*, 1998).

1.2.3 Inverting the source region anisotropic parameters using moment tensors:

In order to invert for c_{ijkl} using m_{ij} , u and s were set to be scalar 1 (thus m_{ij} is the normalized moment tensor). Equation (1.1) can then be rewritten as:

$$m_{ij} = \frac{1}{2} c_{ijkl} (n_k v_l + n_l v_k) = c_{ijkl} d_{kl}, \quad (1.6)$$

where the tensor:

$$d_{kl} = \frac{1}{2} (n_k v_l + n_l v_k) \quad (1.7)$$

represents the fault geometry. For a pure shear fault, $\text{Trace}(\mathbf{d}) = \mathbf{n} \cdot \mathbf{v} = 0$.

Using the Voigt notation (Helmwein, 2001) to denote the tensors in equation (1.6):

$$\text{Voigt notation: } ij \rightarrow \alpha: 11 \rightarrow 1, 22 \rightarrow 2, 33 \rightarrow 3, 12 \rightarrow 6, 13 \rightarrow 5, 23 \rightarrow 4,$$

the 3-by-3 tensors \mathbf{m} and \mathbf{d} can be rewritten as 6-by-1column matrices \mathbf{M} and \mathbf{D} . The 4-rank elastic tensor \mathbf{c} can be written as a 6-by-6 matrix \mathbf{C} . Equation (1.6) can be rewritten as:

$$\mathbf{M} = \mathbf{CD}, \quad (1.8)$$

where:

$$\mathbf{D} = \left(n_1 v_1, n_2 v_2, n_3 v_3, n_2 v_3 + n_3 v_2, n_3 v_1 + n_1 v_3, n_1 v_2 + n_2 v_1 \right)^T, \quad (1.9)$$

where superscript T represents the transpose.

Because the trace of a moment tensor (which represents the isotropic component of moment tensor) from the CMT catalog is constrained to be zero in the routine inversion procedure, the moment tensor in the CMT catalog represents only the deviatoric part m_{ij}^* of the ‘full’ moment tensor m_{ij} such that:

$$m_{ij}^* = m_{ij} - \frac{1}{3} \delta_{ij} \text{Trace}(\mathbf{m}) = \left(c_{ijkl} - \frac{1}{3} \delta_{ij} \delta_{pq} c_{pqkl} \right) d_{kl}. \quad (1.10)$$

To invert for the anisotropic parameters only within the deviatoric subspace of moment tensor, the deviatoric elastic tensor:

$$b_{ijkl} = c_{ijkl} - \frac{1}{3} \delta_{ij} \delta_{pq} c_{pqkl} \quad (1.11)$$

is defined to explicitly impose the constraint that the isotropic component of moment tensor is zero.

I defined the Voigt equivalents of the 4-rank tensor \mathbf{b} and the deviatoric 3-by-3 moment tensor \mathbf{m}^* to be the 6-by-6 symmetric matrix \mathbf{B} and 6-by-1 column vector \mathbf{M}^* . The equation (1.8) for inverting source region anisotropic parameters using moment tensors becomes:

$$\mathbf{M}^* = \mathbf{B} \mathbf{D}, \quad (1.12)$$

where matrix \mathbf{B} has the following relationship with matrix \mathbf{C} :

$$B_{\alpha\beta} = C_{\alpha\beta} - \frac{1}{3} (\delta_{1\alpha} + \delta_{2\alpha} + \delta_{3\alpha}) (C_{1\beta} + C_{2\beta} + C_{3\beta}), \quad \alpha, \beta = 1, 2, \dots, 6 \quad (1.13)$$

1.2.4 Elastic tensor in a TTI medium

For a vertical transversely isotropic (VTI) medium, the five independent elastic constants in the c_{ijkl} (subscript 3 denotes the direction of symmetry axis) can be simplified in notation $C_{11}, C_{33}, C_{44}, C_{66}, C_{13}$. For example, c_{1122} becomes C_{12} and c_{1223} becomes C_{64} , etc. Thus equation (1.8) is equivalent to:

$$\begin{pmatrix} m_{11} \\ m_{22} \\ m_{33} \\ m_{23} \\ m_{13} \\ m_{12} \end{pmatrix} = \begin{pmatrix} C_{11} & C_{11} - 2C_{66} & C_{13} & 0 & 0 & 0 \\ C_{11} - 2C_{66} & C_{11} & C_{13} & 0 & 0 & 0 \\ C_{13} & C_{13} & C_{33} & 0 & 0 & 0 \\ 0 & 0 & 0 & C_{44} & 0 & 0 \\ 0 & 0 & 0 & 0 & C_{44} & 0 \\ 0 & 0 & 0 & 0 & 0 & C_{66} \end{pmatrix} \begin{pmatrix} d_{11} \\ d_{22} \\ d_{33} \\ 2d_{23} \\ 2d_{13} \\ 2d_{12} \end{pmatrix}. \quad (1.14)$$

The Thomsen parameters (Thomsen, 1986) are defined as:

$$\varepsilon = \frac{C_{11} - C_{33}}{2C_{33}}, \gamma = \frac{C_{66} - C_{44}}{2C_{44}}, \delta = \frac{(C_{13} + C_{44})^2 - (C_{33} - C_{44})^2}{2C_{33}(C_{33} - C_{44})}, \quad (1.15)$$

where ε represents P-wave anisotropy strength, γ represents SH-wave anisotropy strength and δ affects both P-wave and SV-wave anisotropy. The parameters ε and δ cannot be well-determined from the inversion. But their combination $\varepsilon - \delta$ can be reasonably estimated if ε is large and δ is negative (see section 1.6.2). We thus further calculated the parameter σ (Thomsen, 1986) which represents SV-wave anisotropy:

$$\sigma = \frac{C_{33}}{C_{44}}(\varepsilon - \delta) \quad (1.16)$$

The TTI medium has two more degrees of freedom (orientation) compared to the VTI medium. Its elastic tensor can be obtained by rotating the symmetry axis of VTI medium by

two angles: the dipping angle θ and the azimuth angle ϕ . Suppose the 3-by-3 rotation tensor is $r(\theta, \phi)$, the rotated 4-rank tensor for TTI medium is:

$$c_{i'j'k'l'}^{\text{TTI}} = r_{i'i} r_{j'j} r_{k'k} r_{l'l} c_{ijkl}^{\text{VTI}}, \quad i', j', k', l', i, j, k, l = 1, 2, 3. \quad (1.17)$$

Equivalently, the Bond transformation (Winterstein, 1990) converts the VTI medium to the TTI medium:

$$\mathbf{C}^{\text{TTI}} = \mathbf{N}^T \mathbf{C}^{\text{VTI}} \mathbf{N}, \quad (1.18)$$

where the Bond transformation matrix \mathbf{N} is defined as:

$$\mathbf{N} = \begin{pmatrix} r_{11}^2 & r_{12}^2 & r_{13}^2 & r_{12}r_{13} & r_{13}r_{11} & r_{11}r_{12} \\ r_{21}^2 & r_{22}^2 & r_{23}^2 & r_{22}r_{23} & r_{23}r_{21} & r_{21}r_{22} \\ r_{31}^2 & r_{32}^2 & r_{33}^2 & r_{32}r_{33} & r_{33}r_{31} & r_{31}r_{32} \\ 2r_{21}r_{31} & 2r_{22}r_{32} & 2r_{23}r_{33} & r_{22}r_{33} + r_{23}r_{32} & r_{21}r_{33} + r_{23}r_{31} & r_{22}r_{31} + r_{21}r_{32} \\ 2r_{31}r_{11} & 2r_{32}r_{12} & 2r_{33}r_{13} & r_{12}r_{33} + r_{13}r_{32} & r_{13}r_{31} + r_{11}r_{33} & r_{11}r_{32} + r_{12}r_{31} \\ 2r_{11}r_{21} & 2r_{12}r_{22} & 2r_{13}r_{23} & r_{12}r_{23} + r_{13}r_{22} & r_{13}r_{21} + r_{11}r_{23} & r_{11}r_{22} + r_{12}r_{21} \end{pmatrix}. \quad (1.19)$$

During the inversion, I fixed the P-wave and S-wave velocities along the TTI symmetry axis. Thus, there are 5 unknown anisotropic, including 3 Thomsen parameters, and 2 angle parameters for the TTI symmetry axis.

In practice, I put neighboring deep earthquakes that are close to each other (in space) into one inversion group and assumed they are in a common TTI anisotropic medium. If there are N earthquakes in a group, there are $5N$ constraints (5 independent components of the N deviatoric moment tensors) but $(5 + 3N)$ degrees of freedom since each shear fault plane has three degrees of freedom (strike, dip, rake). In principle, the elastic tensor can be determined

when $N \geq 3$. I will show that not all parameters can be equally resolved. In our inversion, the most robustly determined parameter is the *SH* anisotropy γ and (with less confidence) the *SV* anisotropy σ .

1.2.5 Two-step in situ anisotropy inversion using earthquake moment tensors

I applied a two-step inversion method for each earthquake group, in which I first determined the TTI symmetry axis and then inverted for the shear anisotropy parameters. To estimate the statistical errors in the inverted γ for each earthquake group, I used the bootstrap method (Efron and Tibshirani, 1994) where I generated 100 bootstrap samples by randomly sampling earthquakes (with replacement), and calculated the mean value and the standard error for the 100 inverted γ values. I also tested the two-step inversion method and verified its robustness.

In Step 1, I used moment tensors and an assumed set of anisotropic parameters to determine dyadic tensor \mathbf{d} . If the anisotropic parameter is close to the ‘correct’ one, the dyadic tensor \mathbf{d} should be close to $\mathbf{nv}+\mathbf{vn}$ and its determinant should be close to zero. For each earthquake group I found the optimized TTI symmetry axis that minimized the misfit function, which is the sum of absolute determinants of inverted fault geometry matrices (Vavrycuk, 2004)

$$\Delta_1 = \sum_j \left| \text{Det}(\mathbf{d}^{(j)}) \right| \quad (1.20)$$

for all moment tensors (indexed by j) within the earthquake group, where the fault geometry matrices $\mathbf{d}^{(j)}$ are inverted using equation (1.12).

During the inversion, C_{33} , C_{44} were density normalized and were fixed according to the averaged P and S wave velocities derived from the preliminary reference earth model (PREM) (Dziewonski and Anderson, 1981) based on the focal depths in the group with a 5% increase to

account for the high-velocity anomaly in the slab (Zhou, 1990; Zhao, 2004). I then grid-searched for the TTI symmetry axis and randomly searched for elastic constants within the range defined by the Thomsen parameters to minimize the misfit function Δ_1 .

In Step 2, I fixed the TTI symmetry axis obtained in the first step, and optimized the Thomsen parameters by randomly searching for elastic constants within the range defined by the three Thomsen parameters, and minimizing a new misfit between the eigenvectors and eigenvalues of observed and synthetic normalized moment tensors (square sum of all elements equals one). The new misfit function is defined as:

$$\Delta_2 = \chi_1 + \chi_2, \quad (1.21)$$

where

$$\chi_1 = \sum_j \frac{1}{3} \left[3 - \left| \mathbf{V}_1^{s(j)} - \mathbf{V}_1^{o(j)} \right| - \left| \mathbf{V}_2^{s(j)} - \mathbf{V}_2^{o(j)} \right| - \left| \mathbf{V}_3^{s(j)} - \mathbf{V}_3^{o(j)} \right| \right], \quad (1.22)$$

and

$$\chi_2 = \frac{1}{6} \sum_j \left[\left(\overline{\Lambda}_1^{s(j)} - \overline{\Lambda}_1^{o(j)} \right)^2 + \left(\overline{\Lambda}_2^{s(j)} - \overline{\Lambda}_2^{o(j)} \right)^2 + 100 \left(\overline{\Lambda}_3^{s(j)} - \overline{\Lambda}_3^{o(j)} \right)^2 \right]. \quad (1.23)$$

Here, the \mathbf{V} 's and $\overline{\Lambda}$'s represent the unit eigenvectors and the corresponding eigenvalues of the normalized moment tensor. These are indexed by subscript 1, 2, and 3 such that $|\overline{\Lambda}_1| \geq |\overline{\Lambda}_2| \geq |\overline{\Lambda}_3|$. The sums are over all earthquakes in a group. Superscripts "s(j)" and "o(j)" are for the j^{th} synthetic and observed moment tensor, respectively. The weighting factor 100 before eigenvalue $\overline{\Lambda}_3$ in χ_2 aims to bring the contribution of the eigenvalue with smallest absolute value to reach the same magnitude as $\overline{\Lambda}_1$ and $\overline{\Lambda}_2$. The eigenvectors and eigenvalues

are normalized, such that $|\mathbf{V1}|=|\mathbf{V2}|=|\mathbf{V3}|=1$, and $\bar{\Lambda}_1^2 + \bar{\Lambda}_2^2 + \bar{\Lambda}_3^2=1$ to make χ_1 and χ_2 have similar contribution to the misfit function. I also tried other relative weighting schemes and found that the results are essentially the same. This new misfit function Δ_2 is independent of the coordinate system and it describes the difference between our synthetic moment tensors and the observed ones. When the misfit function is minimized, the best-fit Thomsen parameters and shear dislocation faulting geometry are determined.

1.3 Synthetic tests of the inversion method

I used fault geometry from earthquakes in the intermediate depth deep earthquake group in Tonga from the CMT catalog and assumed a TTI anisotropy in the source region. The Thomsen parameters were set to be $\varepsilon = 35\%$, $\gamma = 40\%$, $\delta = -20\%$. C_{33} and C_{44} were density normalized and set to be $C_{33} = 100$, $C_{44} = 30 \text{ km}^2/\text{s}^2$ and the TTI symmetry axis was oriented at $\theta = 60^\circ$ and $\phi = 300^\circ$. 10% random Gaussian perturbation is added to C_{33} and C_{44} to represent velocity variations with depth of different events, while 0%, 10% and 20% Gaussian noise were added to synthetic moment tensors respectively to represent the error in the observed moment tensor. I used Gaussian noise because the Global CMT catalog assumes the error in inverted moment tensors to be Gaussian distribution (Dziewonski *et al.*, 1981). However, this assumption is not entirely valid. The discrepancy between the real Earth and the model, and deviation between point source model and a source distributed in time and space may lead to systematic errors.

I applied the two-step inversion method to the noise-contaminated moment tensors. In Step 1, our inverted optimized TTI symmetry axis coincided with the real TTI symmetry axis

for all three cases (Figure 1.2). In Step 2, I used the misfit Δ_2 and randomly searched for the optimized elastic constants within the range of Thomsen parameters at the TTI symmetry axis obtained in Step 1. I applied the bootstrap test with 100 bootstrap samples, and obtained $\varepsilon = 47 \pm 9\%$, $\gamma = 37 \pm 3\%$, $\delta = -15 \pm 8\%$, $\varepsilon - \delta = 61 \pm 8\%$ for noise-free case, $\varepsilon = 44 \pm 10\%$, $\gamma = 32 \pm 6\%$, $\delta = -13 \pm 8\%$, $\varepsilon - \delta = 58 \pm 8\%$ for the 10% noise case and $\varepsilon = 39 \pm 13\%$, $\gamma = 27 \pm 8\%$, $\delta = -9 \pm 11\%$, $\varepsilon - \delta = 48 \pm 7\%$ for the 20% noise case (Figure 1.3). Here the error is the standard deviation ($\pm 1\sigma$) obtained from the bootstrap. The percentage error represents one standard deviation. I noted that not all anisotropy parameters can be equally resolved (even in the isotropic medium, only the shear modulus plays a role in the moment tensor). In our case, the shear anisotropy, γ , is the best-resolved anisotropy parameter. The combination parameter $\varepsilon - \delta$ can also be reasonably estimated.

Note, in Figure 1.2 the local minimum in the northeast quadrant has a misfit about twice that of the global minimum in the southeast quadrant. If this local minimum had values of misfit more comparable to those of the global minimum, it would lead to ambiguity of orientation, as described in section 1.4.2.

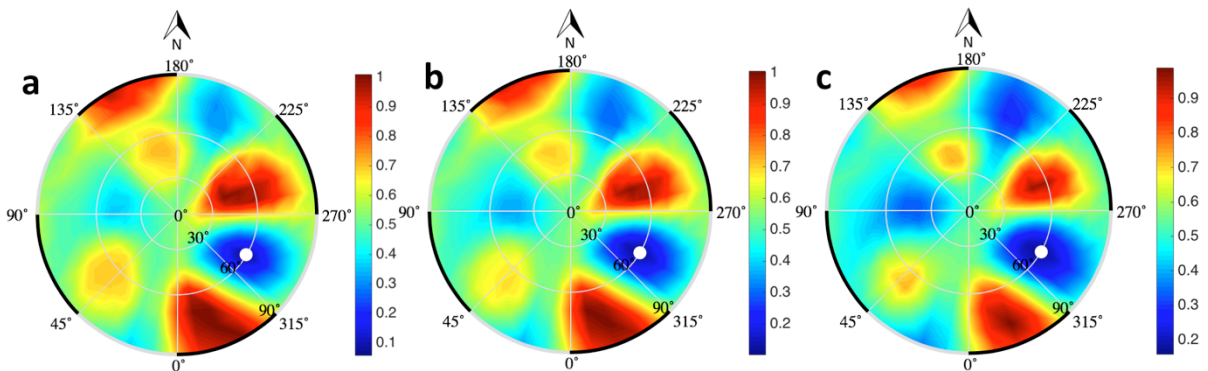


Figure 1.2 Lower hemispheric stereographic projection of the normalized misfit $\Delta_1(\theta, \phi)$ in Step 1 with different noise levels (a, b, c). Here ϕ is the azimuth of the anisotropy symmetry

axis and θ is 90° subtracting the plunge angle of the axis. These plots show the stereographic projection of misfit for different TTI symmetry axes (θ, ϕ) . The white dot represents the intersection between the true TTI symmetry axis in the model and the lower hemisphere. **(a)** Misfit Δ_1 using moment tensors with no noise. **(b)** Misfit Δ_1 using moment tensors with 10% Gaussian noise. **(c)** Misfit Δ_1 using moment tensors with 20% Gaussian noise.

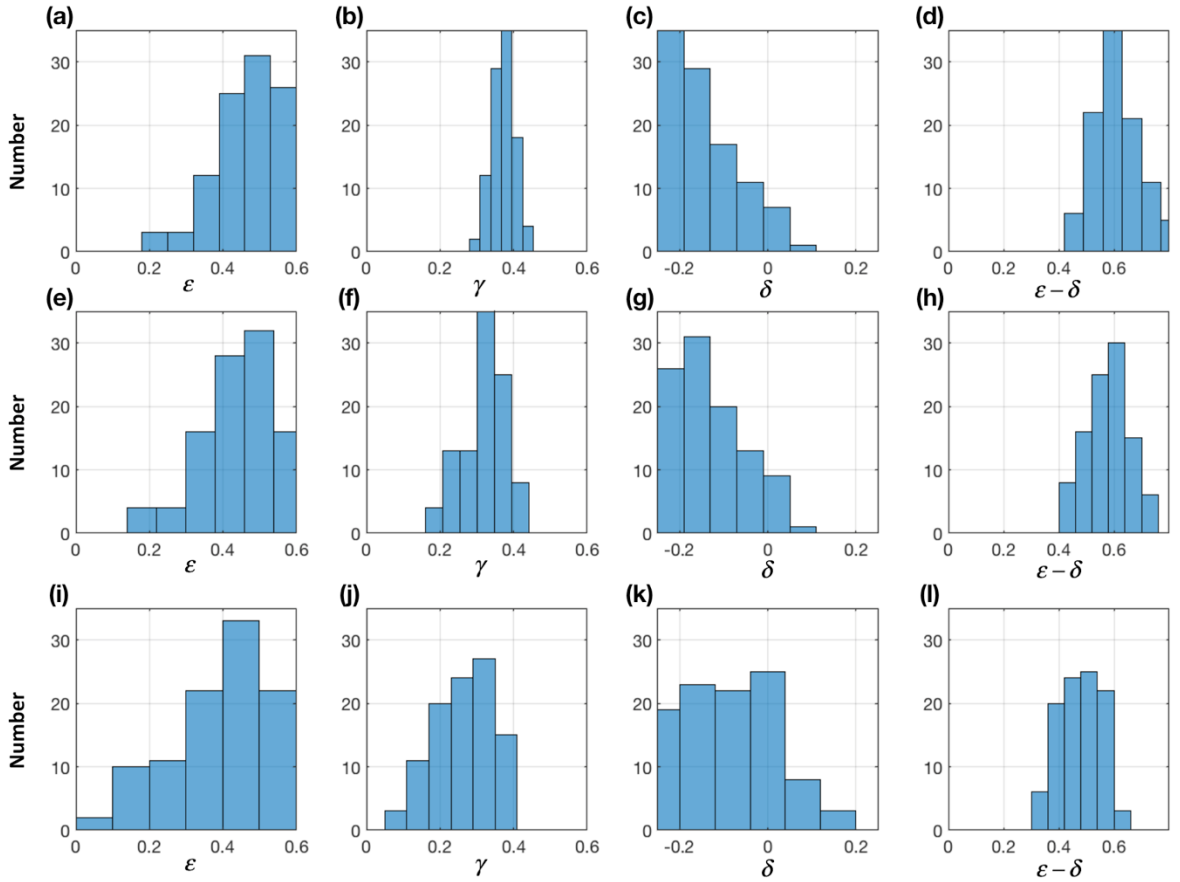


Figure 1.3 Histograms of inverted Thomsen parameters ϵ , γ , δ , and $\epsilon - \delta$ using the bootstrap samples in Step 2 of the synthetic test. I randomly searched for the optimized elastic constants within the searching range of Thomsen parameters and calculated the corresponding Thomsen parameters at the TTI symmetry axis inverted in Step 1. These plots show the histograms of ϵ ,

γ , δ , and $\varepsilon - \delta$ values for the bootstrap method with 100 bootstrap samples. **(a-d)** Histograms of ε , γ , δ , and $\varepsilon - \delta$ for moment tensors with no noise. **(e-h)** Histograms of ε , γ , δ , and $\varepsilon - \delta$ for moment tensors with 10% Gaussian noise. **(i-l)** Histograms of ε , γ , δ , and $\varepsilon - \delta$ for moment tensors with 20% Gaussian noise.

1.4 Strong in-situ anisotropy revealed by deep earthquake moment tensors in six global subduction zones

1.4.1 Data selection

I used the moment tensors from the CMT catalog from 1976 to 2013 for earthquakes of depths greater than 100 km and moment magnitude M_w between 5 and 6.6 (Vavrycuk, 2004) in 6 global subduction zones (Figure 1.4). The fault area of an M_w 6.6 earthquake is about 400 km² (Leonard, 2010). To select well-determined moment tensors, I followed the criteria by both Vavrycuk (2004) and Frohlich and Davis (1999) for ‘well-determined’ moment tensors: the relative error in the inverted moment tensor should not be larger than 15% and the relative CLVD strength should not be larger than 0.2 (theoretical maximum is 0.5). Deep earthquakes with very large CLVD ($|f_{CLVD}| > 0.2$) occurred mostly in two localized deep-focus regions (TG6 & 8) in Tonga subduction slab in our study. Further detailed study on events with very large f_{CLVD} should be done in the future. I further selected events associated with at least 15 recording seismic stations for well-determined moment tensors. I finally selected those earthquakes around the subducting slab interface (Gudmundsson and Sambridge, 1998) (distance less than 55km) to form earthquake groups by their spatial proximity in this study. This has resulted in 22 earthquake groups globally, each group having a similar spatial scale to

the regional study by Vavrycuk (2004). The selected earthquakes possess large non-double-couple (CLVD) components (Figure 1.1b).

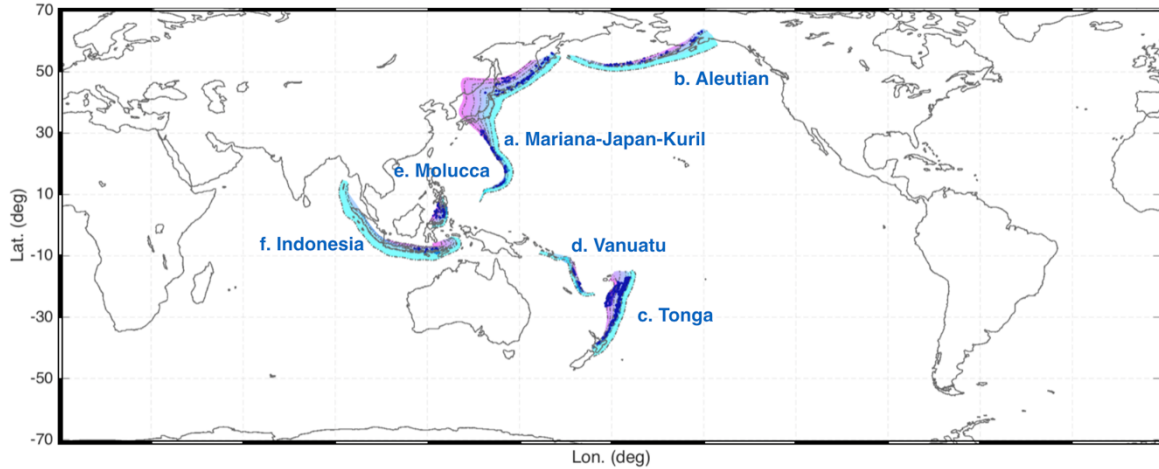


Figure 1.4 Global map view of all 6 subduction regions in this study. The colored patches here represent the subducting slab interfaces. The color changing from light green to pink represent depth from shallow to deep. Blue dots represent all 1,057 deep earthquakes used in this study.

1.4.2 Inverted anisotropy around deep earthquakes

I inverted for the TTI symmetry axis, the SH-wave anisotropy γ , and SV-anisotropy σ for 6 subduction zone systems: Tonga (TG), Vanuatu (VA), Molucca (MO), Indonesia (IND), Mariana-Japan-Kuriles (MJK), and Aleutians (AL) using selected moment tensors (Figure 1.4). For 18 out of the 22 studied earthquake groups (Figure 1.5; Figure 1.6), the symmetry axes are almost perpendicular to the slab interface (Figure 1.5; Figure 1.6; Figure 1.8a). However, there are three deep-focus regions, whose inverted symmetry axes are parallel to the slab interface (Figure 1.5; Figure 1.6; Figure 1.8a) and coincide with the maximum compression axes (the P axis, downdip) of the stress in the slab (Figure 1.9). These groups are MJK6 and MJK7 in Mariana-Japan-Kuriles and TG8 in Tonga (Figure 1.5; Figure 1.6). The anisotropy symmetry

axis for MJK4 is 45° from the normal to the slab interface (Figure 1.5; Figure 1.6; Figure 1.8a) but the corresponding γ and σ is weak. Overall, the TTI symmetry axis orientations of most subducted oceanic lithosphere indicate a dominant planar fabric orientated parallel to the slab interface.

The inverted *SH* anisotropy γ for the 22 earthquake groups is from 6% (MJK4; Marianas) to 46% (Figure 1.8b; Table 1.1). The mean and median values for this population are about 28%, which corresponds to a 25% difference between the *SH*-wave speeds along fastest and slowest direction. I also performed the inversion and obtained similar results (Figure 1.11) using a different moment tensor selection criterion where the relative error in the moment tensor defined by Vavrycuk (2004) is less than 10%.

The ε and δ are not well determined. However, the parameter σ approximately follows a normal distribution. The value of σ is from 31% to 84% with a typical mean value of 60% and an standard deviation of about 31% (Figure 1.8c, Table 1.1), which corresponds to a 15% difference between the *SV*-wave speeds along fastest and slowest direction.

There is no observable depth dependence to γ or TTI symmetry axis orientation (Figure 1.8a-b) nor relationship between anisotropy orientation and γ or σ (Figure 1.10a-b). There seems to be a weak trend that deeper earthquakes have larger values for σ (Figure 1.8c). For the relationship between γ and σ , there seems to be an negative correlation between these two *S*-wave anisotropy parameters, especially for TG groups (except for TG1) and MJK groups (except for MJK4) (Figure 1.8d). This interesting observation may be more study in the future.

To verify that the inverted TTI anisotropy can indeed cause the observed apparent non-DC radiation, I modeled the radiation pattern of each shear-dislocation earthquake using its

best-fit dislocation geometry embedded in the inverted TTI anisotropy. I found that the observed patterns could be well reproduced despite a variety of faulting geometries (Figure 1.7a). I also found that the apparent CLVD components of the modeled moment tensors are linearly correlated (the slope of the regression line is ~ 0.96) to those of the observed moment tensors (Figure 1.7b). Note that the TTI model *simultaneously* explained both large and small CLVD values, which suggests that the anisotropy around the deep earthquakes can be responsible for the non-DC radiation worldwide. Unlike the widely used source-side shear wave splitting technique which assumes that the S-wave motion in the source is linear polarization, which is true only for the double-couple point source in an isotropic medium (Vinnik and Kind, 1993; Lynner and Long, 2014; Nowacki *et al.*, 2015), the present method uses events with both DC mechanism and non-DC mechanism to directly evaluate the *in situ* anisotropy locally around the deep earthquakes, thus providing new information for understanding slab structure hosting deep earthquakes. Given the large estimated anisotropy values, the anisotropy region around the earthquakes is likely to be small in dimension (~ 10 - 20 km) to be consistent with a typical shear-wave splitting delay time measurement (~ 1 s) (Long, 2013) and other results from global studies (Yuan and Beghein, 2013; Chang *et al.*, 2015).

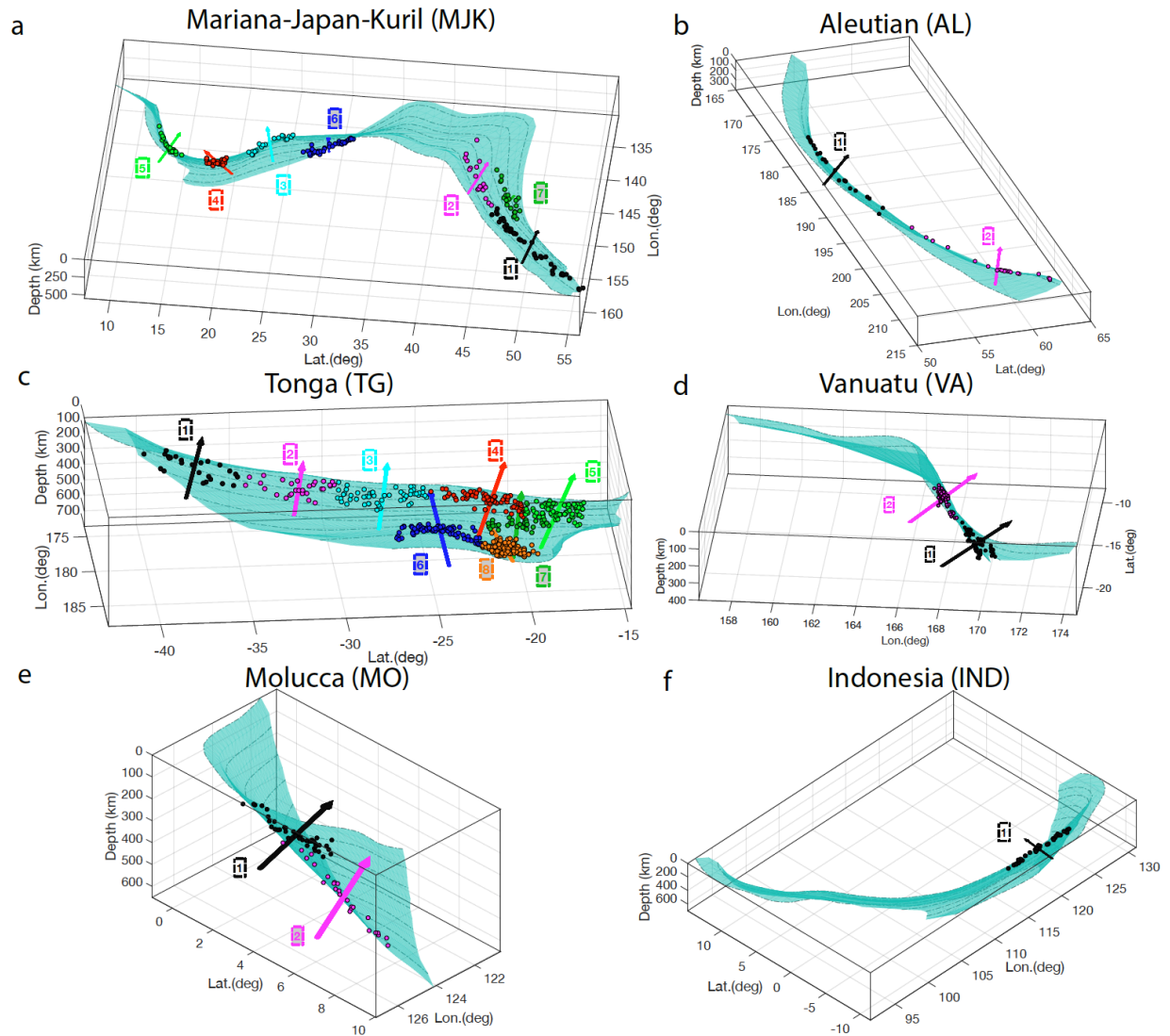


Figure 1.5 Inverted TTI anisotropy symmetry axes (colored arrowheads) with respect to slab geometry. (a), MJK earthquake groups 1–7. (b), AL groups 1 and 2. (c), TG groups 1–8. (d), VA groups 1 and 2. (e), MO groups 1 and 2. (f), IND group 1. Light green surfaces are the subducting slabs. Gray dashed lines are depth contour lines (every 100 km from the Earth's surface). Earthquakes (colored dots) are divided into different groups with different colors indexed by the corresponding group numbers shown in the open boxes (intermediate depth) as well as the shaded boxes (deep focus).

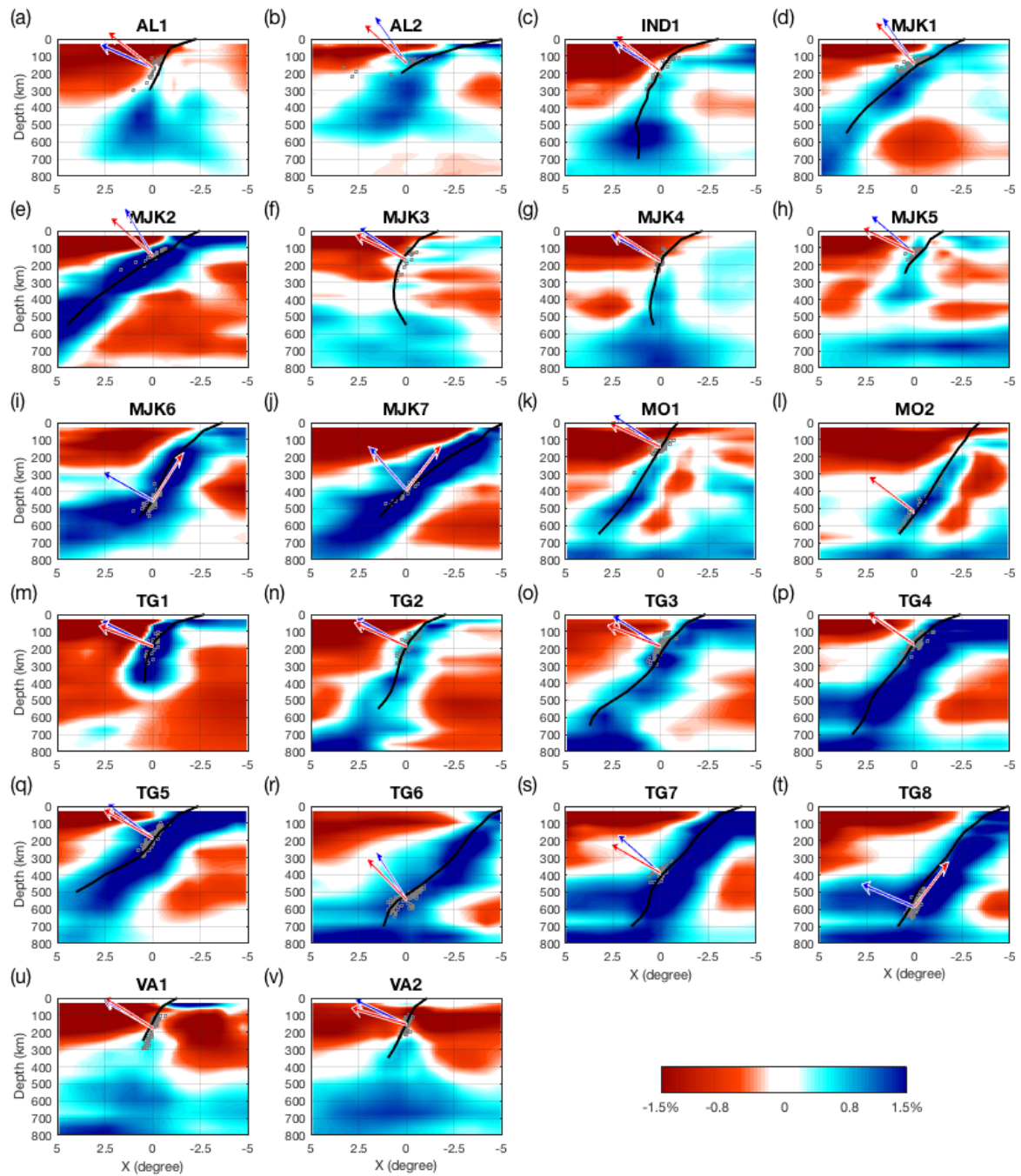


Figure 1.6 (a-v) 2-D vertical cross-sections of 22 regions in our study. Each cross-section contains the center and the slab normal for each deep earthquake group. The gray circles represent deep earthquakes projected on the cross-section plane. The bold black lines represent

the intersections of the slab interfaces by Gudmundsson and Sambridge (1998) and the cross-section planes. The red arrows represent the projection of inverted TTI anisotropy symmetry axes on the cross-section planes, and the blue arrows represent the normal of the slab interfaces in each region. The background P-wave tomographic model is created from the GAP_P4 Model by Fukao and Obayashi (2013). The color scale is $\pm 1.5\%$ in P-wave velocity perturbation where the red represents slower and blue represents faster regions.

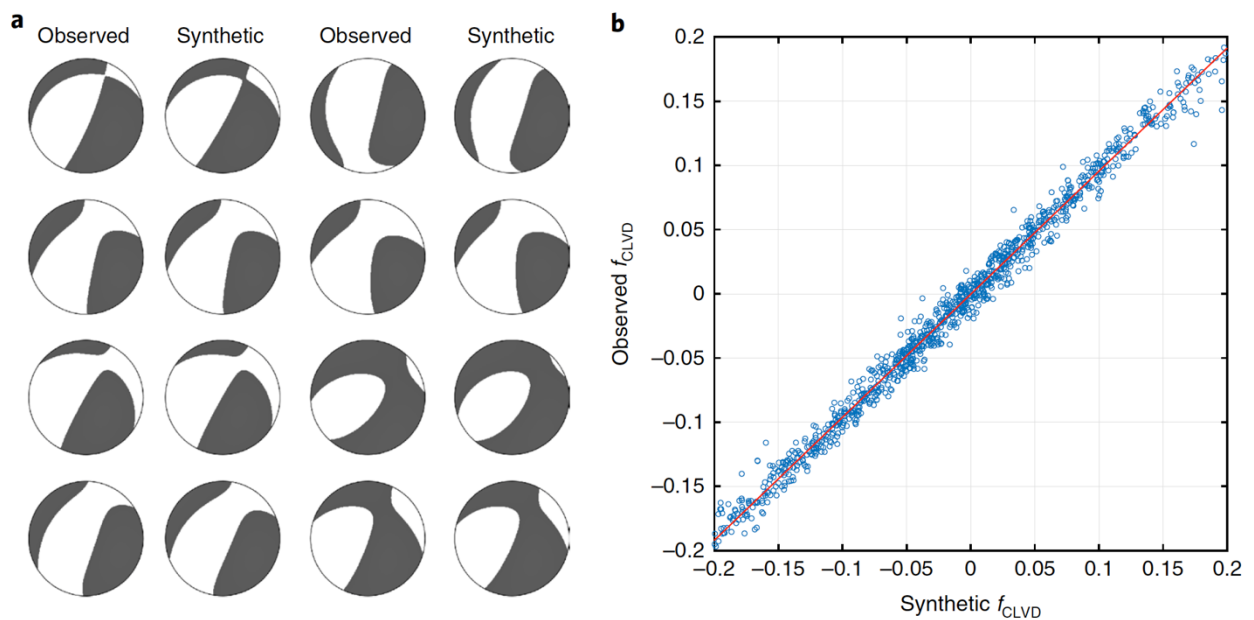


Figure 1.7 Apparent non-DC events caused by shear dislocations in anisotropic media. (a), Comparison between the observed and synthetic radiation patterns (‘beach ball’ representations of the lower hemispheric stereographic projection of the P-wave initial motion) for eight randomly selected earthquakes in the TG4 group. The grey regions represent outward motion and the white regions represent inward motion. The observed beach balls are from the CMT catalogue. The synthetic beach balls were modelled using the inverted anisotropy and best-fit shear dislocation faulting geometry for each event. The synthetic beach balls fit the observed ones well. (b) Cross-plot between the apparent CLVD components of observed moment tensors

and those of synthetic moment tensors for all the earthquakes in 22 earthquake groups. Each circle represents one earthquake. The red line is the orthogonal regression line for all 1,057 earthquakes in this study.

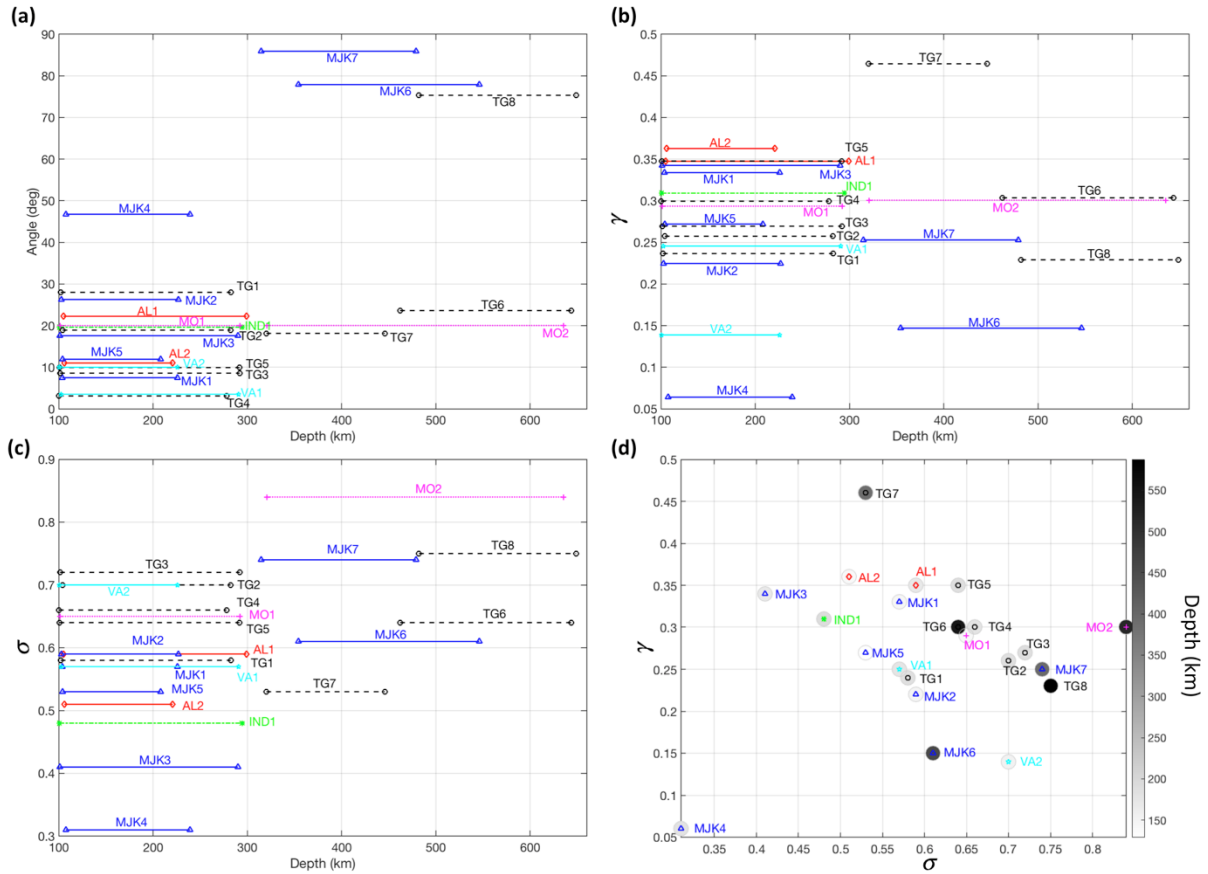


Figure 1.8 Summary of inverted anisotropy parameters. **(a)** The angles between TTI symmetry axes and the normal directions of the slab interfaces in all studied regions. See Figure 1.5 for groups' names. **(b)** The anisotropy strength γ in all studied regions. Horizontal lines represent depth ranges of different earthquake groups. **(c)** The anisotropy strength σ in all studied regions. Horizontal lines represent depth ranges of different earthquake groups. **(d)** Relationship between γ and σ . The background gray-colored circle represents the mean earthquake depth in the corresponding group.

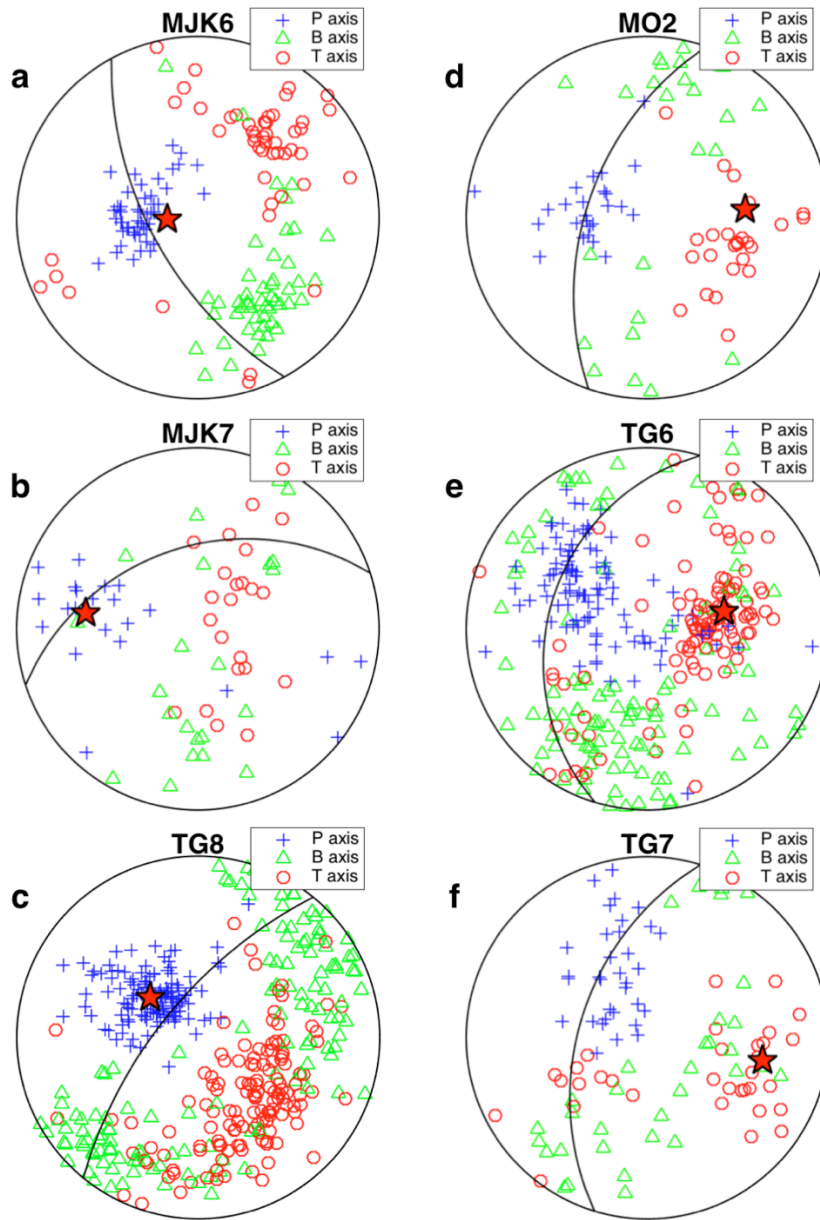


Figure 1.9 PBT axes (P: maximum compression axis, T: tension axis, B: perpendicular to P and T axes) and inverted anisotropy symmetry axes (red star) plotted on a stereographic projection of the lower hemisphere, for all six deep-focus earthquake groups including: (a) MJK6, (b) MJK7, (c) TG8, (d) MO2 (e) TG6 and (f) TG7. The black solid line represents the slab interface.

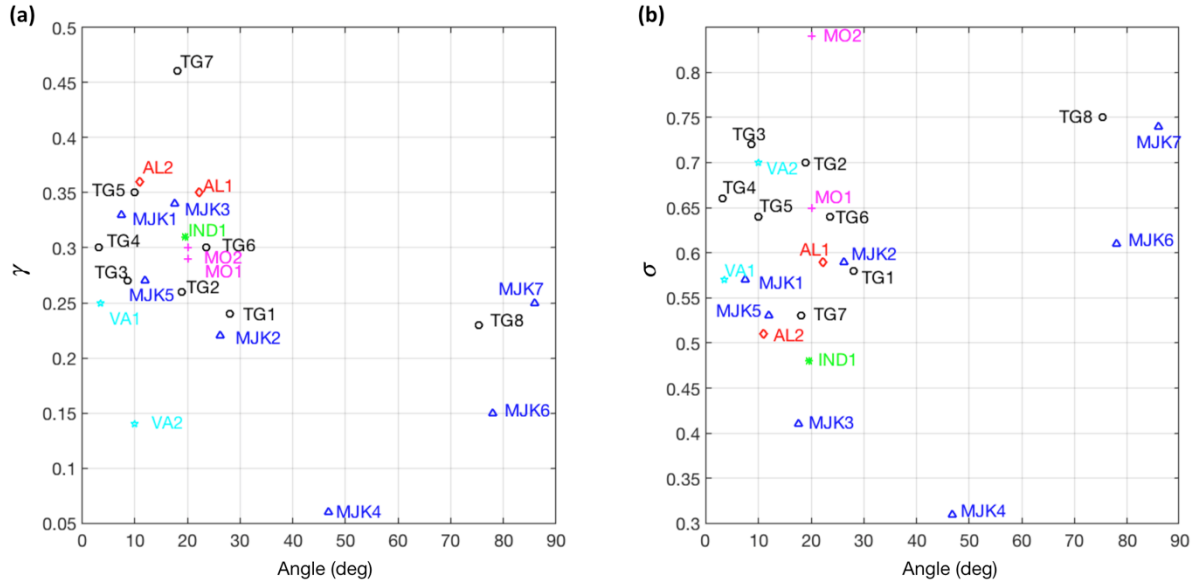


Figure 1.10 Cross plot between inverted (a) γ values and TTI symmetry axis angles and (b) σ values and TTI symmetry axis angles for all 22 groups (black circles) in this study. No clear trends between γ or σ values and angles are found.

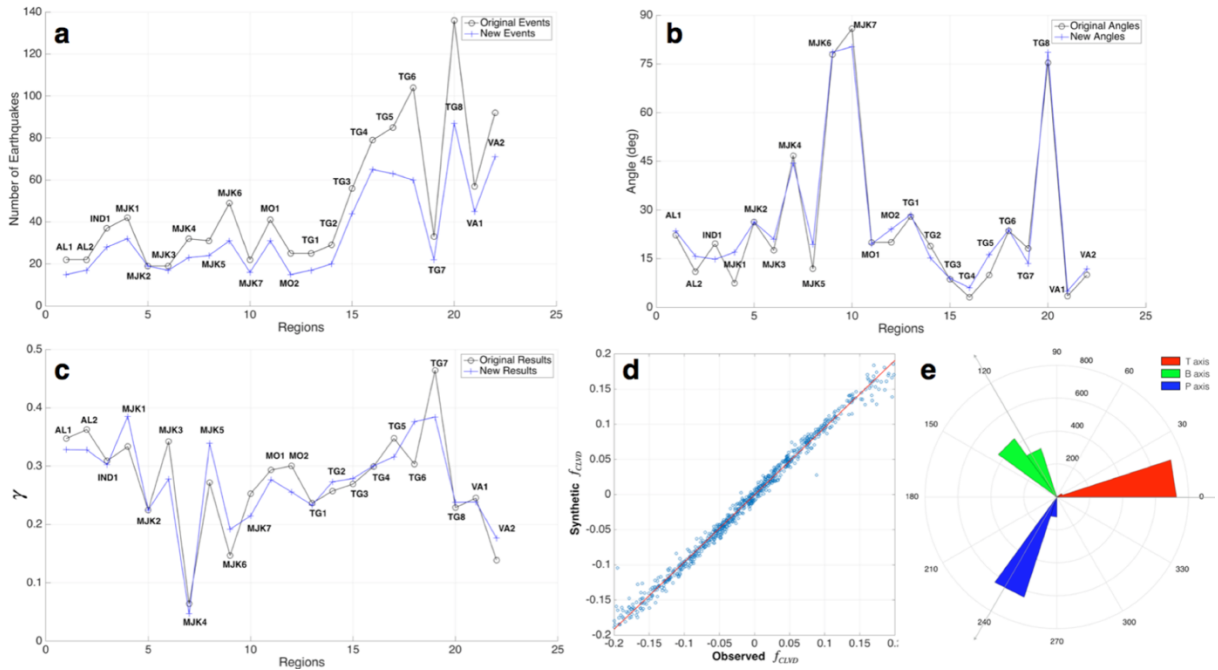


Figure 1.11 Inversion results of reselected earthquakes following the more strict criteria where the relative error in the moment tensors defined by Vavrycuk (2004) is less than 10%. **(a)** Comparison between number of reselected earthquakes (New Events) and earthquakes used in this study (Original Events) for all 22 groups. The number of all reselected earthquakes is 762. **(b)** Comparison of angles between inverted TTI symmetry axes and the corresponding slab normal for reselected earthquakes (New Angles) and earthquakes used in this study (Original Angles) for all 22 groups. **(c)** Comparison between inverted γ values from reselected earthquakes (New Results) and from earthquakes used in this study (Original Results) for all 22 groups. The mean and median values for new γ values are about 27.5%. **(d)** Cross plot between apparent CLVD components of observed MTs and those of synthetic MTs for all reselected earthquakes in 22 earthquake groups. The red line is the orthogonal regression line for all 762 reselected earthquakes with a slope of about 0.96. **(e)** Rose diagram to show angles between P, B, and T axes of the synthetic moment tensors and those of the observed moment tensors for all reselected earthquakes. Those three grey arrows represent the 0° angles between P, B, and T axes of the synthetic moment tensors and those of the observed moment tensors.

Earthquake Group	$\gamma \pm d\gamma$	$\sigma \pm d\sigma$	TTI Symmetry axes (θ, ϕ)	Number of earthquakes	Ambiguity in TTI symmetry axis?
MJK1	33±5%	57±32%	(44±5°, 301±4°)	42	No
MJK2	22±7%	59±34%	(48±5°, 314±6°)	19	Yes (89%) (60°, 170°)
MJK3	34±7%	41±31%	(56±3°, 256±7°)	19	No
MJK4	6±5%	31±35%	(67±3°, 209±3°)	32	No
MJK5	27±5%	53±32%	(58±4°, 312±8°)	31	No
MJK6	15±2%	61±28%	(24±5°, 93±6°)	49	No
MJK7	25±5%	74±31%	(64±4°, 96±2°)	22	No
AL1	35±6%	59±33%	(45±5°, 355±6°)	22	No
AL2	36±5%	51±28%	(41±5°, 295±6°)	22	No
TG1	24 ±5%	58±32%	(64±7°, 299±7°)	25	Yes (96%) (40°, 110°)
TG2	26±2%	70±33%	(75±11°, 283±6°)	29	No
TG3	27±3%	72±33%	(65±4°, 277±3°)	56	No
TG4	30±3%	66±31%	(58±3°, 302±4°)	79	No
TG5	35±4%	64±35%	(54±3°, 304±4°)	85	No
TG6	30±4%	64±35%	(43±5°, 261±3°)	104	No
TG7	46±4%	53±33%	(58±7°, 281±5°)	33	No
TG8	23±2%	75±28%	(37±3°, 130±4°)	136	No
VA1	25±5%	57±31%	(61±7°, 66±6°)	57	No
VA2	14±3%	70±25%	(56±7°, 77±6°)	92	No
MO1	29±4%	65±31%	(51±6°, 286±6°)	41	No
MO2	30±4%	84±29%	(56±4°, 270±5°)	25	No
IND1	31±5%	48±32%	(56±7°, 341±6°)	37	No

Table 1.1 Inverted γ, σ , TTI symmetry axes orientation, and number of earthquakes used in inversion for all 22 studied groups. The angles, θ and ϕ , include the mean value and standard error calculated from 50 bootstrap samples. The γ and σ show the mean values and standard errors $d\gamma$ and $d\sigma$ calculated from the results of 100 bootstrap samples. The last column shows whether there exists ambiguity in the orientation of TTI symmetry axes. None represents no ambiguity. The angles in the last column represent an alternative orientation of the TTI

symmetry axis. For MJK2, the local minimum/global minimum is about ~89%. For TG1, the local minimum/global minimum is about ~96%.

1.4.3 Anisotropy around intermediate-depth deep earthquakes

At depths less than 300km, the global consistency of the inverted anisotropy symmetry axes (Figure 1.8a; Figure 1.12) (perpendicular to the slab interface) and the associated large shear anisotropy, regardless of the subduction age, rate, and slab dip angles (Syracuse *et al.*, 2010), suggests common mechanisms to generate the inverted anisotropy. The commonly invoked mechanism for anisotropy in the mantle (preferred alignment of olivine and/or pyroxene orientation formed as a result of mantle flow or shearing (Karato *et al.*, 2008)) is far too weak to explain the observed values here (Jung *et al.*, 2009; Jung *et al.*, 2010).

The inverted anisotropy values for depths less than 300km are mostly consistent with aligned fluid or mineral inclusions (1.4.5) and hydrous minerals such as highly anisotropic sheet silicates (Mainprice and Ildefonse, 2009) and carbonate minerals (e.g. magnesite) (Yang *et al.*, 2014). All of these assemblages are expected to have large shear anisotropy values (Mainprice and Ildefonse, 2009; Brownlee *et al.*, 2013) and the expected overall slab-parallel foliation orientation is consistent with the inverted anisotropy symmetry axis and the large values of inverted anisotropy. The cause of the intermediate-depth earthquakes has long been speculated as being due to dehydration. The argument is mainly based on the experimentally observed dehydration embrittlement phenomenon (Raleigh and Paterson, 1965; Hacker *et al.*, 2003). This work provides new independent supporting evidence to corroborate the dehydration embrittlement as a viable mechanism for generating intermediate-depth earthquakes by showing the existence of such anisotropy structure around these earthquakes.

1.4.4 Anisotropy around deep-focus deep earthquakes

At depths greater than 300km, there are 6 groups of deep-focus earthquakes. Three of them, TG6, TG7, and MO2, have TTI symmetry axes perpendicular to the slab (Figure 1.8a; Figure 1.12b) and the other three, MJK6, MJK7, and TG8, have axes that are parallel to the slab, downdip (Figure 1.8a; Figure 1.12c). For the latter 3 groups, I emphasize that the inverted anisotropy symmetry axes are along the maximum compression axes (P axis) for the earthquakes (Figure 1.9a-c). The uniformity of the P axes indicates uniform downdip stress field. The overlapping regions between our studied regions (MJK6 and TG8) and those in Nowacki's study (Nowacki *et al.*, 2015) share similar anisotropy orientations.

For deep-focus earthquakes (depths > 300km), the polymorphic olivine-spinel phase change has been widely proposed to explain their mechanism (Green *et al.*, 2010). Under deviatoric stress, the microscopic spinel lenses (anticracks) display a strong tendency for their long axes to lie perpendicular to the *P* axis, which fits the latter 3 groups but not the first three. Given the seismic velocity difference between olivine and the spinel (~5%) (Bina and Wood, 1987), the expected anisotropy should be on the order of ~5%, not the ~25% mean S-wave anisotropy observed by us. Therefore, the anisotropy inferred by us cannot be produced by the metastable olivine phase change alone.

Magnesite, a major carbon host in subducted slab components under locally oxidized (oxygen fugacity > 2 log units above the iron - wüstite oxygen buffer; see ref. (Stagno *et al.*, 2011)) mantle conditions, has a mechanical strength orders of magnitude weaker than peridotite and has been suggested to cause deep-focus earthquakes via ductile-brittle instabilities (Holyoke *et al.*, 2014). In addition, the single-crystal magnesite S-wave anisotropy has been

measured to be around 40% (Yang *et al.*, 2014). Melting of subducted carbonate under these relatively oxidized slab conditions (Thomson *et al.*, 2016) could also generate strength instabilities that trigger deep-focus earthquakes. To explain the TTI symmetry axis orientations for the six deep-focus earthquake groups, it is possible that some of the laminated fabric structure formed at <300km depth can persist to the bottom of the mantle transition zone and form the observed anisotropy for the first 3 deep-focus groups (Figure 1.12b). But for the latter 3 groups, the coincidence among the anisotropy symmetry axes, the slab dip directions, and the uniformity of the maximum compression axes, suggests the anisotropy there may be strongly controlled by the stress in the subducting slab. Regions MJK6, MJK7, and TG8 have more concentrated dip-parallel principal compressive stress directions (σ_1), indicating strong and uniform differential stress field. Recent seismic tomographic results (Fukao and Obayashi, 2013) showed trapped or contorted slab geometries in the mantle transition zone in these three regions (Figure 1.6). However, all the earthquakes in these 3 regions are not in the flattened portions of the slab (Figure 1.6). Such a geometric contortion may 1) locally change the rock fabric orientation due to slab buckling, which cannot be resolved by the current tomographic resolution, or 2) indicate strong resistance to slab penetration into the lower mantle. In the following, I focus on the second possibility. This strong stress field could transpose magnesite-rich layers into flat inclusions through a pure to subsimple shear process, which at sufficient strain rates, can generate an overall TTI symmetry axis sub-parallel to the slab dip direction (Figure 1.12c). If the carbonate was melting, the uniform compressive stress (σ_1) field along the dip-parallel direction could possibly produce compaction-driven, oblate melt segregations perpendicular to σ_1 (Veveakis *et al.*, 2015; Weinberg *et al.*, 2015) at these high confining pressures within the slab. These slab perpendicular melt segregations could, in aggregate, result

in the observed slab parallel TTI symmetry axes and anisotropy. Magnesite and/or carbonate melt could both generate the required anisotropy and provide failure mechanisms for the occurrence of deep-focus earthquakes. Oblate solid aggregates or carbonatite melt phases around deep earthquakes in a subducted slab may be responsible for the observed anisotropy and apparent non-DC seismic radiation patterns of deep-focus earthquakes.

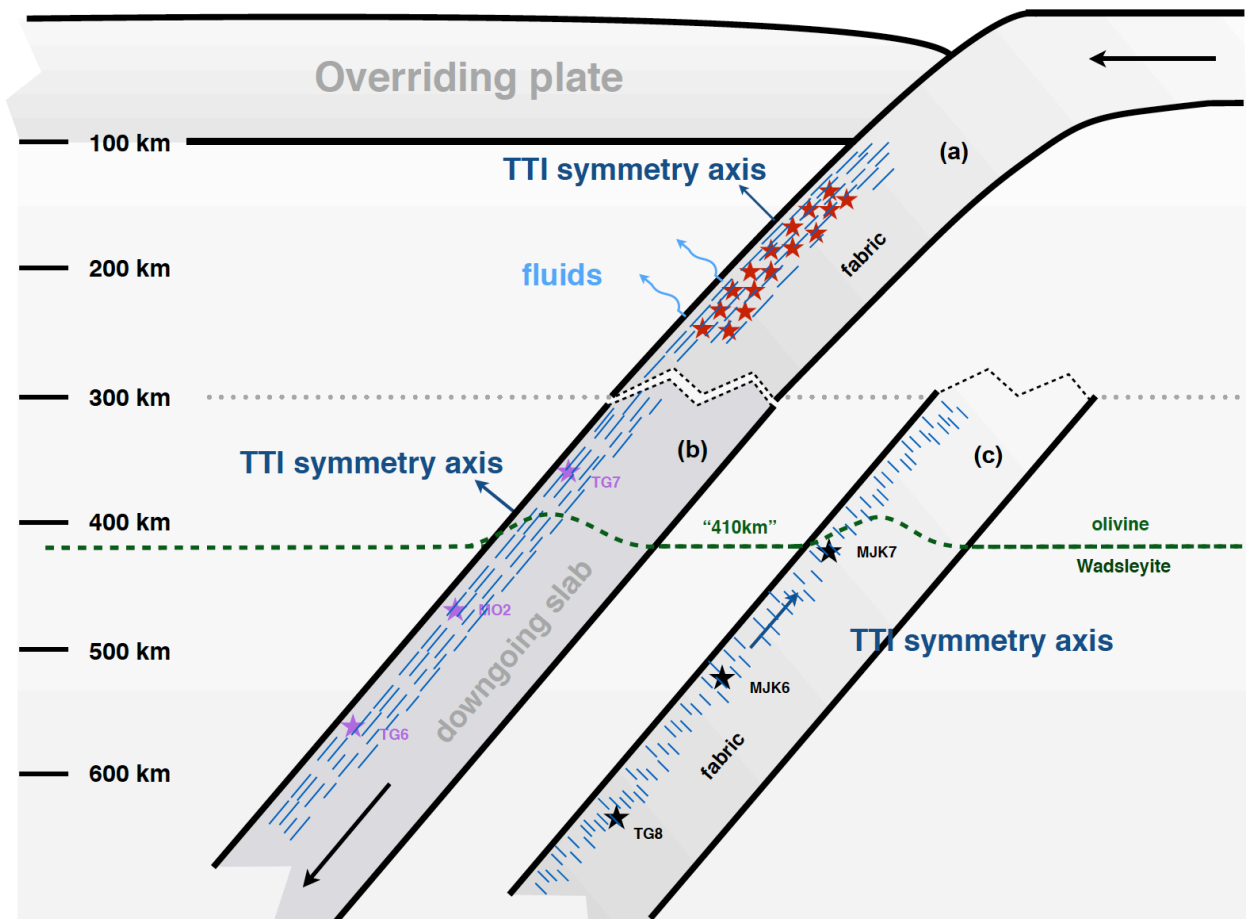


Figure 1.12 Schematic diagram of the origin of anisotropy. The gray dotted line represents our division between intermediate-depth and deep-focus earthquake events; the dark green dashed line represents the 410km phase change boundary. Short blue lines in the downgoing slab represent the inferred fabric in the slab. (a) The red stars represent intermediate-depth

earthquake groups with inverted TTI symmetry axes perpendicular to the slab interface. **(b)** The purple stars represent deep-focus earthquake groups with inverted TTI symmetry axes perpendicular to the slab interface. **(c)** And the black stars represent the deep-focus earthquake groups with TTI symmetry axes parallel to the slab interface.

1.4.5 Rock physics model for large shear anisotropy

Aligned inclusions (solid or liquid) can cause effective seismic anisotropy. I assumed perfectly aligned penny-shape inclusions in our discussion, which was also commonly done in previous studies. If the inclusions are weak in mechanical strength such as for the fluid/melt inclusions, the effective anisotropy strength depends on both the volume fraction ϕ of the inclusions and the aspect ratio e (thickness/diameter) of the inclusion geometry. Based on Eshelby-Cheng's model (Cheng, 1993; Thomsen, 1995), for a medium with Poisson's ratio equals 0.25, the shear anisotropy Thomsen parameter is $\gamma \sim \frac{8}{7} \eta_c$ where η_c is called the 'crack density' and is defined as $\eta_c = \frac{3}{4\pi} \frac{\phi}{e}$. If ϕ is 2% and the aspect ratio e is 0.01, γ is about 0.5. It is possible that inside the Earth e may be smaller, so we need even less inclusion volume to have a large anisotropy. Our above calculation is also valid for magnesite solid inclusions, as the magnesite strength is orders of magnitude smaller than the hosting rock. Imperfect alignment of the orientation of inclusions may also decrease the γ to our observed values.

1.4.6 Relationship between moment magnitude and f_{CLVD} values

From the selected deep earthquakes, it appears that deep earthquake events with larger moment magnitude (M_W from 6.2 to 6.6) tend to have smaller magnitude of f_{CLVD} compared with those with smaller moment magnitudes (M_W from 5 to 5.4) (Figure 1.13). What causes this

phenomenon? One possible explanation may be that the in-situ anisotropy is a localized small-scale feature. Using an empirical relationship (Leonard, 2010) between the length L and width W of a rectangular fault and its seismic moment:

$$\begin{aligned}
 A &= \left(\frac{M_0}{C_2 \mu} \right)^{\frac{2}{3}} \\
 L &= \left(\frac{A}{C_1} \right)^{\frac{3}{5}}, \\
 W &= C_1 \times (L)^{\frac{2}{3}}
 \end{aligned} \tag{1.24}$$

where M_0 is the seismic moment, and A is the fault area; $C_1 = 17.5 m^{\frac{1}{3}}$ and $C_2 = 3.8 \times 10^{-5}$ are the constants used in scaling relations; $\mu = 3.3 \times 10^{10} N/m^2$ is the shear modulus; together with the relationship between the seismic moment and the moment magnitude (Leonard, 2010):

$$M_0 = 10^{\left[\frac{3}{2}(M_w + 6.07) \right]}, \tag{1.25}$$

the fault dimension for deep earthquakes with different moment magnitudes can be estimated (Figure 1.14).

The dimension for an earthquake with moment magnitude 6.2 is estimated to be $15 km \times 10 km$. The dimension of the intra-slab anisotropic structure may also be of a similar scale.

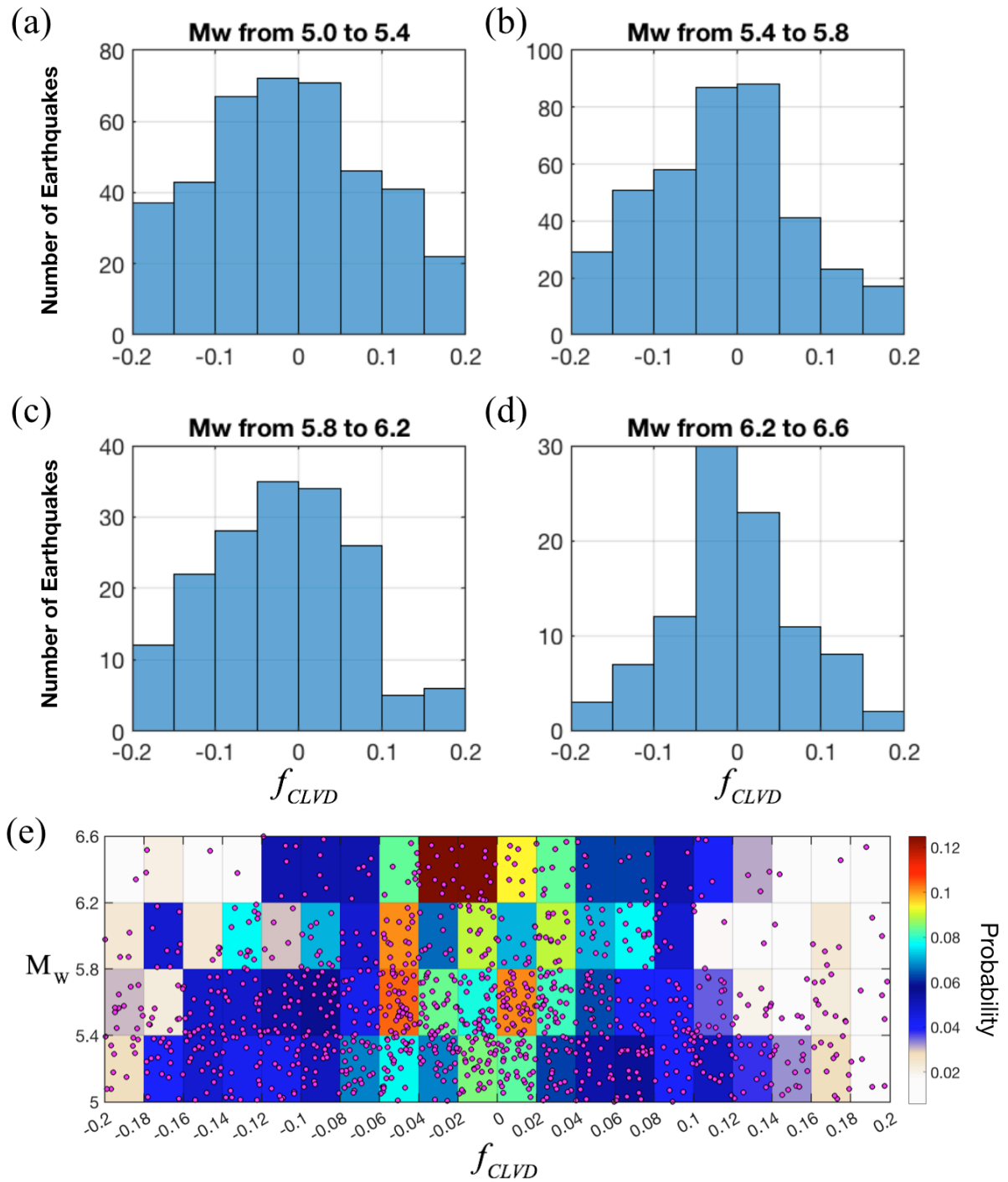


Figure 1.13 Relationship between the moment magnitude and f_{CLVD} value for the selected 1057 deep earthquakes. (a-d) f_{CLVD} histogram of deep earthquakes within different moment magnitude ranges (a) M_w between 5.0 and 5.4. (b) M_w between 5.4 and 5.8. (c) M_w between

5.8 and 6.2. (d) M_W between 6.2 and 6.6. (e) Probability distribution within different f_{CLVD} - M_W bins. The bin interval for M_W is 0.4 and bin interval for f_{CLVD} is 0.02. Each magenta scatter represents one selected deep earthquake.

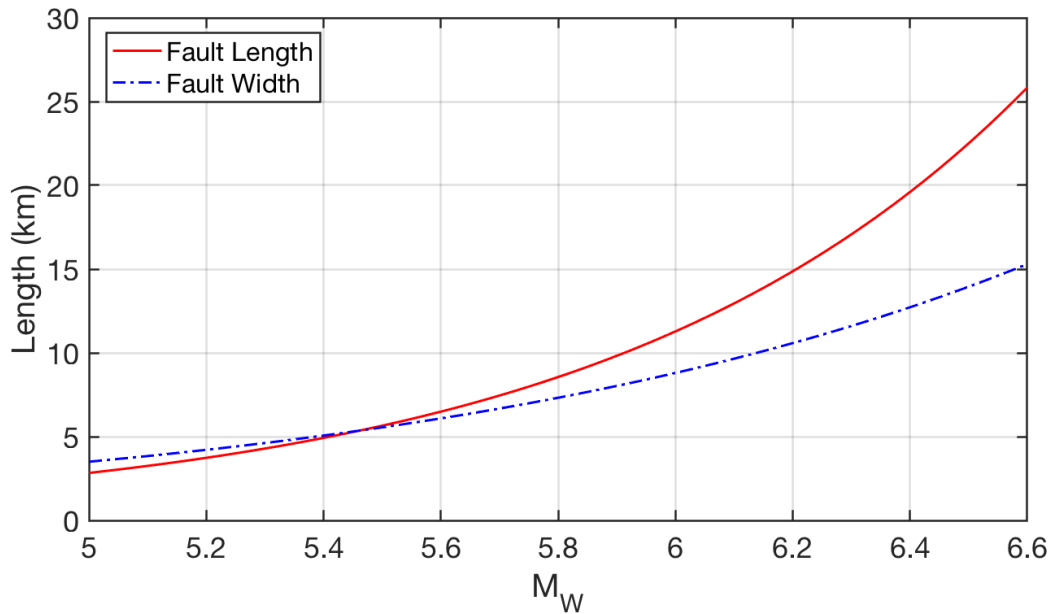


Figure 1.14 Rectangular fault dimension for different moment magnitude. The red solid line represents the length of the fault. The blue dashed line represents the width of the fault.

1.5 A regional study using F-net moment tensors

In this section, I applied the method to invert for in-situ anisotropy (intra-slab anisotropy) in subducting slab using the F-net moment tensor dataset (Kubo *et al.*, 2002). I selected earthquake events with magnitudes between 3 and 6.6 near the subducting slab interface (Gudmundsson and Sambridge, 1998) in Japan with latitude between 30°N to 46°N, longitude between 137°E to 148°E, and depth between 60 km and 200 km, from 1998-01-01 to 2017-12-31. The selected

earthquake events also meet two other criteria: (i) the CLVD (compensated linear vector dipole) is between -0.2 and 0.2 (maximum range from -0.5 to 0.5) and (ii) the variance reduction which represents the quality of the inverted moment is greater or equal than 75% (Kubo *et al.*, 2002). Higher variance reduction represents higher quality. This selection procedure resulted in 1034 selected earthquake events. I applied the K-means (Lloyd, 1982) unsupervised cluster algorithm to automatically cluster the earthquake events by their spatial distribution and obtained 25 groups (Figure 1.15; Figure 1.16).

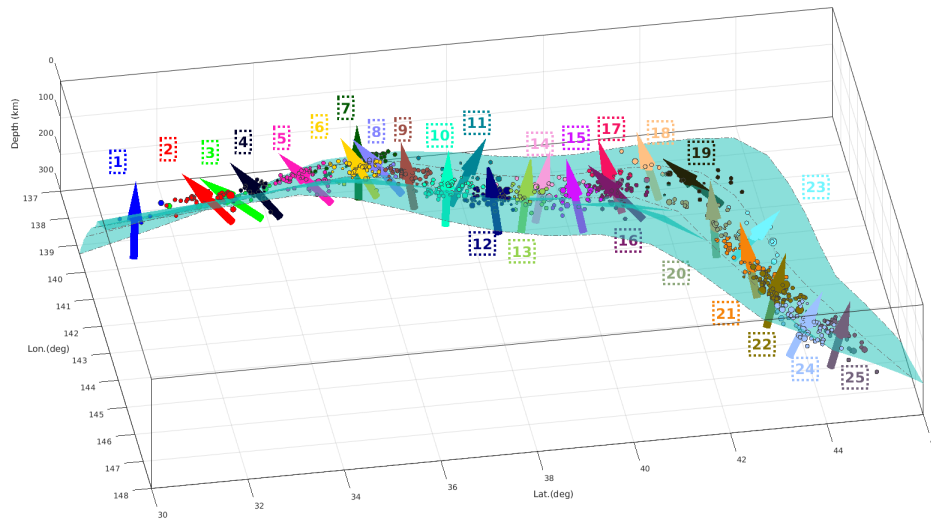


Figure 1.15 Intra-slab anisotropy inverted using earthquake moment tensors from the F-net. Earthquakes (colored dots) are clustered into different groups with different colors indexed by the corresponding group numbers shown in the open boxes. Colored arrowheads represent inverted TTI anisotropy symmetry axes. Light green surfaces are the subducting slabs. Gray dashed lines are depth contour lines (every 100km from the Earth's surface).

I then applied the inversion method to those 25 groups to obtain both TTI symmetry axes orientation (headed arrows in Figure 1.15. and magenta arrows in Figure 1.16) and the shear wave anisotropy strength γ (Figure 1.17b). The TTI symmetry axes are mostly either normal to

the slab interface or 45° with respect to the slab normal (Figure 1.17a). The SH-wave anisotropy strength γ ranges from 4% to 39%, and mean and median values are both around 21% (Figure 1.17b) which represents the SH wave propagating perpendicular to the TTI symmetry axis is 19% faster than the SH wave propagating parallel to the TTI symmetry axis. The SV-wave anisotropy strength ranges from 41% to 81%, and mean and median values are both around 59%, which represents the SV wave is about 15% faster along the fastest than the slowest direction. I did not observe any dependence of TTI symmetry axis orientation or γ on the depth of earthquakes (Figure 1.17). I show the inverted TTI symmetry axes, means and standard errors γ of and σ from bootstrap results (Efron and Tibshirani, 1994) in Table 1.2.

There exists ambiguity in many of the orientation of TTI symmetry axes (Table 1.2), meaning that an alternative TTI symmetry axis also fits the observed moment tensors. This ambiguity may be caused by many reasons. One possibility is that our assumption about anisotropy may not be valid. If the source region is orthorhombic, there will exist three local minimums corresponding to the three symmetry axes. However, I found that if the inverted anisotropy is strong and the number of earthquakes used in the inversion is large, the ambiguity reduces. For the groups with no ambiguity in TTI symmetry axis orientation (group 10, 12, 13, 14, 17, 18, 20, 22), most of them are nearly perpendicular to the slab interface (except group 18). This problem needs to be addressed in the future research.

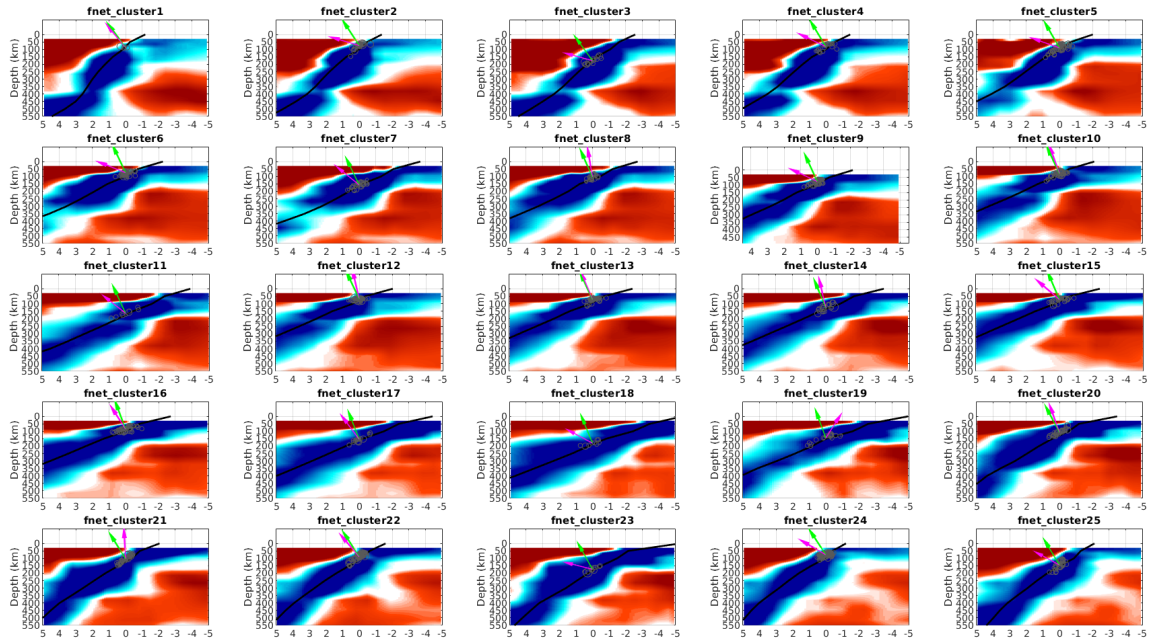


Figure 1.16 2-D vertical cross-sections of 25 groups in our preliminary study. Each cross-section contains the center and the slab normal for each deep earthquake group. The gray circles represent deep earthquakes projected on the cross-section plane. The bold black lines represent the intersections of the slab interfaces (Gudmundsson and Sambridge, 1998) and the vertical cross-section planes. The magenta arrows represent the projection of inverted TTI anisotropy symmetry axes on the cross-section planes, and the green arrows represent the normal of the slab interfaces in each region. The background P-wave tomographic model is created from the GAP_P4 Model by (Fukao and Obayashi, 2013). The color scale is $\pm 1.5\%$ in P-wave velocity perturbation where the red represents slower and blue represents faster regions.

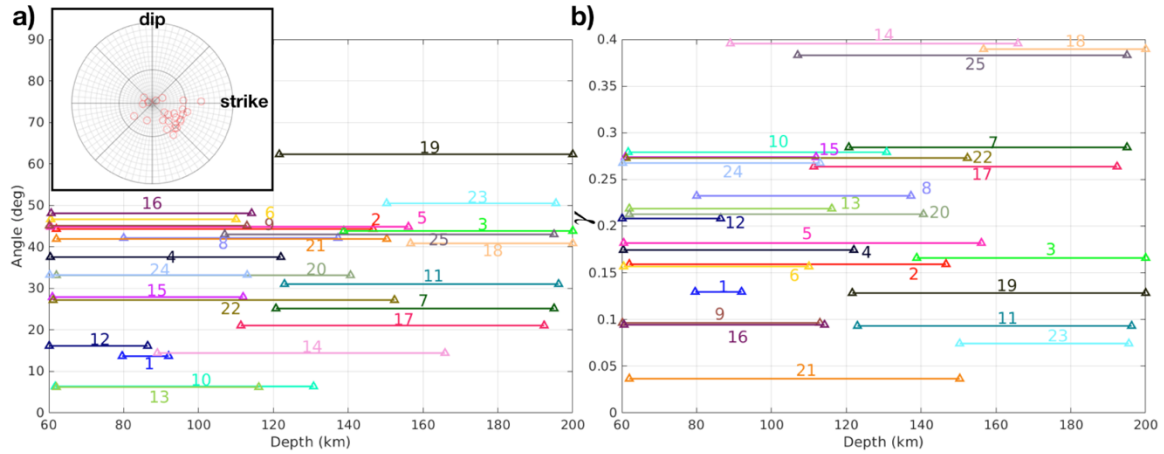


Figure 1.17 The angles between TTI symmetry axes and the normal direction of slab interfaces in all 25 groups. The plot inside the black box shows the upper hemisphere stereographic projection of TTI symmetry axes (red circles). The center of the plot represents slab normal. Right direction represents the strike of the slab. Upper direction represents the up dipping of the slab. **b)** The anisotropy strength γ in all 25 groups. Horizontal lines represent depth ranges of different earthquake groups.

Earthquake Group	$\gamma \pm d\gamma$	$\sigma \pm d\sigma$	TTI Symmetry axes (θ, φ)	Number of earthquakes	Ambiguity in TTI axis orientation?
Cluster 1	14±5%	57±31%	(41°, 282°)	5	Yes
Cluster 2	13±6%	63±31%	(74°, 237°)	36	Yes
Cluster 3	16±6%	63±33%	(75°, 224°)	17	Yes
Cluster 4	18±7%	46±29%	(65°, 234°)	26	Yes
Cluster 5	18±4%	53±31%	(71°, 234°)	60	Yes
Cluster 6	16±2%	71±30%	(69°, 250°)	123	Yes
Cluster 7	25±7%	63±31%	(51°, 278°)	33	Yes
Cluster 8	25±6%	52±29%	(41°, 203°)	30	Yes
Cluster 9	16±7%	41±35%	(66°, 269°)	62	Yes
Cluster 10	25 ±5%	70±29%	(20°, 287°)	55	No
Cluster 11	8±4%	70±34%	(53°, 315°)	10	Yes
Cluster 12	21±2%	76±25%	(17°, 250°)	66	No
Cluster 13	25±6%	65±29%	(24°, 298°)	83	No
Cluster 14	34±2%	60±30%	(17°, 320°)	22	No
Cluster 15	30±4%	57±33%	(50°, 263°)	39	Yes
Cluster 16	13±7%	56±32%	(54°, 218°)	46	Yes
Cluster 17	26±3%	57±33%	(39°, 250°)	17	No
Cluster 18	38±8%	56±32%	(62°, 261°)	9	No
Cluster 19	9±4%	58±31%	(51°, 200°)	19	Yes
Cluster 20	23±5%	68±28%	(37°, 272°)	36	No
Cluster 21	6±5%	57±30%	(32°, 255°)	46	Yes
Cluster 22	27±3%	81±25%	(46°, 300°)	77	No
Cluster 23	8±2%	57±31%	(76°, 318°)	11	Yes
Cluster 24	28±5%	55±29%	(61°, 309°)	72	Yes
Cluster 25	28±5%	53±30%	(64°, 296°)	34	Yes

Table 1.2 Inverted γ , σ , TTI symmetry axes orientation, and the number of earthquakes used in inversion for all 25 studied groups. The γ and σ show the mean values and standard errors $d\gamma$ and $d\sigma$ calculated from the results of 100 bootstrap samples. The last column shows whether there exists ambiguity in the orientation of TTI symmetry axes.

1.6 Full moment tensor in a transversely isotropic medium

Since the percentages of isotropic, CLVD, and DC component of a moment tensor are simple combinations of eigenvalues of the moment tensor (1.3) (1.4), ISO, CLVD, and DC are independent of the coordinate system. Without loss of generality, for an arbitrary shear fault in a determined TTI medium, we could calculate all possible values of ISO, CLVD, and DC by rotating to the corresponding VTI medium and changing the orientation of the shear fault by two angles (dip angle and rake angle). The eigenvalues of the moment tensor do not change with the strike angle of the shear fault because of the symmetry around vertical axis for the VTI medium.

1.6.1 Relationship between ISO and CLVD

Suppose initially a horizontal shear fault with slip along the east direction in an East (1)-North (2)-Up (3) (ENU) coordinate system. The slip normal vector is:

$$\begin{aligned} \mathbf{n} &= (0, 0, 1) \\ \mathbf{v} &= (1, 0, 0) \end{aligned} \quad (1.26)$$

The fault geometry is defined by the tensor \mathbf{d} (1.7) and:

$$\mathbf{d} = \begin{pmatrix} 0 & 0 & 0.5 \\ 0 & 0 & 0 \\ 0.5 & 0 & 0 \end{pmatrix} \quad (1.27)$$

In order to obtain an shear fault that can produce arbitrary ISO and CLVD values in a VTI medium, I first right-hand rotated the fault plane along the 3-axis by angle θ (changing the rake

of the fault) and then right-hand rotated the fault plane along the 1-axis by angle ϕ (changing the dipping angle of the fault). The rotated fault geometry tensor is:

$$\mathbf{d}^{\text{rot}} = \mathbf{r}_1 \mathbf{r}_3 \mathbf{d} \mathbf{r}_3^T \mathbf{r}_1^T = \frac{1}{2} \begin{pmatrix} 0 & -\cos(\theta)\sin(\phi) & \cos(\theta)\cos(\phi) \\ -\cos(\theta)\sin(\phi) & -\sin(2\theta)\sin(\phi) & \sin(\theta)\cos(2\phi) \\ \cos(\theta)\cos(\phi) & \sin(\theta)\cos(2\phi) & \sin(\theta)\sin(2\phi) \end{pmatrix}, \quad (1.28)$$

where \mathbf{r}_1 and \mathbf{r}_3 the right-hand rotation tensors along the East (1) and Up (3) direction.

According to equation (1.6), the moment tensor with fault geometry \mathbf{d}^{rot} in a VTI medium defined by equation (1.14) is:

$$\mathbf{m} = \frac{1}{2} \begin{pmatrix} (C_{13} - C_{11} + 2C_{66})\sin(\theta)\sin(2\phi) & -2C_{66}\cos(\theta)\sin(\phi) & 2C_{44}\cos(\theta)\cos(\phi) \\ -2C_{66}\cos(\theta)\sin(\phi) & (C_{13} - C_{11})\sin(\theta)\sin(2\phi) & 2C_{44}\sin(\theta)\cos(2\phi) \\ 2C_{44}\cos(\theta)\cos(\phi) & 2C_{44}\sin(\theta)\cos(2\phi) & (C_{33} - C_{13})\sin(\theta)\sin(2\phi) \end{pmatrix} \quad (1.29)$$

As an example, suppose C_{33} and C_{44} are density normalized to $100 \text{ km}^2/\text{s}^2$ and $30 \text{ km}^2/\text{s}^2$, and the Thomsen parameters are: $\varepsilon = 0.05$, $\gamma = 0.25$, $\delta = -0.05$ ($\sigma = 0.3$). Then the ISO and CLVD varies with respect to two angles θ and ϕ as in (Figure 1.18).

The trace of the moment tensor \mathbf{m} is:

$$\text{Trace}(\mathbf{m}) = \frac{1}{2} [C_{33} + C_{13} - 2(C_{11} - C_{66})] \sin(\theta) \sin(2\phi). \quad (1.30)$$

When $\theta = 0^\circ$ or $\phi = 0^\circ, 90^\circ$ or $C_{33} + C_{13} - 2(C_{11} - C_{66}) = 0$, the trace of the moment tensor is zero, which implies that:

- (i) A strike slip fault in a VTI medium always produces zero ISO.

- (ii) A shear slip on a vertical or horizontal fault plane in a VTI medium always produces zero ISO.
- (iii) If the elastic parameters satisfy $C_{33} + C_{13} - 2(C_{11} - C_{66}) = 0$, an arbitrary fault in this VTI medium will always produce zero ISO (In the isotropic special case, this condition is always satisfied). Unlike the first two cases which only involves the orientation relationship between the shear fault and the VTI medium, equation $C_{33} + C_{13} - 2(C_{11} - C_{66}) = 0$ is a property of the VTI medium only. Let us further examine the CLVD value under the condition that the ISO is zero.

Case 1: $\theta = 0^\circ$:

$$\mathbf{m} = \begin{pmatrix} 0 & -C_{66} \sin(\phi) & C_{44} \cos(\phi) \\ -C_{66} \sin(\phi) & 0 & 0 \\ C_{44} \cos(\phi) & 0 & 0 \end{pmatrix} \quad (1.31)$$

\mathbf{m} 's eigenvalues are:

$$\{0, \pm \sqrt{C_{44}^2 \cos^2(\phi) + C_{66}^2 \sin^2(\phi)}\} \quad (1.32)$$

Thus, the CLVD component is zero. The moment tensor is a pure double-couple.

Case 2: $\phi = 0^\circ, 90^\circ$

$$\mathbf{m} = \begin{pmatrix} 0 & 0 & C_{44} \cos(\theta) \\ 0 & 0 & C_{44} \cos(\theta) \\ C_{44} \cos(\theta) & C_{44} \cos(\theta) & 0 \end{pmatrix} \quad (1.33)$$

\mathbf{m} 's eigenvalues are:

$$\{0, \pm C_{44}\} \quad (1.34)$$

Thus, the CLVD component is also zero. The moment tensor is a pure double-couple.

Case 3: $C_{33} + C_{13} - 2(C_{11} - C_{66}) = 0$

Although its eigenvalues are not straightforward to solve, its determinant is not necessarily zero, thus the CLVD is not necessarily zero.

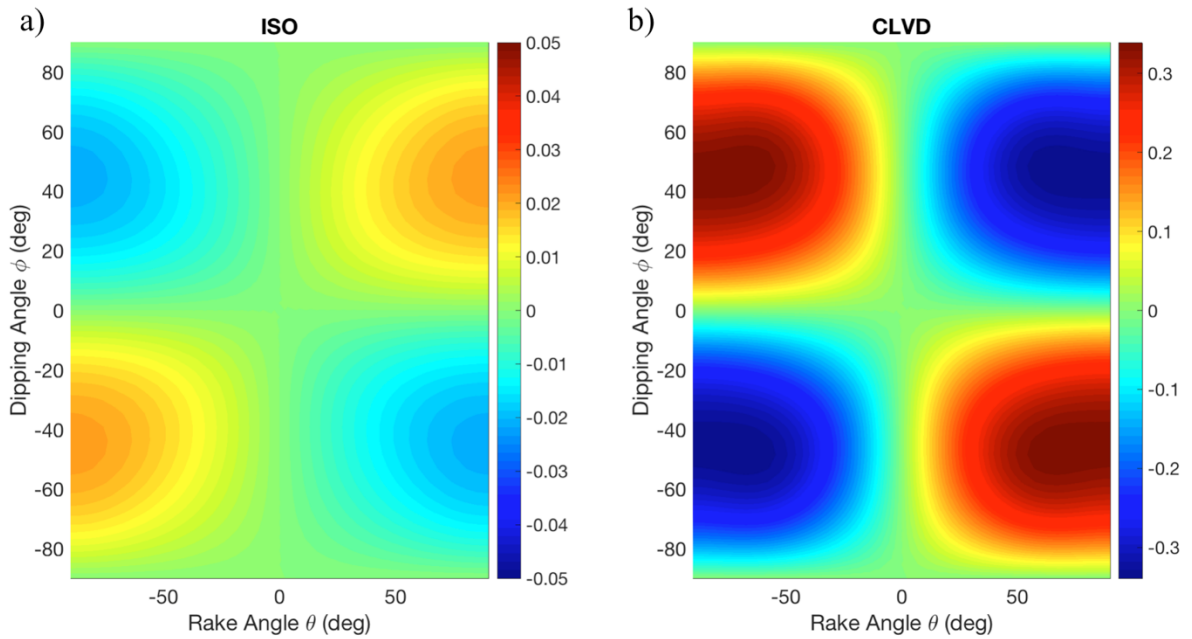


Figure 1.18. Variation of ISO (a) and CLVD (b) with respect to the change of rake angle θ and dipping angle ϕ of a shear slip in the VTI medium. The C_{33} and C_{44} are density normalized to be $100 \text{ km}^2/\text{s}^2$ and $30 \text{ km}^2/\text{s}^2$ The Thomsen parameters are: $\epsilon = 0.05, \gamma = 0.25, \delta = -0.05$.

1.6.2 Deviatoric part of the moment tensor

The deviatoric part of the moment tensor in (1.29) is:

$$\mathbf{m}^* = \frac{1}{2} \begin{pmatrix} -\frac{1}{3}(X - 4C_{66})\sin(\theta)\sin(2\phi) & -2C_{66}\cos(\theta)\sin(\phi) & 2C_{44}\cos(\theta)\cos(\phi) \\ -2C_{66}\cos(\theta)\sin(\phi) & -\frac{1}{3}(X + 2C_{66})\sin(\theta)\sin(2\phi) & 2C_{44}\sin(\theta)\cos(2\phi) \\ 2C_{44}\cos(\theta)\cos(\phi) & 2C_{44}\sin(\theta)\cos(2\phi) & \frac{2}{3}(X - C_{66})\sin(\theta)\sin(2\phi) \end{pmatrix} \quad (1.35)$$

where:

$$X = C_{11} - 2C_{13} + C_{33} \quad (1.36)$$

Deviatoric moment tensors produced by arbitrary shear fault in an arbitrary TTI medium can be simply obtained by rotating the moment tensor in equation (1.35). The elastic parameters C_{11} , C_{13} , and C_{33} which relate to Thomsen parameters ε and δ are always coupled together in X . This explains why we cannot determine the value of ε and δ in the inversion using only the deviatoric part of the moment tensor.

The parameter $\sigma = \frac{C_{33}}{C_{44}}(\varepsilon - \delta)$, which is closely related to the SV-wave anisotropy, is a combination of elastic constants C_{11} , C_{13} , C_{33} , C_{44} :

$$\sigma = -\frac{C_{13}^2 - C_{11}C_{33} + C_{11}C_{44} + 2C_{13}C_{44} + C_{33}C_{44}}{2(C_{33} - C_{44})C_{44}} \quad (1.37)$$

If we take $C_{11} = X + 2C_{13} - C_{33}$ (1.36) into equation (1.37), we have:

$$\sigma = -\frac{C_{13}(C_{13} - 2C_{33} + 4C_{44}) + C_{33}^2 + X(C_{44} - C_{33})}{2(C_{33} - C_{44})C_{44}} \quad (1.38)$$

where X can be inverted in the inversion, since C_{33} and C_{44} are fixed values. In order to determine parameter σ , we need to know the elastic constant C_{13} which could not be independently inverted since it is always coupled together with C_{11} and C_{33} in X . Therefore, we could not accurately resolve SV-wave anisotropy parameter σ .

However, in the case of inversion of anisotropy for medium around deep earthquakes, we could use X^2 to approximate σ if the true Thomsen parameters ε and δ are within certain range. I defined the ratio r to be $r = \sigma / \left(\frac{X}{C_{33}}\right)^2$ and calculated its value for δ from -0.25 to 0.25, ε from 0 to 0.4, and $\frac{C_{44}}{C_{33}} = 0.3$ (which is the typical value at the depth range of deep earthquakes). The normalized ratio $\bar{r} = r / \max(r)$ is presented (Figure 1.19). For negative δ and large ε , the ratio \bar{r} is close to 1, which means that SV-wave anisotropy parameter σ almost linearly varies with parameter X^2 . In this situation, the parameter σ could be reasonably approximated.

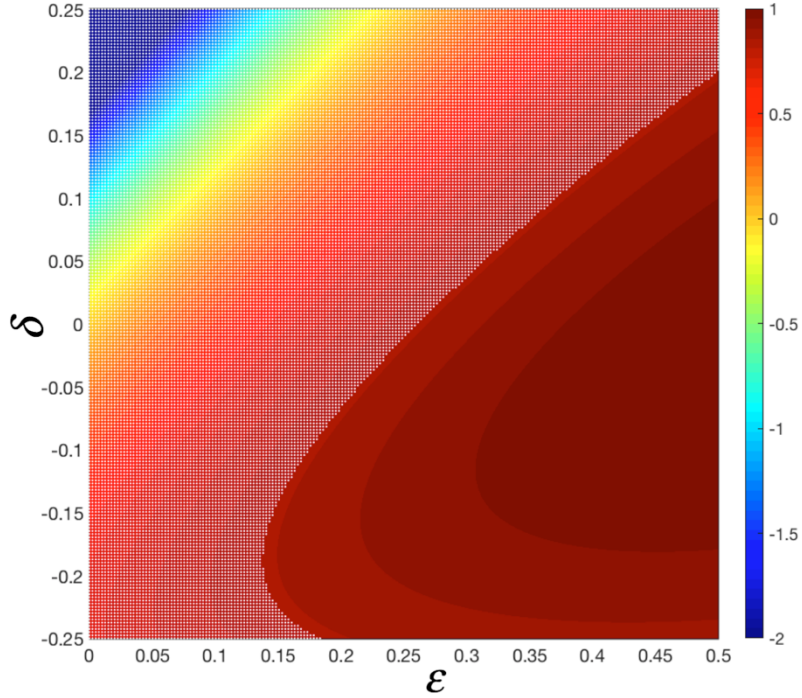


Figure 1.19. Normalized ratio \bar{r} calculated for different ϵ and δ and $\frac{c_{44}}{c_{33}} = 0.3$. The white dots cover area with $\bar{r} < 0.85$. For negative δ and large ϵ , the ratio \bar{r} is close to 1, which means that SV-wave anisotropy almost linearly varies with parameter X^2 .

1.7 Discussion

Our study of intra-slab highly anisotropic structure using deep earthquake moment tensors suggests some interesting future research directions:

- (i) Shear faulting in a tilted transversely isotropic medium can also produce an ISO component in the moment tensor (which would imply (unphysically) an explosion or implosion if analyzed isotropically). The isotropic component of the moment tensor can place constraint on the other two Thomsen parameters ϵ and δ . It may be

advisable to remove the constraint that isotropic component of moment tensor is zero during routine inversion.

- (ii) The intra-slab highly anisotropic structure could have significant effect on shear-wave-splitting measurements (depending on the dimensions of the anisotropic region). These are predicted consequences and I will show some initial numerical results in Chapter 3. More detailed study should be done in the future.
- (iii) We can use moment tensors of intermediate-depth deep earthquakes in the upper and lower Benioff zone (Figure 1.20) to infer their difference in the sense of anisotropy. It may provide seismic evidence to the mineral composition in the double Benioff zone. Using the moment tensors from F-net to investigate the anisotropic structure in a double-Benioff zone can be a promising start.

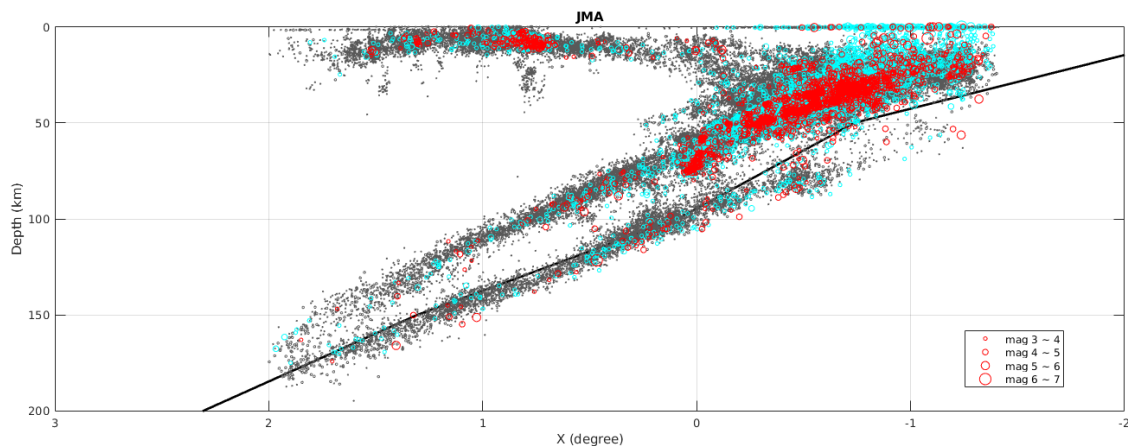


Figure 1.20 West-East vertical cross section of earthquake events in Japan. Earthquakes are within the region with latitude between 38.5°N to 40.9°N , longitude between 140°E to 143°E . Grey circles represent earthquakes from Japan Meteorological Catalog (JMA) with a magnitude between 1.0 and 6.6 from 1998-01-01 to 2017-12-31. Blue circles represent earthquakes from

JMA with a magnitude between 3.0 and 6.6. Red circles represent earthquake events with a magnitude between 3.0 and 6.6 recorded in both JMA and F-net. In cross section, radii of circles indicate earthquake magnitudes. We can clearly see two layers of earthquake events, i.e. the double-Benioff zone.

Furthermore, there are some problems to address in the future:

- (i) The remaining two Thomsen parameters ε and δ are not well determined. This problem may be better addressed if we used the full moment tensor instead of only deviatoric part of moment tensor to constrain the inversion of anisotropy.
- (ii) For some inversion groups (few for GCMT and many for F-net data), there exists ambiguities in determining the TTI symmetry axes. The inversion method may need improvements to eliminate the ambiguity.
- (iii) For those three deep-focus deep earthquake groups whose inverted TTI symmetry axes are parallel to the slab interface, the slab is experiencing extreme flattening at the depth of those earthquake groups (Figure 1.6). This interesting observation will be worth a more detailed study in the future.

1.8 Conclusions

In this chapter, I tested the hypothesis that the deep earthquakes are caused by simple pure shear faulting, but embedded in a tilted transversely isotropic medium. I used the moment tensors from Global CMT catalog to invert for the in-situ anisotropic structure for 22 deep earthquake groups in 6 global subduction slabs. I found that in most studied regions (for both depth between 100 km~300 km and >300km), the inverted TTI symmetry axes are almost perpendicular to the

local slab interface. However, for three deep-focus deep earthquake groups, I found that the inverted TTI symmetry axes are parallel to the slab interface and coincide with local maximum stress direction. This result, that the inverted axes have plausible orientations, provides strong support for the validity of the procedures used. Among all the anisotropy parameters, the SH anisotropy γ is best determined and has a typical value of 25% (5%-46%) which is strong. The SV anisotropy σ is also strong, but less well determined: 60% (30%-90%). The inferred anisotropy can systematically explain the non-double-couple radiation pattern without invoking exotic source processes.

I also used the moment tensor data from F-net catalog to invert for the in-situ anisotropy in Japan. The inferred SH anisotropy γ is also large with a typical value of 21% (4%~39%). The inferred SV anisotropy σ has a typical value of 61% (41%-81%). However, there exists a lot of ambiguity in determining the TTI symmetry axes.

I further showed that a shear dislocation fault in a TTI medium may also produce isotropic component in the moment tensor. This implies that we may want to remove the zero-trace constraint during the routine moment tensor inversion.

2 Effects of Heterogeneity, Anisotropy and Station Coverage on Moment Tensor Inversion of Deep Earthquakes

2.1 Introduction

Seismic moment tensors have been routinely determined either locally or globally by different catalogs (Dziewonski *et al.*, 1981; Kubo *et al.*, 2002; Ekström *et al.*, 2012). The simple linear relationship between the amplitude of free oscillation and the seismic moment tensor established by Gilbert (1971), and the broad deployment of broadband seismometers contribute to this routine process. However, routine determination of moment tensors is based on the assumption that the excitation kernel functions (based on 1d model) are relatively exact and could correctly represent the earth structure (Dziewonski *et al.*, 1981). Although the effect of major structures on wave propagation is well understood, consideration of the effect of near-source medium properties has been lacking.

The CLVD component in the moment tensor of deep earthquakes is commonly observed. Since Knopoff and Randall (1970) and Randall and Knopoff (1970) first proposed that there are significant CLVD components in moment tensors inverted using body waves of several deep earthquakes, several observations have confirmed the existence of a CLVD component in deep earthquakes (Kuge and Kawakatsu, 1993; Henry *et al.*, 2002). However, there are still doubts about what exactly causes the CLVD component. Possible mechanisms including complex fault geometries (Frohlich, 1990; Julian *et al.*, 1998) and complex source structures

have been proposed. The complex source structure could either be unknown heterogeneous structure in the source region (Woodhouse, 1981; Johnston and Langston, 1984; Tada and Shimazaki, 1994), plausible because most deep earthquakes are embedded in heterogeneous subducting slabs, or in-situ anisotropic structures (Kawasaki and Tanimoto, 1981; Vavrycuk, 2004; Li *et al.*, 2018).

The main purpose of this numerical study is to analyze the effect of near-source medium properties such as heterogeneity and anisotropy on the CLVD component in inverted moment tensors of deep earthquakes, apart from the effect of strong intra-slab anisotropy at the source, studied in Chapter 1. Therefore, I suppose all the synthetic earthquakes have simple pure shear dislocations in either isotropic or anisotropic media. I will model synthetic seismograms by applying a 3-D full-elastic staggered-grid FD modeling (Virieux, 1986) using 24 different source fault geometries in five different models. I will show that the heterogeneity near the source only has a minor effect on the CLVD component of inverted moment tensors given a reasonable station coverage. The inverted CLVD component thus represents other source-region properties such as the in-situ anisotropy. Since the metastable olivine wedge (MOW) has been prevalently invoked to explain for the mechanism of deep-focus deep earthquakes (Bina and Wood, 1987; Jiang *et al.*, 2008; Green *et al.*, 2010; Kawakatsu and Yoshioka, 2011) the effect of MOW is tested here. It is shown that the weakly anisotropic (seismic anisotropy $\sim 5\%$) MOW alone could not produce large CLVD components in inverted moment tensors. However, strong in-situ anisotropic structure could produce large CLVD components in inverted moment tensors, as shown in Chapter 1. In addition, I will show that the station coverage does play an important role in moment tensor determination (Satake, 1985). A poor station coverage could generate artifacts in the CLVD components when the effects of

heterogeneity are neglected in kernel functions. However, if we consider the effect of heterogeneous structure in the kernel functions, we could retrieve more precise CLVD values even with a poorer station coverage.

2.2 Methods:

2.2.1 Model Setup

I performed the FD forward modeling using a Ricker wavelet with a central frequency of 0.1Hz as source time function. 441 receivers are evenly distributed on a sphere with a radius of 500km centered at the source (Figure 2.1a). The background medium is isotropic homogeneous with a P-wave velocity 8km/s and S-wave velocity 4.5km/s and is denoted as Model-0. I used the waveforms recorded in Model-0 as our Green's function in the inversion, which is similar to the kernel function used in routine inversion. Note that, the Green's function only contains information of background medium properties. No source-region elastic properties are included in the Green's function.

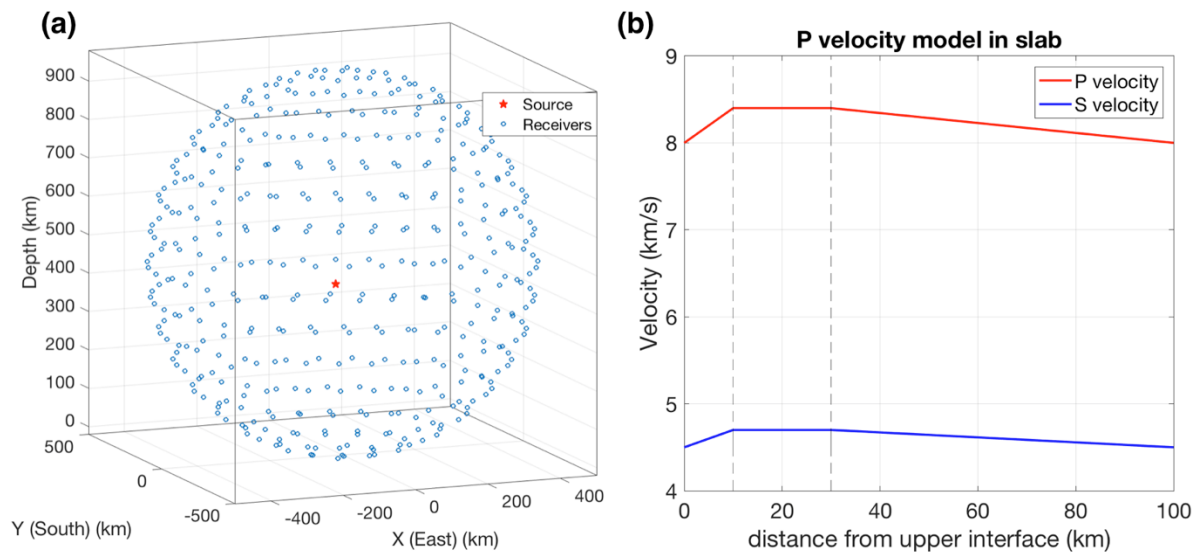


Figure 2.1. **(a)** The source and receiver geometry in FD forward modeling. Red star represents the source. Blues circles represent the receivers. The 441 receivers are evenly distributed on a sphere with a radius of 500km centered at the source. The background $V_P = 8\text{km/s}$ and $V_S=4.5$ km/s. **(b)** P and S velocities in the heterogeneous slab for model-1, 2, 4, and 5 (Figure 2.2 **a, b, d, e**). The highest velocities in the slab are $V_P = 8.4\text{km/s}$ and $V_S=4.7$ km/s, which represent about 5% high-velocity anomaly in the coolest part of the slab.

I also did FD modeling for five other models which introduced heterogeneous or anisotropic structures (Figure 2.2). These five models are:

- (i) Model-1 (Figure 2.2a) adds a $100\text{km} \times 600\text{km} \times 600\text{km}$ heterogeneous slab with strike 180° and dip 40° . The V_P and V_S in the coldest part of the slab is 5% higher than the background velocities (Figure 2.1b). The source is located in the center of the slab with a distance of 20km from the upper interface of the slab.
- (ii) Model-2 (Figure 2.2b) has no heterogeneous slab but adds a $30\text{km} \times 30\text{km} \times 30\text{km}$ highly anisotropic patch around the source region. The anisotropic patch is tilted transversely isotropic (TTI). The TTI symmetry axis is perpendicular to the slab interface in Model-1. The 5 independent elastic components of this TTI medium is described by the V_P and V_S along the TTI symmetry axis and three Thomsen parameters ϵ, γ, δ . Here, $V_P = 8.4\text{km/s}$, $V_S=4.7$ km/s, $\epsilon = 20\%$, $\gamma = 20\%$, $\delta = 0\%$ ($\sigma \sim 64\%$). These anisotropy parameters are consistent with those found above. The source has the same location as the one in Model-1 and is located in the center of the anisotropic patch.

- (iii) Model-3 (Figure 2.2c) adds both heterogeneous slab and anisotropic patch described in Model-1 and Model-2. The source has the same location as the one in Model-1.
- (iv) Model-4 (Figure 2.2d) adds the same heterogeneous slab described in Model-1. In addition, it adds a weak outside slab anisotropic patch. The lower interface of this anisotropic patch is contiguous with the upper interface of the slab. This anisotropic patch has a dimension of $150\text{km} \times 150\text{km} \times 20\text{km}$. The orientation of the TTI symmetry axis is the same as the one in Model-2 and Model-3. And the V_p and V_s along the TTI symmetry axes are the same as the background velocities. The Thomsen parameters are $\epsilon = 0\%$, $\gamma = 6\%$, $\delta = 0\%$, ($\sigma = 0\%$). The source has the same location as the one in Model-1.
- (v) Model-5 (Figure 2.2e) adds the same heterogeneous slab described in Model-1. In addition, to simulate the possible existence of MOW in the earthquake source region, it adds a weakly anisotropic wedge. The MOW is also a TTI medium. Its TTI symmetry axis orientation is parallel to the slab interface. The V_p and V_s along the TTI symmetry axis inside the MOW is 5% slower than the background slab. Its Thomsen parameters are $\epsilon = 0\%$, $\gamma = 5\%$, $\delta = 0\%$, ($\sigma = 0\%$). In 2-D profile of the MOW (Figure 2.2f), the distances of its three tips A, B, and C from the upper slab interface are 20km, 0km, and 40km. The gray lines in Figure 2.2f represent the layered anisotropic structure inside the MOW. The source has the same location as the one in Model-1.

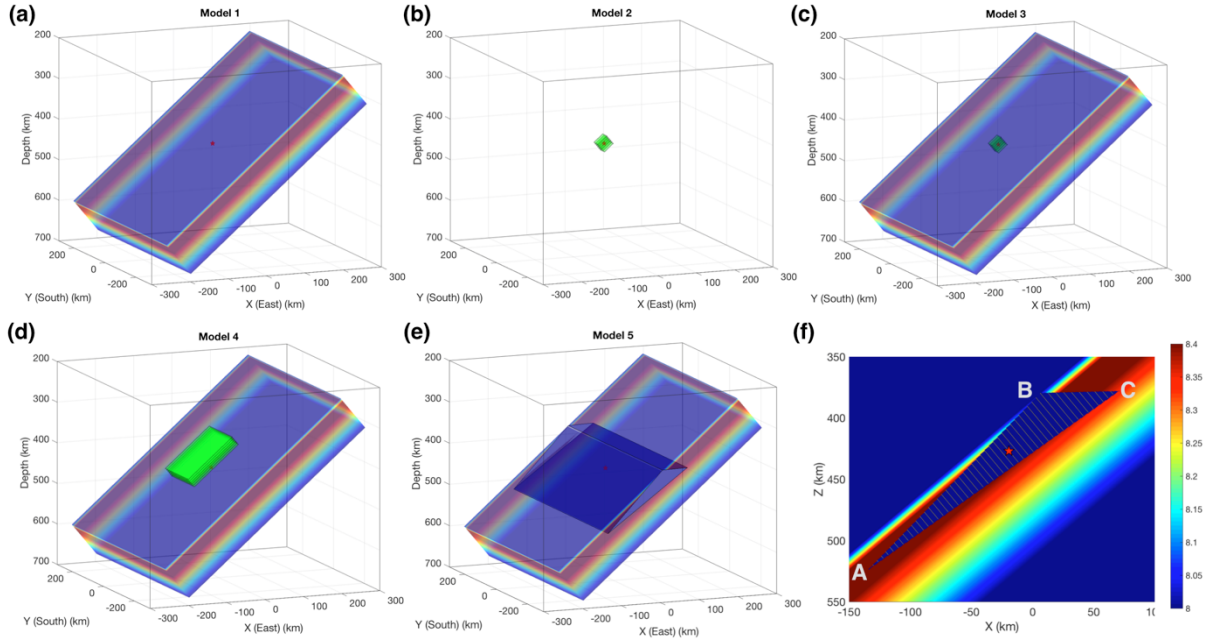


Figure 2.2. Five different models (only show P wave velocities) with a heterogeneous slab or an anisotropic structure. The dipping angle of the slab is 40° . The red star represents the source location. The size of heterogeneous slab is $100\text{km} \times 600\text{km} \times 600\text{km}$. The anisotropic structure is chosen to be tilted transversely isotropic (TTI) medium, which is described by the V_P and V_S (same as background V_P and V_S) along the TTI symmetry axis, and three Thomsen parameters ϵ, γ, δ . In Model-2, 3, and 4, the TTI symmetry axis is perpendicular to the slab interface. In Model-5, the TTI symmetry axis is parallel to the slab interface. For Model-2 and 3, the dimension of the anisotropic patch is $30\text{km} \times 30\text{km} \times 30\text{km}$ and the three Thomsen parameters are $\epsilon = 20\%, \gamma = 20\%, \delta = 0\%$, which represents a strong in-situ anisotropic structure. For model-4, the anisotropic patch is $150\text{km} \times 150\text{km} \times 20\text{km}$ and the $\epsilon = 0\%, \gamma = 6\%, \delta = 0\%, \sigma = 0\%$, which represents a weak outside slab anisotropic structure. For Model-5, the $\epsilon = 0\%, \gamma = 5\%, \delta = 0\%, \sigma = 0\%$, which represents a weakly anisotropic MOW inside the slab. (a) Model-1 with only heterogeneous slab. (b) Model-2 with only strong

anisotropic patch in the source region. (c) Model-3 with both heterogeneous slab and strong anisotropic patch in the source region. (d) Model-4 with heterogeneous slab and weakly anisotropic patch outside the slab. (e) Model-5 with heterogeneous slab and weakly anisotropic MOW inside the slab. (f) 2D velocity profile of Model-5. The distance of three tips of MOW A, B, and C to the slab upper interface is 20km, 0km, and 40km.

2.2.2 Inversion Methods

I randomly generated 24 shear dislocation sources with different fault geometries. I then computed the moment tensors (Aki and Richards, 2002) using the elastic tensor and fault geometry following equation (1.1).

These synthetic moment tensors were used as source mechanisms together with the corresponding kernel function in each Model- J (e.g. Model- J , $J = 1,2,3,4,5$) to produce synthetic waveforms denoted by $u_k^J(\mathbf{r}, t)$, which represents the k -th component of far-field displacement recorded at receiver \mathbf{r} . The relationship between far-field displacement field, source moment tensor and the Green's function G (or the kernel function) is shown in equation (2.1).

$$u_k^J(\mathbf{r}, t) = G_{kp,q}^J(\mathbf{r}, t) m_{pq} . \quad (2.1)$$

The Green's function G_{kp}^J represents the k -th component of the displacement at \mathbf{r} due to a single force along the p -th direction at the source position in Model- J . The subscript $, q$ represents spatial derivative along q -th direction in the source region.

After I obtained synthetic waveforms, a least-squares method was applied to invert for the source moment tensors using the Green's function obtained in the homogeneous isotropic

Model-0. I minimized the objective function (2.2) to find the source moment tensor m_{pq} and the time shift τ_r at receiver \mathbf{r} to minimize the difference between the synthetic waveform and the observed waveform for direct P waves.

$$L(m_{pq}^J, \tau_r^J) = \sum_{\mathbf{r}} \sum_{k=1}^3 \int [u_k^J(\mathbf{r}, t + \tau_r^J) - m_{pq}^J G_{kp,q}^0(\mathbf{r}, t)]^2 dt. \quad (2.2)$$

Using Voigt notation to simplify tensors:

$$11 \rightarrow 1, 22 \rightarrow 2, 33 \rightarrow 3, 12 \rightarrow 6, 13 \rightarrow 5, 23 \rightarrow 4,$$

$$\begin{aligned} M_{\alpha}^J &= m_{pq}^J \\ K_{k1}^0 &= G_{k1,1}^0, K_{k2}^0 = G_{k2,2}^0, K_{k3}^0 = G_{k3,3}^0 \\ K_{k4}^0 &= G_{k2,3}^0 + G_{k3,2}^0 \\ K_{k5}^0 &= G_{k3,1}^0 + G_{k1,3}^0 \\ K_{k6}^0 &= G_{k1,2}^0 + G_{k2,1}^0 \\ \alpha &= 1, \dots, 6; \quad p, q, k = 1, 2, 3 \end{aligned} \quad (2.3)$$

By applying partial derivative with respect to M_{α}^J and τ_r^J , we have:

$$\frac{\partial L(M_{\alpha}^J, \tau_r^J)}{\partial M_{\alpha}^J} = -2 \sum_{\mathbf{r}} \sum_{k=1}^3 \int [u_k^J(\mathbf{r}, t + \tau_r^J) K_{kp}^0 - K_{kp}^0 K_{kq}^0 m_q^J] dt = 0, \quad (2.4)$$

and:

$$\frac{\partial L(M_{\alpha}^J, \tau_r^J)}{\partial \tau_r^J} = 2 \sum_{k=1}^3 \int \left\{ [u_k^J(\mathbf{r}, t + \tau_r^J) - K_{kq}^0 M_{\alpha}^J] \frac{\partial u_k^J(\mathbf{r}, t + \tau_r^J)}{\partial \tau_r^J} \right\} dt = 0. \quad (2.5)$$

In the inversion, I first set $\tau_r = 0$ and use equation (2.4) to determine the moment tensor M_{α}^J . And then put M_{α}^J into equation (2.5) to solve for τ_r for each receiver. I repeated this procedure and iteratively determine both moment tensor M_{α}^J and the shift time τ_r .

2.3 Numerical Results

I first present comparisons between CLVD components of inverted moment tensors and true moment tensors for the 5 different models under reasonable station coverages (perfect station coverage and stations only in the lower hemisphere).

2.3.1 Case 1: Perfect station coverage

I first analyze the situation with perfect station coverage where all 441 receivers were used for the least-square inversion (Figure 2.3a). In this situation, there is full coverage for both up-going and down-going direct arrivals. Figure 2.4 contains the comparison between inverted CLVD components and true CLVD components for 24 earthquakes in five different models. I use $Err^{(J)}$ to denote the root mean squares (RMS) error between inverted CLVD components and true CLVD components for Model- J ($J = 1,2,3,4,5$). In this case, $Err^{(1)} \approx 0.008$, $Err^{(2)} \approx 0.023$, $Err^{(3)} \approx 0.036$, $Err^{(4)} \approx 0.008$, $Err^{(5)} \approx 0.007$. Notice that the true moment tensors are actually pure double couples for Model-1 and 4 because a shear dislocation source embedded in an isotropic homogeneous structure will not produce non-double-couple components. For Model-2 and 3, shear dislocations embedded in a strong anisotropic medium will produce large CLVD component based on equation (1.1). The largest CLVD component in this test is about 12.6%. For Model-5, the weakly anisotropic MOW contributes a small amount of CLVD component (1.9% on average) to the moment tensors. The inversion result shows that for perfect station coverage, the heterogeneous structure such as a subducting slab (Figure 2.2a) and the outside slab weakly anisotropic structure (Figure 2.2d) has a very little effect on the CLVD components of moment tensors (Figure 2.4a, d). The inverted CLVD

components for Model-1 and 4 are close to zero (0.8% on average). For Model-2, 3, and 5 the CLVD components in the inverted moment tensors actually represent other source properties. In our study, the anisotropic structure is responsible for the apparent CLVD components in inverted moment tensors. A strong in-situ anisotropic patch could lead to large CLVD components in inverted moment tensors, while a weakly anisotropic MOW alone could not produce large CLVD components in inverted moment tensors.

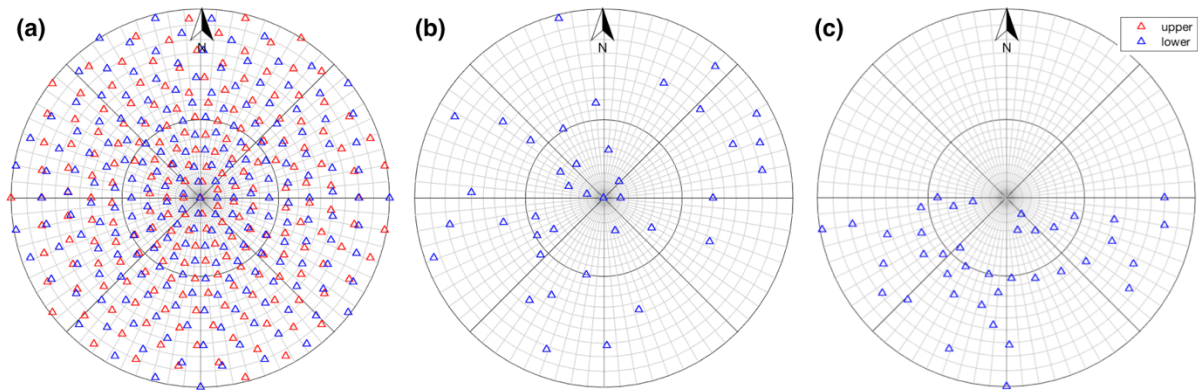


Figure 2.3. Lower hemisphere projection of station distributions for three cases. Upper direction represents North and right direction represent East. Red triangles represent receivers in the upper hemisphere, blue triangles represent lower hemisphere. **(a)** Perfect station coverage including all 441 stations. **(b)** 40 stations in the lower hemisphere are randomly selected. The stations are evenly distributed by azimuth and distance. **(c)** Azimuth-biased station coverage with 40 stations in the lower hemisphere in the southern part selected.

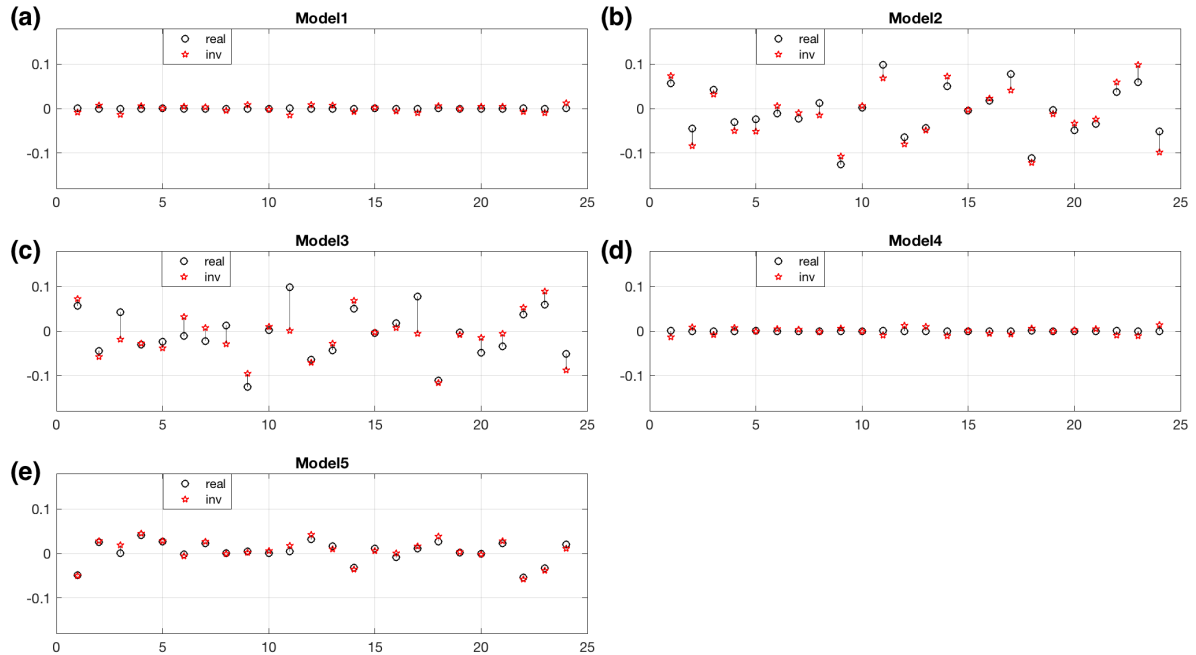


Figure 2.4. Comparison between CLVD components of inverted moment tensors and CLVD components of true moment tensors for 24 earthquake events for five models with perfect station coverage. **(a)** Comparison for Model-1. Inverted CLVD components are very close to the true ones, which are essentially zeros. **(b)** Comparison for Model-2. Inverted CLVD components are close to the true ones. Non-zeros CLVDs are caused by the anisotropic structure in the source region. **(c)** Comparison for Model-3. Inverted CLVD components are still close to the true ones. The error is a bit larger than the results in Model-2. **(d)** Comparison for Model-4. The results are similar to the ones in Model-1. **(e)** Comparison for Model-5. Inverted CLVD components are very close to the true ones.

2.3.2 Case 2: Stations only in the lower hemisphere

In the real world, there seldom is extensive station coverage for up-going direct arrivals. Even for a 600km depth earthquake, the station coverage could only extend to about 12° from the epicenter in the upper hemisphere (Frohlich, 2006). To make the station coverage here

consistent with the real world, I randomly selected 40 stations only from the lower hemisphere used for inversion (Figure 2.3b). Figure 2.5 contains the comparison between the inverted CLVD components and true CLVD components for this type of station coverage. For this poorer but more realistic station coverage, the CLVD components in inverted moment tensors have larger errors than those with perfect station coverage. The RMS errors of inverted CLVD components are $Err^{(1)} \approx 0.016, Err^{(2)} \approx 0.040, Err^{(3)} \approx 0.054, Err^{(4)} \approx 0.016, Err^{(5)} \approx 0.016$ for each model. Although the RMS errors doubled for Model-1, 4, and 5, our inverted moment tensors are still very close to the true mechanisms. This implies that with a reasonable station coverage, it is unlikely that apparent CLVD components of moment tensors are purely caused by source heterogeneous structures such as subducting slab, neither could be caused by outside slab weakly anisotropic structure nor in-situ weakly anisotropic MOW. Other source medium properties such as strong in-situ anisotropic structures could be responsible for the apparent CLVD components.

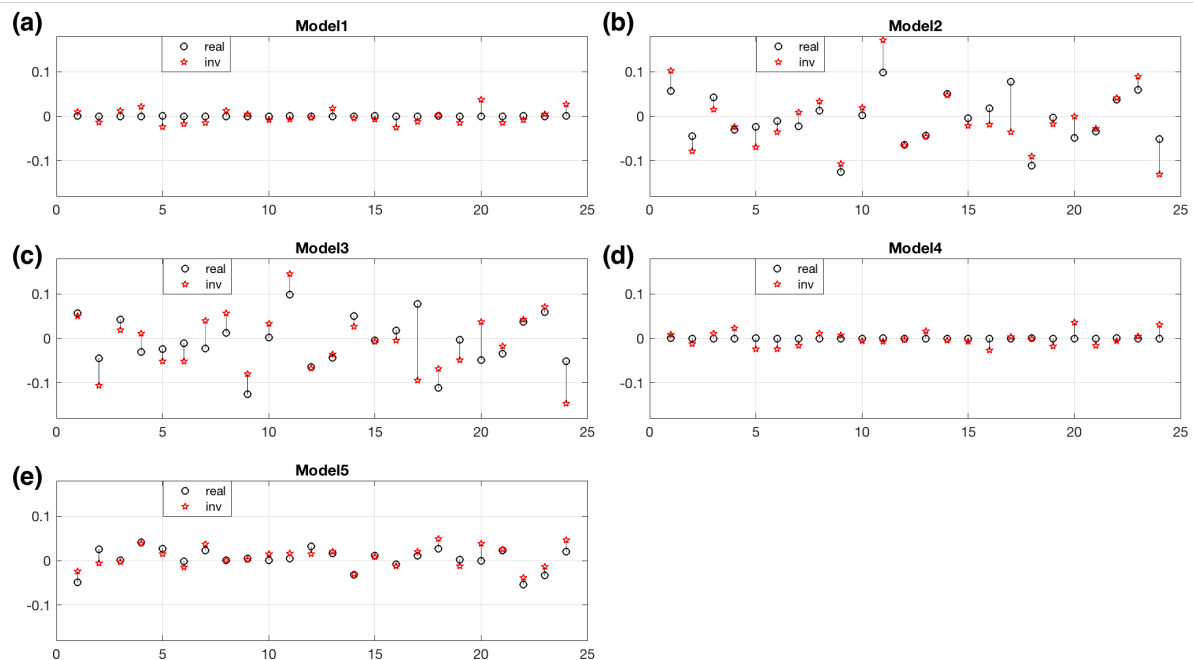


Figure 2.5. Comparison between CLVD components of inverted moment tensors and CLVD components of true moment tensors for 24 earthquake events for five models. The moment tensors are inverted using 40 randomly selected stations only in lower hemisphere. For this station coverage, the inverted CLVD components have larger errors for all 4 Models. But the results are still reasonable. (a-e) Comparison for Model-1~5.

2.3.3 Case 3: Azimuth-biased station coverage

I then present comparisons between inverted moment tensors and true moment tensors for 5 different models with azimuth-biased station coverage.

Could very poor station coverage cause large artifacts in CLVD components in inverted moment tensors? Our answer is YES, by investigating an azimuth-biased station distribution (Figure 2.3c). The RMS errors of CLVD components for models are $Err^{(1)} \approx 0.038$, $Err^{(2)} \approx 0.058$, $Err^{(3)} \approx 0.097$, $Err^{(4)} \approx 0.035$, $Err^{(5)} \approx 0.033$. I observed that on average about 3.7% CLVD artifacts are introduced into inverted moment tensors in Model-1 and 4 (Figure 2.6) while the biggest one can almost reach 12%, even though the true source mechanism is a pure double couple. The RMS errors for Model-2 and 3 also increases a lot. In Model-3, the strength of inverted CLVD component for earthquake event 1 and 14 are 24% and 25%, which is much larger than the true values 6% and 5%. This indicates that very poor station coverage may cause spuriously large CLVD components in inverted moment tensors when the source is embedded in strong anisotropic medium. In Model-5, the RMS error also increases a lot. The largest error in CLVD components between inverted and true moment tensors is about 8%.

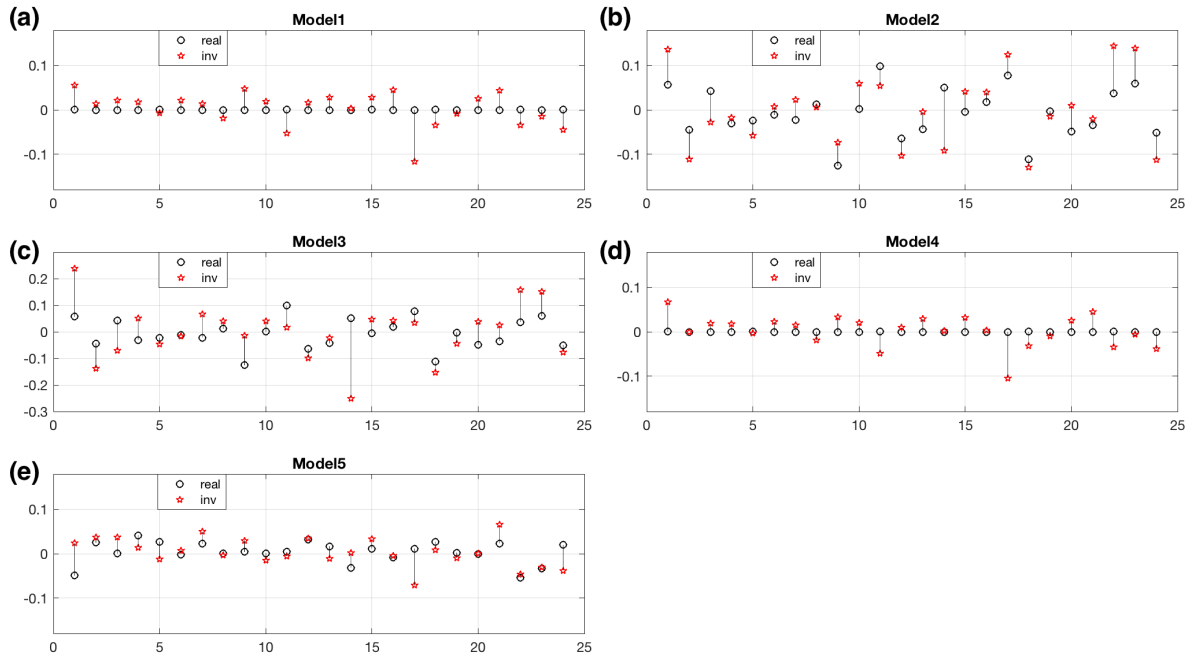


Figure 2.6. Comparison between CLVD components of inverted moment tensors and CLVD components of true moment tensors for 24 earthquake events for five models. The moment tensors are inverted using 40 randomly selected azimuth-biased stations. This poor station distribution contributes large artifacts to the inverted CLVD components. (a-e) Comparison for Model-1~5.

2.3.4 Case 4: Same station distribution as Case 3 with Green's function considering slab effects

What if we include the effect of the heterogeneous slab in our Green's function for Models with the existence of heterogeneous slab? To do so, I used the waveforms recorded in Model-1 (Figure 2.2a) instead of Model-0 as our new Green's function. I then performed the same inversion procedures to invert for moment tensors for Model-1, 3, 4, and 5 using the azimuth-biased station coverage. Figure 2.7 contains the comparison between the inverted CLVD components and true CLVD components. The RMS errors of CLVD components for five

models are $Err^{(1)} \approx 0.001, Err^{(3)} \approx 0.066, Err^{(4)} \approx 0.006, Err^{(5)} \approx 0.027$. The error of CLVD components in Model-1 and 4 is decreased a lot. The inverted moment tensors are almost pure double-couple mechanisms which are even more precise than the case with perfect station coverage. However, for Model-3 and 5, although the error has been decreased a lot, the inverted CLVD components still possesses large errors.

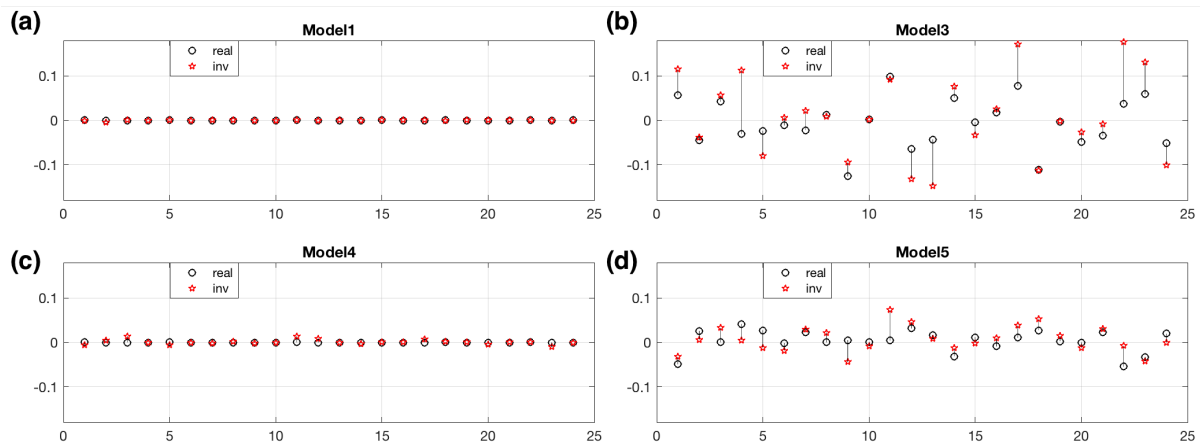


Figure 2.7. Comparison between CLVD components in inverted moment tensors and true CLVDs. I used the same station coverage as the one in Figure 2.6. But I used different Green's function which takes effect of the heterogeneous slab into account. Although a poor station coverage is used, I got an even better result for Model-1 and 4. For Model-3 and 5, the error is decreased a little bit. **(a)** Comparison for Model-1. **(b)** Comparison for Model-3. **(c)** Comparison for Model-4. **(d)** Comparison for Model-5.

2.4 Discussion

In case 1 and 2 where the station coverage is reasonable, since the true mechanism is a pure double couple for Model-1 and 4, the inverted CLVD components represent the artefacts

introduced by the heterogeneous slab and the outside-slab anisotropic structure. For case 1, the average errors are about $Err^{(1)} \approx 0.8\%$, $Err^{(4)} \approx 0.8\%$. For case 2, the average errors are about $Err^{(1)} \approx 1.6\%$, $Err^{(4)} \approx 1.6\%$. This indicates that around 1.6% of CLVD components could be introduced by the heterogeneous slab and outside slab anisotropic structure with a reasonable station coverage. The inverted large CLVD components in Model-2 and 3 in case 1 and 2 thus, represent some other near-source medium property, such as the strong in-situ anisotropic structure in Chapter 1. For case 3, the big CLVD errors in Model-1 and 4 confirm that it is important to have good station coverage to retrieve precise CLVD components in inverted moment tensors.

In Model-4, I mainly aimed at testing whether outside-slab weakly anisotropic structure could cause apparent CLVD component in moment tensors. I decided this anisotropic patch dimension and anisotropy strength based on the shear-wave splitting studies where a typical traveltime difference between fast and slow shear waves is about 1 second (Nowacki *et al.*, 2015). Our inversion results show that the outside-slab weakly anisotropic structure has nearly no effects on the CLVD component in moment tensors compared with the heterogeneous slab because the inverted CLVDs in Model-4 are highly correlated with the ones in Model-1 for all four cases in this study (Figure 2.8).

Shear-wave splitting studies could tell the general traveltime difference between fast wave and slow wave caused by the averaged anisotropy on the ray path. However, they could not resolve in which part of the raypath the anisotropic structure resides. Based on our numerical study, the outside-slab weakly anisotropic structure has very small effect on observed CLVD components while the in-situ anisotropic structure could cause significant CLVD components.

The observation of large CLVD components thus indicates that the anisotropy observed using the shear-wave splitting method may be strong but localized anisotropy residing in the source region and could be responsible for the occurrence of CLVD components in moment tensors.

In case 4, I found that if I include slab information in the Green's function, the inversion result could be even better resolved for an azimuth-biased station coverage for Model-1 and 4 compared with perfect station coverage. For Model-3, the RMS error is decreased by 26% compared with the RMS error using Green's function in an isotropic homogeneous medium. This suggests that it would be intriguing to consider the effect of the heterogeneous subducting slab in the kernel functions during routine inversion to improve the accuracy of the CLVD components.

I also tested the effect of the weakly anisotropic MOW on the CLVD components of moment tensors. I selected the MOW model with a similar dimension and velocity structures to the ones in previous studies (Kirby *et al.*, 1996; Jiang *et al.*, 2008). I found that the inverted CLVD component in all 4 cases in this study is reasonably close to the true values, and the MOW could only contribute a small amount of CLVD component to moment tensors. This indicates that MOW alone cannot produce the prevalently observed large CLVD components in the moment tensors of deep earthquakes. And there may exist other structures such as strong anisotropic fabric layers around deep earthquakes (Li *et al.*, 2018).

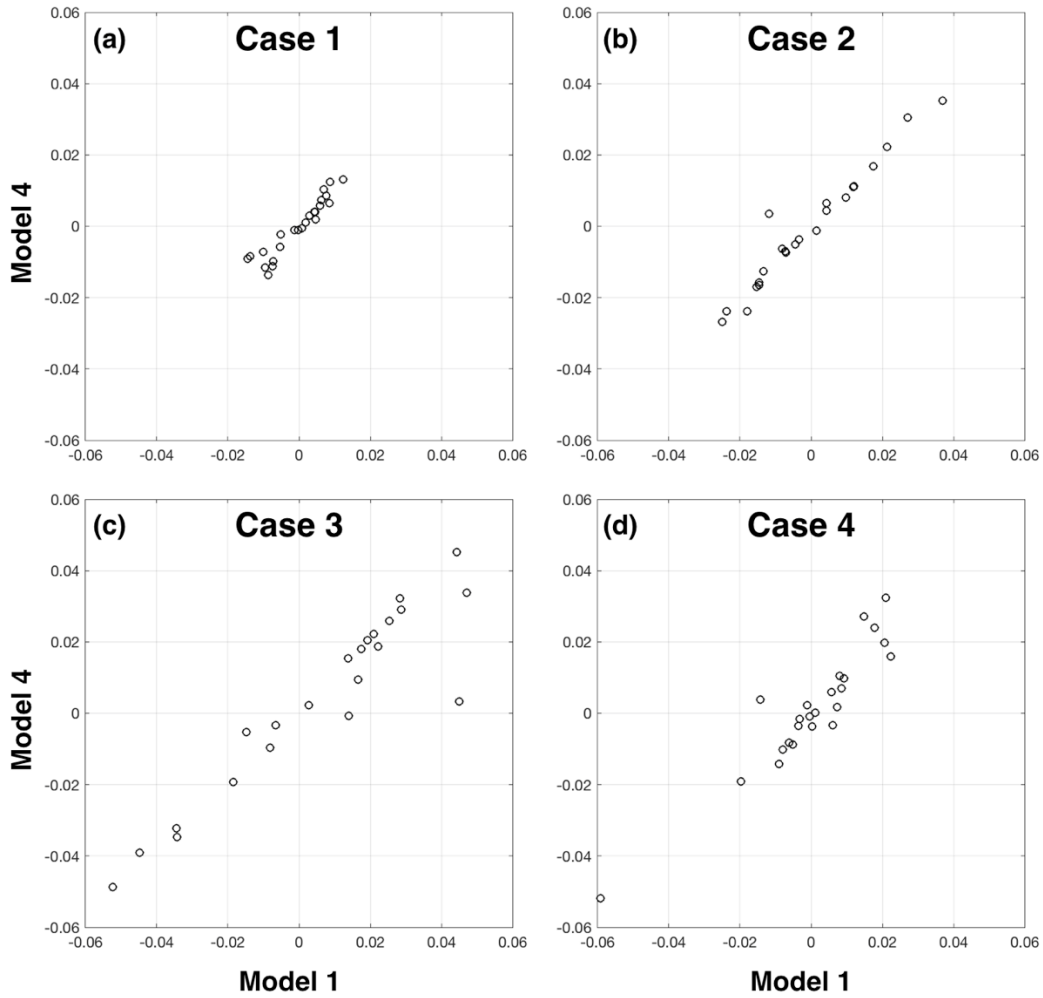


Figure 2.8. (a-d) Comparison between the inverted CLVD component in Model-1 and Model-4 for 4 cases. The inverted CLVDs in Model-4 are highly correlated with the ones in Model-1.

2.5 Conclusions

In this numerical study, I analyzed the inverted CLVD components of 24 synthetic earthquakes in five Models for four different cases. I showed that, with an even station distribution (case 1 and case 2), the heterogeneous slab structure in the source region (Model-1) and the outside-

slab weakly anisotropic structure (Model-4) could only introduce around 1.6% CLVD components on average in inverted moment tensors. The inverted large CLVD components in Chapter 1 our study represent other source properties such as the strong in-situ anisotropic structure (Model-2 and 3). I also found that outside slab weakly anisotropic structure has nearly no effect on the inverted CLVD components since the inverted CLVD components are highly correlated for Model-1 and 4 in case 1, 2, 3, 4. Furthermore, I found that the existence of weakly anisotropic MOW (Model-5) alone could not produce large CLVD components in moment tensors. The strong anisotropic structure in the source region could be a possible mechanism to produce significant CLVD components in inverted moment tensors.

I found that the poor station coverage (case 3) could introduce large error into inverted moment tensors. On average, around 3.7% CLVD components could be introduced while the true mechanism is a pure double couple (Model-1 and 4). When the true mechanism contains large CLVD components caused by in-situ strong anisotropic structure (Model-2 and 3), spuriously high CLVD components would be obtained in the inversion.

However, if the effect of the heterogeneous slab is considered in the kernel function, even with an azimuth-biased station coverage, we could obtain more precise CLVD components. This indicates that consideration of heterogeneous slab structure in kernel/or Green's functions of routine moment tensor inversion is highly recommended.

3 Effect of strong intra-slab anisotropic structure on subduction zone shear-wave-splitting measurements

3.1 Introduction

Resolving spatial distribution of seismic anisotropy in subduction zones is important because anisotropy is thought as a proxy to map mantle flow information (e.g., Smith *et al.*, 2001; Long and Silver, 2008; Long and Becker, 2010; Long, 2013; Hu *et al.*, 2017), which in turn controls surface expressions such as sea-level changes, mountain building, volcanic activities, outgassing of volatiles into the ocean/air, and seismicity.

Unfortunately, seismic anisotropy inside the slab (i.e., intra-slab anisotropy) was often disregarded as a potential source for shear wave splitting (SWS) analyses in most high-resolution studies targeting subduction zone anisotropy because it was assumed that the intra-slab anisotropy is not strong and the relative path length through the slab is short compared with the rest of the upper mantle (Eakin *et al.*, 2016). As a consequence, the observed anisotropy has been frequently attributed to either above (Levin *et al.*, 2002) or below the slab (Song and Kawakatsu, 2012; Lynner *et al.*, 2017). In light of evidence for the existence of highly anisotropic intra-slab structure (Li *et al.*, 2018; Romanowicz, 2018), this assumption should be re-examined.

Seismic anisotropy in subduction zones is commonly studied by SWS, which is an effective tool used to study the overall anisotropy along the propagation path (Vinnik *et al.*, 1984; Kaneshima, 1990; Silver and Chan, 1991; Wookey *et al.*, 2002; Nakajima and Hasegawa,

2004; Crampin and Peacock, 2008; Song and Kawakatsu, 2012; Lynner and Long, 2015). However, it is challenging, if not impossible, (Long and Silver, 2008; Eakin *et al.*, 2015; Long *et al.*, 2016) to pinpoint the location on the ray path where the splitting occurs (e.g., inside or outside of the slab). In addition, the orientation of the fast S polarization has been observed in subduction zones to vary with the earthquake backazimuth (e.g., Smith *et al.*, 2001; Karato *et al.*, 2008; Long and Silver, 2009), not the simple trench-parallel or trench perpendicular direction. The interpretations of the complicated observed SWS polarization patterns are mainly dwelling upon complex mantle flow (e.g., Smith *et al.*, 2001). Is this the only interpretation? I investigate the effect of the strong anisotropic structure in a dipping slab using the propagator matrix method (Peng, 2019) in this chapter.

3.2 Methods

All the following derivations are based on an orthogonal coordinate system with 1 and 2 representing horizontal direction and 3 the vertical direction (downward is positive).

3.2.1 Solution of Green-Christoffel equation

The wave equation for an arbitrary locally-homogeneous (stiffness tensor is locally constant and can be taken out of the spatial derivative) anisotropic medium is:

$$-\rho\omega^2 u_i = \frac{\partial}{\partial x_i} c_{ijkl} \frac{1}{2} \left(\frac{\partial u_l}{\partial x_k} + \frac{\partial u_k}{\partial x_l} \right) = c_{ijkl} \frac{\partial}{\partial x_j} \frac{\partial}{\partial x_l} u_k, \quad i, j, k, l = 1, 2, 3, \quad (3.1)$$

where u_i represents the displacement.

The plane wave solution in the frequency domain is: $\mathbf{u}(\mathbf{x}, \omega) = A \mathbf{t} e^{i\omega \mathbf{p} \cdot \mathbf{x}}$. Here, A is the plane wave amplitude, $\mathbf{t} = (t_1, t_2, t_3)$ is the unit polarization vector, $\mathbf{p} = (p_1, p_2, p_3)$ is the slowness vector.

The problem I choose to solve is: suppose the horizontal components p_1, p_2 of the slowness vector \mathbf{p} are known, then what are 1) the vertical slowness p_3 and 2) the polarization vector \mathbf{t} for this propagation direction?

Take the plane wave solution into equation (3.1):

$$-\rho \omega^2 A t_i e^{i\omega \mathbf{p} \cdot \mathbf{x}} = -c_{ijkl} \omega^2 A p_j p_l t_k e^{i\omega \mathbf{p} \cdot \mathbf{x}}, \quad (3.2)$$

which may be simplified as:

$$\left(\delta_{ik} - \bar{c}_{ijkl} p_j p_l \right) t_k = 0, \quad (3.3)$$

where $\bar{c}_{ijkl} = \frac{c_{ijkl}}{\rho}$ is the density normalized elastic tensor. Denoting the matrix $a_{ik} = \delta_{ik} -$

$\bar{c}_{ijkl} p_j p_l$ as \mathbf{A}_p , equation (3.3) can be rewritten as:

$$\mathbf{A}_p \mathbf{t} = \mathbf{0}. \quad (3.4)$$

Equation (3.4) has non-trivial solutions when:

$$\det(\mathbf{A}_p) = 0. \quad (3.5)$$

Equation (3.5) yields a 6th order polynomial equation for solving p_3 :

$$\sum_{k=0}^6 c_k p_3^k = 0 \quad (3.6)$$

Equation (3.6) has 6 roots $p_3^{(n)}$, $n = 1, 2, \dots, 6$. If the 6 roots are real and unique, they represent the vertical slowness of 1: upgoing slow S, 2: upgoing fast S, 3: upgoing P, 4:

downgoing P, 5: downgoing fast S, and 6: downgoing slow S (the positive direction is downgoing and the roots are sorted in ascending order).

For each root $p_3^{(n)}$, $n = 1, 2, \dots, 6$, I took it into equation (3.4) to calculate the matrix $\mathbf{A}_p^{(n)}$ and solve for the corresponding polarization vector $\mathbf{t}^{(n)}$. To solve this equation, I applied singular value decomposition (SVD) to the matrix $\mathbf{A}_p^{(n)}$:

$$\mathbf{A}_p^{(n)} = \mathbf{U}^{(n)} \mathbf{\Sigma}^{(n)} \mathbf{V}^{(n)*}, \quad (3.7)$$

where $\mathbf{U}^{(n)}$ and $\mathbf{V}^{(n)}$ are unitary matrices and $*$ represents the conjugate transpose. $\mathbf{\Sigma}^{(n)}$ is a diagonal matrix with singular values $S_1^{(n)}, S_2^{(n)}, S_3^{(n)}$ among which and at least one singular value is zero, because the absolute determinant of \mathbf{S} is the same as the absolute determinant of diagonal matrix \mathbf{A}_p , which is zero.

Let $\mathbf{y}^{(n)} = \mathbf{V}^{(n)*} \mathbf{t}^{(n)}$, from equations (3.4) and (3.7), we have $\mathbf{U}^{(n)*} \mathbf{U}^{(n)} \mathbf{\Sigma}^{(n)} \mathbf{y}^{(n)} = \mathbf{U}^{(n)*} \mathbf{0}$. Since $\mathbf{U}^{(n)*} \mathbf{U}^{(n)}$ is an identity matrix and $\mathbf{U}^{(n)*} \mathbf{0} = \mathbf{0}$, we have:

$$\begin{pmatrix} S_1^{(n)} & 0 & 0 \\ 0 & S_2^{(n)} & 0 \\ 0 & 0 & S_3^{(n)} \end{pmatrix} \begin{pmatrix} y_1^{(n)} \\ y_2^{(n)} \\ y_3^{(n)} \end{pmatrix} = \begin{pmatrix} 0 \\ 0 \\ 0 \end{pmatrix}. \quad (3.8)$$

If $S_k^{(n)} = 0$, $y_k^{(n)}$ is undetermined and it may be assigned a random value. If $S_k^{(n)} \neq 0$, $y_k^{(n)} = 0$, then

$$\mathbf{t}^{(n)} = \mathbf{V}^{(n)} \mathbf{V}^{(n)*} \mathbf{t}^{(n)} = \mathbf{V}^{(n)} \mathbf{y}^{(n)} = \begin{pmatrix} \mathbf{v}_1^{(n)} & \mathbf{v}_2^{(n)} & \mathbf{v}_3^{(n)} \end{pmatrix} \begin{pmatrix} y_1^{(n)} \\ y_2^{(n)} \\ y_3^{(n)} \end{pmatrix} = y_1^{(n)} \mathbf{v}_1^{(n)} + y_2^{(n)} \mathbf{v}_2^{(n)} + y_3^{(n)} \mathbf{v}_3^{(n)}, \quad (3.9)$$

where $\mathbf{v}_i^{(n)}$, $i = 1, 2, 3$ are the column vectors of the unitary matrix $\mathbf{V}^{(n)}$.

I then normalize the polarization vector and finally get solutions for 6 plane waves:

$$\mathbf{u}^{(n)}(\mathbf{x}, \omega) = A_n \mathbf{t}^{(n)} \cdot e^{i\omega \mathbf{p}^{(n)} \cdot \mathbf{x}}, \quad n = 1, 2, \dots, 6. \quad (3.10)$$

3.2.2 Propagator matrix in layered medium

A layered medium has c_{ijkl} which varies only in the 3-direction. The strain and stress tensor for plane waves in the frequency domain within a layer are:

$$\varepsilon_{ij} = \frac{1}{2} \left(\frac{\partial u_i}{\partial x_j} + \frac{\partial u_j}{\partial x_i} \right) = \frac{1}{2} i\omega (t_i p_j + t_j p_i) = i\omega \bar{\varepsilon}_{ij}, \quad (3.11)$$

and:

$$\sigma_{ij} = c_{ijkl} \varepsilon_{kl} = i\omega c_{ijkl} \bar{\varepsilon}_{kl} = i\omega \cdot \bar{\sigma}_{ij} \quad (3.12)$$

where $\bar{\varepsilon}_{ij}$ and $\bar{\sigma}_{ij}$ represents the normalized strain tensor and stress tensor respectively.

The traction on a surface with normal unit vector \mathbf{n} is:

$$\bar{T}_i = \bar{\sigma}_{ij} n_j \quad (3.13)$$

Suppose the amplitudes of the 6 plane waves obtained in (3.10) are: A_n , $n = 1, 2, \dots, 6$.

Define the vector $\mathbf{B} = (u_1, u_2, u_3, \bar{T}_1, \bar{T}_2, \bar{T}_3)^T$ to describe to displacement and traction on the

surface boundary between two layer (superscript T represents transpose operations) (Figure 3.1). \mathbf{B} may be calculated using matrix \mathbf{S} , as $\mathbf{B} = \mathbf{S}\mathbf{A}$:

$$\begin{pmatrix} u_1 \\ u_2 \\ u_3 \\ \bar{T}_1 \\ \bar{T}_2 \\ \bar{T}_3 \end{pmatrix} = \begin{pmatrix} t_1^{(1)} & t_1^{(2)} & t_1^{(3)} & t_1^{(4)} & t_1^{(5)} & t_1^{(6)} \\ t_2^{(1)} & t_2^{(2)} & t_2^{(3)} & t_2^{(4)} & t_2^{(5)} & t_2^{(6)} \\ t_3^{(1)} & t_3^{(2)} & t_3^{(3)} & t_3^{(4)} & t_3^{(5)} & t_3^{(6)} \\ \bar{T}_1^{(1)} & \bar{T}_1^{(2)} & \bar{T}_1^{(3)} & \bar{T}_1^{(4)} & \bar{T}_1^{(5)} & \bar{T}_1^{(6)} \\ \bar{T}_2^{(1)} & \bar{T}_2^{(2)} & \bar{T}_2^{(3)} & \bar{T}_2^{(4)} & \bar{T}_2^{(5)} & \bar{T}_2^{(6)} \\ \bar{T}_3^{(1)} & \bar{T}_3^{(2)} & \bar{T}_3^{(3)} & \bar{T}_3^{(4)} & \bar{T}_3^{(5)} & \bar{T}_3^{(6)} \end{pmatrix} \begin{pmatrix} A_1 \\ A_2 \\ A_3 \\ A_4 \\ A_5 \\ A_6 \end{pmatrix}, \quad (3.14)$$

where superscript (α) , $\alpha = 1, \dots, 6$ represents 3 upgoing waves and 3 downgoing waves. $t_i^{(\alpha)}$, $i = 1, 2, 3$ represents the i^{th} component of polarization vector for α^{th} plane wave. $\bar{T}_i^{(\alpha)}$, $i = 1, 2, 3$ represents the i^{th} component of traction on the surface boundary between two layers caused by the α^{th} plane wave.

The particle displacement and traction on the surface boundary between two layers are continuous across the layer boundary. Using these boundary conditions, I can propagate a plane wave through many layers. I take a two-layer model as an example (Figure 3.1):

$$\mathbf{A}_{upper}^{(2)} = \mathbf{D}^{(2)}\mathbf{S}^{(1)}\mathbf{K}^{(1)}\mathbf{A}_{upper}^{(1)} = \mathbf{P}\mathbf{A}_{upper}^{(1)}, \quad (3.15)$$

where $\mathbf{K}^{(i)}$ represents the phase shift in the i^{th} layer. $\mathbf{D}^{(i)} = (\mathbf{S}^{(i)})^{-1}$ in the i^{th} layer (Aki and Richards 2002). \mathbf{P} is the propagator matrix.

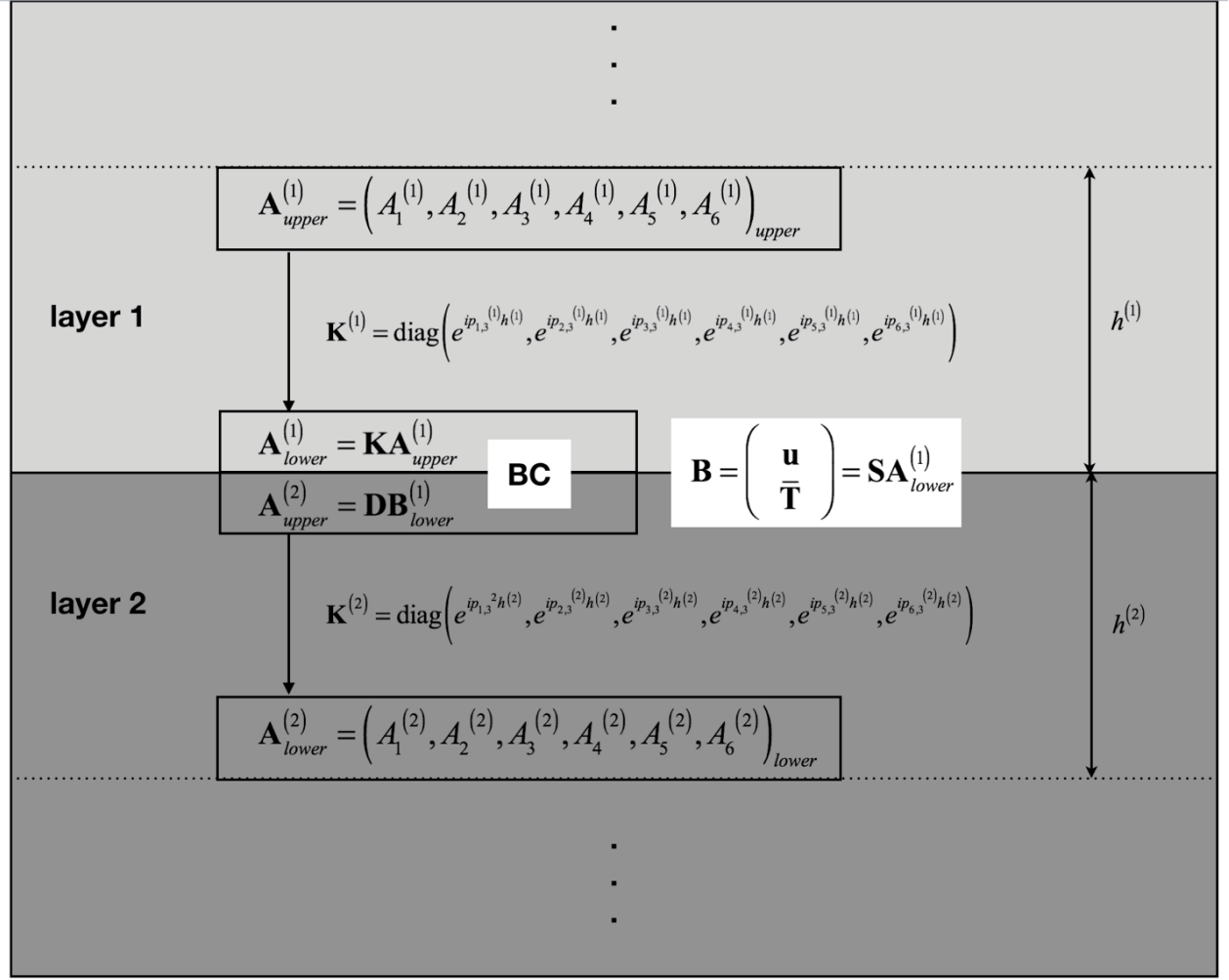


Figure 3.1. Propagator matrix in a two-layered model.

Suppose the amplitudes of downgoing waves in the 1st layer are known and the amplitudes of upgoing waves in the 2nd layer are desired. As the upgoing wave amplitudes are zero if the 2nd layer extends to infinity, the problem can be solved by blocking the propagator matrix \mathbf{P} into the following form:

$$\begin{pmatrix} \mathbf{0} \\ \mathbf{A}_d^{(2)} \end{pmatrix} = \begin{pmatrix} \mathbf{P}_{11} & \mathbf{P}_{12} \\ \mathbf{P}_{21} & \mathbf{P}_{22} \end{pmatrix} \begin{pmatrix} \mathbf{A}_u^{(1)} \\ \mathbf{A}_d^{(1)} \end{pmatrix}, \quad (3.16)$$

where $\mathbf{A}_d^{(2)} = (A_4^{(2)}, A_5^{(2)}, A_6^{(2)})_{upper}$, $\mathbf{A}_d^{(1)} = (A_4^{(1)}, A_5^{(1)}, A_6^{(1)})_{upper}$, and $\mathbf{A}_u^{(1)} = (A_1^{(1)}, A_2^{(1)}, A_3^{(1)})_{upper}$.

Thus $\mathbf{A}_d^{(2)}$ and $\mathbf{A}_u^{(1)}$ are:

$$\mathbf{A}_u^{(1)} = -\mathbf{P}_{11}^{-1}(\mathbf{P}_{12}\mathbf{A}_d^{(1)}), \quad (3.17)$$

and:

$$\mathbf{A}_d^{(2)} = \mathbf{P}_{21}\mathbf{A}_u^{(1)} + \mathbf{P}_{22}\mathbf{A}_d^{(1)} \quad (3.18)$$

The plane wave could thus be propagated layer by layer using equation (3.15). The Green-Christoffel equation and propagator matrix provide a solution for a single frequency. By multiplying with the frequency spectrum of a wavelet and summing, we can simulate the result for a plane wave with a specific time function.

3.3 Numerical results

To calculate the SWS pattern, I need to calculate 1) polarization of fast S wave (orientation of blue bar in Figure 3.3), and 2) traveltime difference between fast and slow S waves (length of blue bar in Figure 3.3). I solved for the Green-Christoffel equation and used the simple propagator matrix approach in the frequency-space domain (full-wave modeling) (e.g., Haskell, 1953; Mallick and Frazer, 1991) to compute SWS that would be observed at the station on the Earth's surface for a layered medium.

As an example, I simulated elastic wave propagation (plane wave incidence) in a 3-layered medium with the middle 20km-thick layer being the tilted transversely isotropic (TTI) portion

(not the entire slab) of the slab (Figure 3.2). I computed 3-component (3-C) synthetic seismograms for SV plane waves with different incident directions (incident angle i and incidence azimuth ϕ , the incident SV wave oscillates in the vertical plane). The source time function is a Ricker wavelet with a central frequency of 10 seconds. For each incident SV plane wave, I measured the shear-wave splitting and the fast-S polarization at the station. The results are shown in the lower hemisphere stereographic projection of the fast-S polarization vector (Figure 3.3). The length of this polarization vector represents the splitting time between the fast-S wave and the slow S-wave. It can be seen that depending on the incoming wave direction, the fast-S polarization can be either trench parallel or trench perpendicular and the splitting time can be more than 1.0 s. This phenomenon has been previously investigated by Song and Kawakatsu (2012) to study sub-slab anisotropy whereas the goal here is to study intra-slab anisotropy.

The numerical results imply that when the intra-slab anisotropy strength is large and cannot be overlooked, the S wave splitting can be significant even for a short propagation path in the slab.

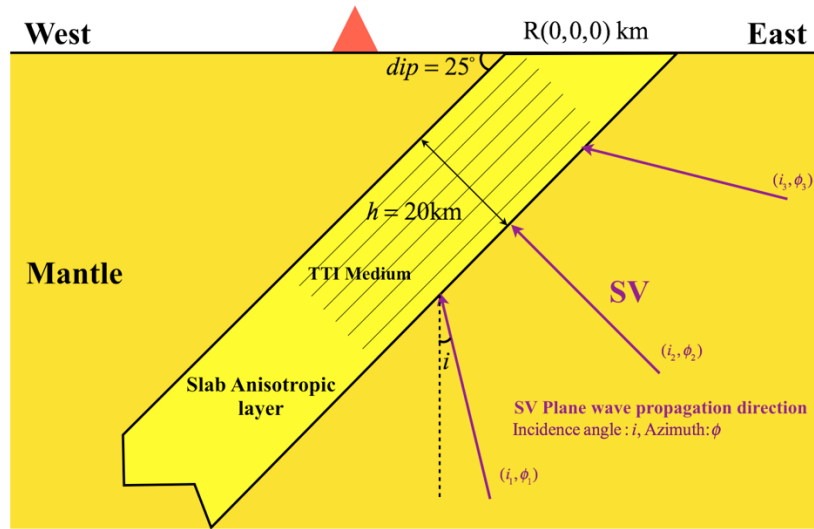


Figure 3.2 3D modeling of SWS for plane wave propagation through a dipping anisotropic layer. A vertical cross-section showing the anisotropic layer (part of the slab) and incident wave geometry. The slab is dipping to the west. The station (triangle) is 28km west of the trench. The middle layer is 20 km thick and has a tilted transverse isotropy (TTI) anisotropy (with symmetry axis normal to the slab) with the P-wave anisotropy $\epsilon = 0.3$, the SH-wave anisotropy $\gamma = 0.3$, and the Thomsen $\delta = 0$ (see (1.15) for definition). Along the TTI symmetry axis, its P-wave velocity, V_P is 8.4 km/s and S-wave velocity, V_S is 4.67 km/s. The SV-wave anisotropy σ is about 0.54 calculated using equation (1.16). The upper and lower layers are isotropic and have $V_P=8$ km/s and $V_S=4.45$ km/s. Rock density is set to be uniform (3400kg/m^3) in the whole model.

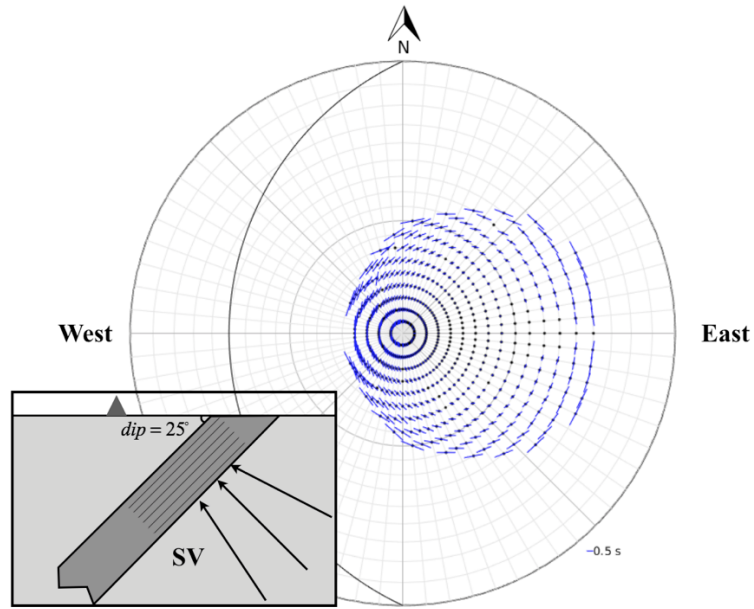


Figure 3.3 Lower hemisphere stereographic projection of the upgoing incident SV wave directions (i.e., locations of the blue bars) at the station. The orientation of the blue bar represents the projection of fast wave polarization on the ground. The length of blue bars (see the 0.5s scale at the lower right location) represents the travelt ime difference between the fast and slow shear waves. The graph inside the black box shows the schematic diagram of the geometry of the slab and incident plane wave with different propagation directions. I did not compute all possible incident angles but only those corresponding to the blue bars.

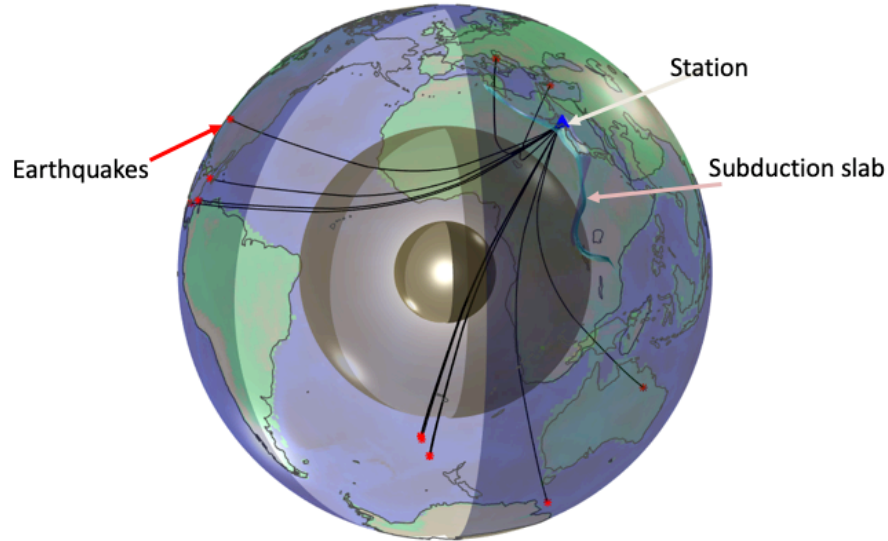


Figure 3.4 Seismic rays (SKS) through the Earth from different earthquakes to one seismic station in Japan.

3.4 Conclusions

Recent comprehensive analysis of non-double-couple components in the moment tensors for global deep earthquakes showed that SH-wave anisotropy (γ) in slabs can be strong ($\sim 25\%$ typically) (Li *et al.*, 2018) and SV-wave anisotropy σ ($\sim 60\%$ typically) can be estimated from the combination of ε and δ (see Chapter 1.6.2). In our numerical example, I assumed the value of ε , γ , and δ such that the S-wave anisotropy reasonably matched the results from the analysis of moment tensors. I solved Green-Christoffel equation and used propagator matrix method to calculate the SWS pattern for incident SV-wave with different backazimuths. The numerical results show that the existence of intra slab strong anisotropic structure could generate complex fast S-polarization patterns depending on the backazimuth of earthquakes and cause significant splitting time between fast and slow S-waves. This has significant implications:

- (i) SWS (both delay time and the fast S polarization direction) depends on earthquake source backazimuth. We must consider the incident direction of the incoming S waves.
- (ii) The observed shear-wave splitting phenomena may be caused by strong intra slab anisotropic structure besides the anisotropic structure in the mantle.
- (iii) We will make forward predictions for SWS for a transmitted shear wave through the slab to independently verify the existence of the inferred anisotropy structure.

It will be beneficial to study the relationship between the observed SWS pattern and the backazimuths of incident S waves in the SWS analysis (Figure 3.4) in the future.

4 Generation of a stochastic binary field that fits a given heterogeneity power spectrum

4.1 Summary

Incomplete binary mixing of two components can form a heterogeneous assemblage in space. The heterogeneity power spectrum of the assemblage can be frequently obtained in observation. However, it is unknown if one can find a stochastic binary field to generate the observed spectrum. I proposed a novel and powerful constructive procedure for this purpose (Li and Zheng, 2019). The procedure allows us not only to test whether certain binary mixing is feasible but also to tightly constrain the properties of the mixing components and the modal proportion. The method should find wide applications in many branches of geosciences.

4.2 Introduction

Mixing is a general phenomenon widely observed in many dynamic systems. Rather than being too general and vague in the description, we set our discussion in the context of solid Earth sciences. In the Earth's interior, mixing is a process to either generate or destroy geochemical and geophysical heterogeneities (Allegre and Turcotte, 1986; Kellogg and Turcotte, 1987; Hart, 1988; Kellogg and Turcotte, 1990; Hunt and Kellogg, 2001; van Keken *et al.*, 2002; Bercovici, 2007; Stixrude and Lithgow-Bertelloni, 2012). Therefore, mapping heterogeneities to infer mixing patterns can provide valuable information in understanding the dynamic evolution of Earth's interior.

Among all mixing scenarios, binary mixing (Farley *et al.*, 1992; Xu *et al.*, 2008; Shimizu *et al.*, 2016) has the fewest mixing components but occupies a special role. For example, the marble-cake model (Allegre and Turcotte, 1986) or the mechanical mixing model of basalt and harzburgite (Xu *et al.*, 2008) provides important frameworks to understand mantle evolution. Small-scale heterogeneities observed from seismic scattering in the lowermost mantle have been interpreted as mantle binary mixing with subducted mid-ocean-ridge basalt (Haugland *et al.*, 2018).

It is important to distinguish two important cases: complete and incomplete binary mixing. Let us consider a particular case where we want to mechanically mix two endmember rock types with different seismic velocities. We can analyze the assemblage by considering the content in boxes at different spatial locations and of different scales. The complete mixing results in a statistically homogenized assemblage where the relative modal proportion of each component is constant in any box regardless of its location and scale. In this case, the assemblage is considered as an effective homogeneous medium, and seismic waves will not ‘see’ heterogeneities. On the other hand, the incomplete mixing results in a binary velocity field where the modal proportion of each mixing component in the box depends on the box’s location and scale. In this case, the mixed assemblage could be heterogeneous at multiple scales, seen by seismic waves. Statistically, the property of a heterogeneous assemblage can be characterized by the first moment of the distribution (which is a mean value) and the second moment (which is the correlation function) Seismic tomography is such an example and can give the large-scale mean seismic velocity in the mantle (Romanowicz, 2003). However, knowing only the large-scale mean velocity is limited in understanding binary mixing because there are different possible small-scale mixing scenarios that can yield the same mean value. If

the correlation function of the velocity field fluctuation can also be obtained, the mixing can be much better understood. In this regard, seismic scattering can frequently determine the power spectrum (hence spatial correlation function) of the random heterogeneity using transmission fluctuations (Chernov, 1960; Aki, 1973; Wu and Flatté, 1990; Chen and Aki, 1991; Cormier, 2000; Zheng and Wu, 2005; Zheng and Wu, 2008; Sanborn *et al.*, 2017) or seismic envelopes (Sato and Fehler, 1998). The heterogeneity power spectrum is defined as the square of the Fourier amplitude spectrum and therefore does not have the phase information.

It is usually straightforward to find a random realization of a continuous (not binary) field (Muller *et al.*, 1992; Zheng and Wu, 2008) or a discrete field satisfying some specific correlation function form such as von Karman distribution (Goff *et al.*, 1994; Levander *et al.*, 1994) that can generate the observed heterogeneity power spectrum. However, the question posed here is: can we find a stochastic discrete binary velocity field for a general correlation function such that it can produce the observed heterogeneity power spectrum?

4.3 Methods

4.3.1 Definition of heterogeneity power spectrum and two-point correlation function

Suppose the heterogenous seismic velocity field in the mantle is $v(\mathbf{x})$. The background velocity is v_0 . Then the fluctuation of the velocity field (Zheng and Wu, 2008) could be defined as:

$$\varepsilon(\mathbf{x}) = \frac{1}{2} \left[\frac{v_0^2}{v^2(\mathbf{x})} - 1 \right] \approx \frac{v(\mathbf{x})}{v_0} - 1 = \frac{\delta v(\mathbf{x})}{v_0}. \quad (4.1)$$

The two-point correlation function, $B(\mathbf{r})$, of the fluctuation field is defined as

$$B(\mathbf{r}) = \overline{\varepsilon(\mathbf{x})\varepsilon(\mathbf{x} + \mathbf{r})}, \quad (4.2)$$

where the overbar means averaging the product over all possible locations \mathbf{x} for a given a correlation lag \mathbf{r} . The heterogeneity spectrum of the fluctuation field is defined as

$$F(\mathbf{k}) = \iiint \varepsilon(\mathbf{x}) e^{-i\mathbf{k}\cdot\mathbf{x}} d^3\mathbf{x}, \quad (4.3)$$

which is usually a complex number. The heterogeneity power spectrum $P(\mathbf{k})$ is just the Fourier transform of the fluctuation correlation $B(\mathbf{r})$:

$$P(\mathbf{k}) = \iiint B(\mathbf{r}) e^{-i\mathbf{k}\cdot\mathbf{r}} d^3\mathbf{r} = |F(\mathbf{k})|^2. \quad (4.4)$$

Therefore, knowing the correlation function B can enable us to obtain the power spectrum P , and vice versa.

I further assume the binary mixture is a statistically isotropic random medium, which means that the heterogeneity correlation function does not depend on the orientation and we have $B(\mathbf{r}) = B(r)$, where r is the length of the vector \mathbf{r} .

It is easy to see that the two-point correlation function of the velocity field $C(r) = C(\mathbf{r}) = \overline{v(\mathbf{x})v(\mathbf{x} + \mathbf{r})}$ has the following relationship with the fluctuation correlation function of the random field $B(r)$ using equation (4.1):

$$C(r) = v_0^2 [1 + B(r)]. \quad (4.5)$$

4.3.2 Problem statement and binary field construction

Our goal is to construct a stochastic binary velocity field $V^{(B)}(\mathbf{x})$, whose spatial correlation function is the same as $C(r)$.

To achieve this goal, I applied a two-step reconstruction method.

- (i) In the first step, I will determine a viable combination of the two endmember velocities and the volume fraction of each component.
- (ii) In the second step, I will apply the simulated annealing (SA) optimization method (Yeong and Torquato, 1998) to find a stochastic realization of a binary field that could yield the correlation function $C(r)$.

4.3.3 Step1: Determination of velocities and volume fractions of the mixing endmembers

Suppose the two mixing components have two discrete velocities: v_a and v_b for phase- a and phase- b , respectively. The binary velocity field $V^{(B)}$ takes a velocity (either v_a or v_b) at any location \mathbf{x} and is sought to fit the following constraint

$$C(r) = \overline{V^{(B)}(\mathbf{x})V^{(B)}(\mathbf{x} + \mathbf{r})} . \quad (4.6)$$

It is more convenient for us to use an indicator function defined as:

$$I^{(a)}(\mathbf{x}) = \begin{cases} 1 & \text{if } \mathbf{x} \in \text{phase a,} \\ 0 & \text{if } \mathbf{x} \notin \text{phase a.} \end{cases} \quad (4.7)$$

The correlation function of the indicator field for phase- a is defined as:

$$S^{(a)}(r) = S^{(a)}(\mathbf{r}) = \overline{I^{(a)}(\mathbf{x})I^{(a)}(\mathbf{x} + \mathbf{r})} . \quad (4.8)$$

Because the relationship between the indicator field and binary velocity field is:

$$I^{(a)}(\mathbf{x}) = \frac{V^{(B)}(\mathbf{x}) - v_b}{v_a - v_b} , \quad (4.9)$$

we have the following:

$$\overline{I^{(a)}(\mathbf{x})I^{(a)}(\mathbf{x}+\mathbf{r})} = \frac{1}{(v_a - v_b)^2} \left\{ \overline{V^{(B)}(\mathbf{x})V^{(B)}(\mathbf{x}+\mathbf{r})} - v_b \left[\overline{V^{(B)}(\mathbf{x})} + \overline{V^{(B)}(\mathbf{x}+\mathbf{r})} \right] + v_b^2 \right\}, \quad (4.10)$$

Since $\overline{V^{(B)}(\mathbf{x})} = (\phi_a v_a + \phi_b v_b)$, it is straightforward to show the following relationship between $C(r)$ and $S^{(a)}(r)$:

$$C(r) = a_1 S^{(a)}(r) + a_2 \phi_a + a_3, \quad (4.11)$$

where

$$a_1 = (v_a - v_b)^2, \quad a_2 = 2v_b(v_a - v_b), \quad a_3 = v_b^2. \quad (4.12)$$

The bulk volume fraction of phase- a , is given by the correlation function $I^{(a)}(\mathbf{x})$ at the zero lag:

$$S^{(a)}(0) = \phi_a. \quad (4.13)$$

On the other hand, when the lag R is large enough, we have

$$S^{(a)}(R) = \phi_a^2. \quad (4.14)$$

To see the validity of equation (4.14), I used the following rationale. At any point in the binary field, the probability to find phase- a is ϕ_a . The probability of finding phase- a simultaneously at two locations (see equation (4.8)) at a distance R apart is ϕ_a^2 when R is large. The reason we need a large R is that the field is decorrelated at large distances.

Plugging (4.5), (4.13), and (4.14) into equation (4.11), we can obtain the relationship v_a , v_b , and ϕ_a :

$$\begin{aligned}
v_a(\phi_a) &= v_0 \left[\sqrt{1+B(R)} + \sqrt{\frac{1-\phi_a}{\phi_a}} \sqrt{B(0)-B(R)} \right], \\
v_b(\phi_a) &= v_0 \left[\sqrt{1+B(R)} - \sqrt{\frac{\phi_a}{1-\phi_a}} \sqrt{B(0)-B(R)} \right].
\end{aligned} \tag{4.15}$$

Here, $B(0)$ and $B(R)$ can be taken as known from the correlation function $B(r)$ (which is inverted from the observations) and v_0 is the background velocity. Given a volume fraction of phase- a , ϕ_a , we can determine the two endmember velocities v_a and v_b using equation (4.15). We still need to show that there is a stochastic binary field whose correlation function can fit the observed correlation function.

In practice, this correlation function could be obtained from observations such as seismic transmission fluctuations (Cormier *et al.*, 2018) or seismic reflection data (Scholer *et al.*, 2010). For observations using seismic transmission fluctuations, the correlation function $B(r)$ is the inverse Fourier transform of the spatial power spectrum of the velocity heterogeneity, which is related to the observed logarithmic amplitude and phase fluctuation coherence functions across a seismic array (Zheng and Wu, 2008; Cormier *et al.*, 2018). For reflection data, the correlation function can be estimated from the migration image. Note that the information in the correlation function obtained from seismic observations reflects heterogeneous features on the scale of the seismic wavelength.

4.3.4 Step2: Determination of the stochastic structure of binary-mixing field

Because there is a one-to-one correspondence between the fluctuation correlation $B(r)$ and the indicator correlation function $S^{(a)}(r)$ using equation (4.11), I chose to find a binary field with a correlation that fits $S^{(a)}(r)$.

I will apply an iterative simulated annealing (SA) method (Kirkpatrick *et al.*, 1983; Yeong and Torquato, 1998) for this purpose. I start from some random binary indicator field. I then update the binary indicator field in order to reach the final stochastic field with $S^{(a)}(r)$. In each SA step, I proposed to minimize the misfit E defined in the least-squares sense:

$$E = \sum_i \left[S^{SA}(r_i) - S^{(a)}(r_i) \right]^2, \quad (4.16)$$

where r_i denotes the i^{th} correlation lag, and S^{SA} is the correlation function for the binary indicator field at that SA step. For each lag r_i , I calculate the average of all corresponding two-point products (Yeong and Torquato, 1998).

In each SA step, I swap two points randomly chosen from the indicator field. In this way, the bulk volume fraction of each phase will be automatically conserved. I then calculate the new misfit E' and I can compute the change in the misfit $dE = E' - E$ before and after each swap. If $dE \leq 0$, I will accept the swap with probability 1. If $dE > 0$, the swap is accepted according to the probability, $p(dE)$, defined as

$$p(dE) = \begin{cases} 1 & dE \leq 0 \\ \exp(-dE / T) & dE > 0 \end{cases}. \quad (4.17)$$

The reason I may still accept the swap even the misfit increases is to avoid being trapped in the local minimum in iteration.

The starting value of T (usually called “melting temperature” in SA) should be a value large enough to make the acceptance ratio in the initial several hundred swaps greater than 80%. If the acceptance ratio is less than 80%, the initial T should be doubled. After the initial “melting temperature” T is determined, the “cooling process” starts, the parameter T decreases

at a constant rate, say 0.95, after certain number of swaps (Kirkpatrick, 1984). The iteration terminates when the misfit E given by equation (4.16) is less than some given tolerance value such that the misfit is minimized in the sense of the least-squares.

4.4 Examples

I provided two examples to show how to construct a stochastic binary field whose correlation/spectrum can fit a given correlation/spectrum function. I will test two types of 2D correlation functions for the fluctuations, Gaussian and von Karman types. For the Gaussian type, its correlation function is:

$$B(r) = \chi^2 e^{-(r/r_0)^2} . \quad (4.18)$$

For the von Karman type, its correlation function is:

$$B(r) = \frac{2^{1-\nu}}{\Gamma(\nu)} \chi^2 \left(\frac{r}{r_0} \right)^\nu K_\nu \left(\frac{r}{r_0} \right) . \quad (4.19)$$

In equations (4.18) and (4.19), χ is the root mean square (rms) of the random fluctuation field. r is the correlation lag. r_0 is a length scale for the heterogeneities. In equation (4.19), Γ is the gamma function, K_ν is the modified Bessel function, ν is the Hurst number ($0 < \nu < 1$) that controls the amount of small-scale heterogeneities relative to the large-scale ones.

In our examples, the way I constructed the continuous random field for a given correlation function is as follows. I Fourier transformed the correlation function to get the Fourier amplitude spectrum. This amplitude spectrum is multiplied with a random phase in the wavenumber domain, and then transformed back to the space domain, keeping the real part (the

imaginary part is zero). Although it is intuitive to simply pixelating the continuous field into binary field using a certain threshold, the pixelated binary field would not fit the correlation function. That is why I took advantage of the simulated annealing method to reconstruct the binary field.

4.4.1 Gaussian Type:

For the Gaussian type, I set the rms velocity $\chi = 0.03 \text{ km/s}$, $r_0 = 0.2 \text{ km}$ to obtain the correlation function $B(r)$ (Fig. 1a). Suppose the corresponding fluctuation field has a dimension of 200×200 pixels, and the pixel size is the same along the x direction (Δx) and the z direction (Δz), i.e., $\Delta x = \Delta z = 0.05 \text{ km}$. Given a background velocity v_0 (say, $v_0 = 8 \text{ km/s}$), a random realization of the velocity field is $v(x, z)$ (Figure 4.2e) if we were to find a continuous random field that can fit the correlation function $B(r)$. However, our goal is to find a stochastic binary field that generate the same $B(r)$.

With $B(0)$, $B(R)$, and v_0 , the relationship of the binary velocities v_a (red dashed line) and v_b (blue dash-dotted line) with respect of the volume fraction, ϕ_a , can be determined (Figure 4.1b) (equation (4.15)). For instance, by fixing $\phi_a = 0.3$, we can determine the velocities of the two mixing endmembers, $v_a = 8.36 \text{ km/s}$ and $v_b = 7.83 \text{ km/s}$, respectively. If these velocities do not correspond to properties of real geological components, we can continue to vary ϕ_a until the two velocities make geological sense. Therefore, this is a powerful method to constrain possible v_a , v_b , and ϕ_a if the binary mixing scenario is assumed.

Next, we I will find a random binary field that corresponds to $B(r)$. To do this, I chose to work on the binary indicator correlation function $S^{(a)}(r)$ which has a one-to-one correspondence with $B(r)$ (Figure 4.1a) (also see equations (4.5) and (4.11)).

I created an initial random binary field model with the volume fraction of phase-a $\phi_a = 0.3$ (Figure 4.2c). The correlation function of the corresponding indicator field is far from the observed $S^{(a)}(r)$ (Fig. 2a). Then I applied the SA iteration. At each SA step, I computed the correlation function $S^{SA}(r)$ and its misfit (Fig. 2b). After 2 million SA steps, A correlation $S^{SA}(r)$ that fits the true correlation function $S^{(a)}(r)$ well is achieved (Figure 4.2a) and the misfit is decreased to an acceptable level (Figure 4.2b).

The final stochastic binary field (Figure 4.2d) from the SA method shows many spatially contiguous domains or “blobs”. These blobs have similar spatial scales which is characteristic to the single-scale Gaussian random field.

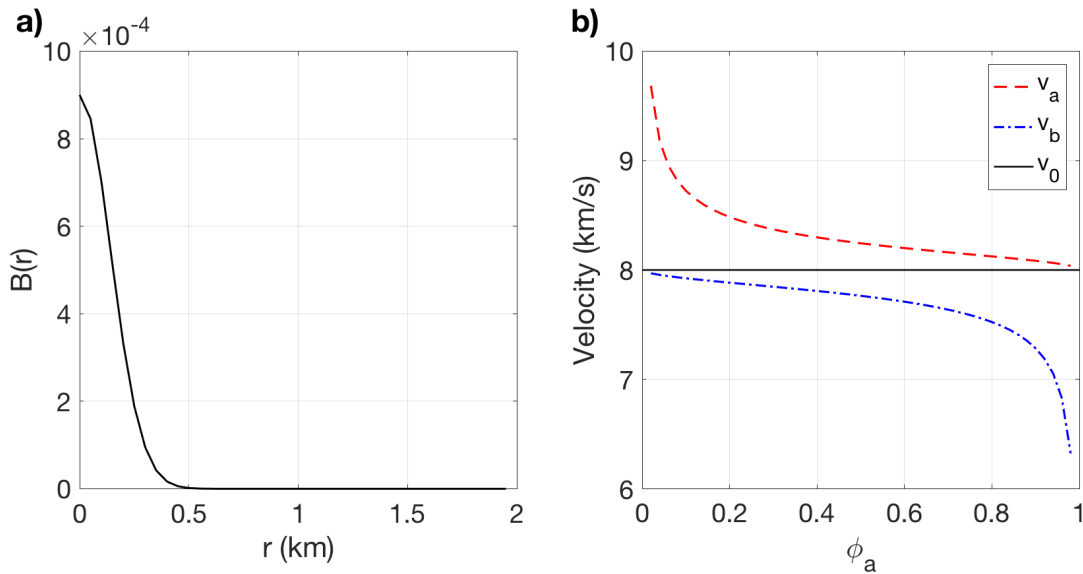


Figure 4.1. (a) A Gaussian correlation function. (b) Relationship of binary velocities v_a (red dashed line) and v_b (blue dash-dotted line) with the volume fraction of phase-a ϕ_a for this Gaussian type. The black solid line represents the background velocity v_0 .

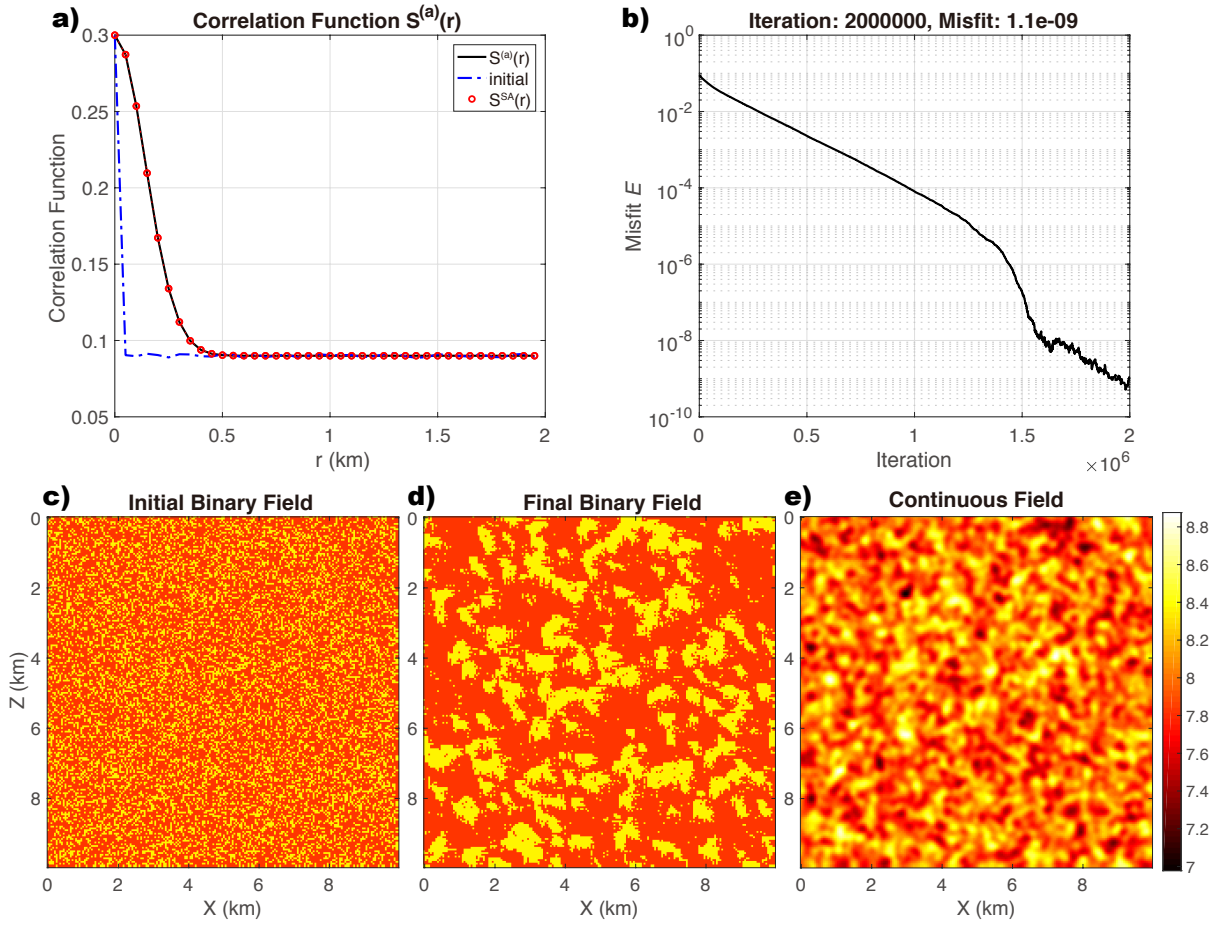


Figure 4.2. Gaussian type binary field. (a) Comparison of the observed correlation function ($S^{(a)}$, black solid line), initial correlation function (blue dash-dotted line), and final correlation function of the indicator field after 2 million simulated annealing iterations (S^{SA} , red circles); (b) Correlation misfit, E (equation (4.16)), with the iteration number; (c) Initial random binary velocity with volume fraction $\phi_a = 0.3$ for phase-a. (d) Final binary velocity field $V^{(B)}(x, z)$

using SA. (e) One realization of the continuous velocity field given the observed $B(r)$ and background velocity v_0 . In (c) and (d), the yellow region denotes phase-a and red region denotes phase-b.

4.4.2 von Karman Type:

I set the rms velocity $\chi = 0.03 \text{ km/s}$, $r_0 = 0.4 \text{ km}$, and $\nu = 0.2$ to obtain one von Karman type correlation function $B(r)$ (Figure 4.3a). Suppose the corresponding fluctuation field has a dimension 400×400 pixels, each pixel is a grid with dimension $0.05 \text{ km} \times 0.05 \text{ km}$. We can then obtain one random realization of the continuous velocity field (Figure 4.4e) given background velocity $v_0 = 8 \text{ km/s}$.

Similar to the Gaussian type, we can determine the relationship of the binary velocities v_a (red dashed line) and v_b (blue dash-dotted line) with volume fraction ϕ_a (Figure 4.3b).

Given a volume fraction $\phi_a = 0.3$, I obtained $v_a = 8.33 \text{ km/s}$ and $v_b = 7.87 \text{ km/s}$ using equation (4.15). The structure of the binary field could be obtained in a way similar to the one for the Gaussian type after 3 million iterations. The $S^{SA}(r)$ that fits the observed correlation function $S^{(a)}(r)$ well and the misfit was reduced to the level of 10^{-10} (Figure 4.4b). The final SA binary velocity field (Figure 4.4d) shows that the spatial distribution of phase-a is less contiguous compared to the Gaussian case (Figure 4.2d). There are multiple sizes for the contiguous domains dispersed throughout the model, which are characteristic for the multi-scale von Karman random medium.

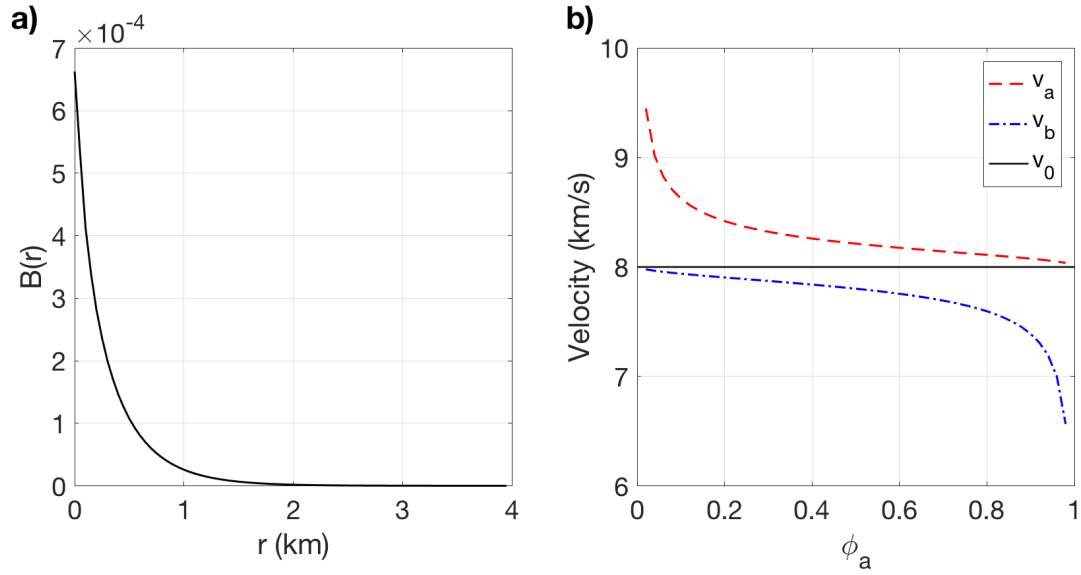


Figure 4.3. **(a)** von Karman correlation function. **(b)** Relationship of binary velocities v_a (red dashed line) and v_b (blue dash-dotted line) with the volume fraction of phase-a ϕ_a for the von Karman type medium. The black solid line represents the background velocity v_0 .

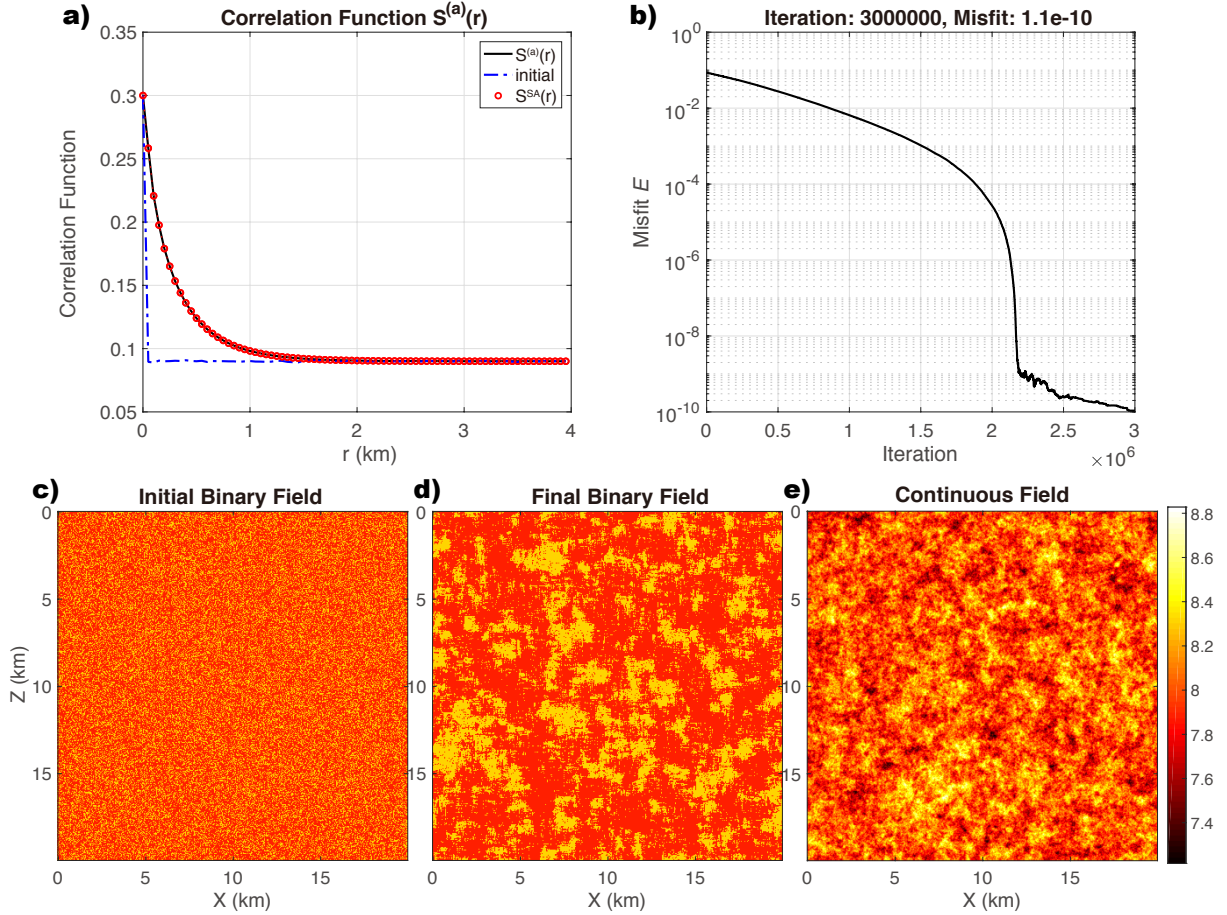


Figure 4.4. von Karman binary field. **(a)** Comparison of the observed correlation function (black solid line), initial correlation function (blue dash-dotted line), and final SA correlation function (red circles) of binary indicator field after 3 million iterations. **(b)** Misfit E (equation (4.16)) with the iteration number. **(c)** Initial random binary velocity field with volume fraction $\phi_a = 0.3$. **(d)** Final binary-mixing velocity field $V^{(B)}(x,z)$ after 3 million steps of SA. **(e)** One random realization of continuous velocity field given observed $B(r)$ and background velocity v_0 . In **(c)** and **(d)**, the yellow region denotes phase-a and red region denotes phase-b.

4.5 Discussion and Conclusions

Our iterative simulated annealing approach provides a new way to test the feasibility of geological binary-mixing models such as binary models for the mantle (Farley *et al.*, 1992; Xu *et al.*, 2008; Shimizu *et al.*, 2016). If some region in the mantle is composed of two types of rocks such as basalt and harzburgite, we can then constrain the velocities and volume fraction of basalt and harzburgite using the observed heterogeneity spectrum. This can be potentially useful in understanding mantle evolution and recycling of slab materials.

I note that based only on the measured power spectrum, we cannot tell if the true field is composed of two or more mixture components because the power spectrum only gives us one aspect (spatial correlation structure) of the true assemblage property. In the scope of the paper, I take ‘binary mixing’ scenario as a constraint to interpret the spectrum in this context. If the medium is indeed composed of more than two components, our inversion may give incorrect results.

This method also has the potential to be implemented to 3D case with acceptable computation cost. For the 2D case in the Von Karman type example, the inversion only takes 381 seconds for 3 million iterations given the power spectrum on MATLAB R2017b. The SA sampling step’s time complexity is $O(n)$ (n is the sampling dimension). Although we may need more iterations to achieve convergence, the computational cost would be acceptable.

In conclusion, I find a novel constructive approach using simulated annealing to construct a random binary field that fits both the mean value and the correlation function (or heterogeneity power spectrum) of random heterogeneities. This new method enables us to obtain a tight

relationship of the binary velocities and the volume fraction of the binary endmembers. Spatial patterns of the random field can be used to infer dynamic styles of mixing. The method is general and is a new powerful analysis tool for understanding binary mixing in a variety of settings.

5 Physics-Guided Machine Learning Identification of Discrete Fractures From Double Beam Images

5.1 Summary

Reservoir natural fracture detection is of critical importance in unconventional resource and geothermal resource development and production. Previously, a double-beam interference method was proposed to characterize irregularly distributed fractures, including multiple coexisting fractures with random spacings and varying azimuths (Zheng *et al.*, 2013; Hu and Zheng, 2017; Hu *et al.*, 2018). This method is target-oriented, and it outputs complex-valued interference patterns for reservoir fracture target, which contain information about local fracture orientation, density, and fracture compliance. In the double-beam method, only amplitude information of the double-beam image was interpreted, and the phase spectrum was ignored. In this study, I take advantage of machine learning technique to perform high-resolution interpretation of the double-beam images to directly obtain discrete fractures (Li *et al.*, 2019). The machine learning algorithm is essentially a constrained Fourier analysis on complex-valued 2D images

5.2 Introduction

Fractures are common and important geological elements in many different geological settings. The porosity and compliance of subsurface fractures in the reservoir can influence fluid flow significantly (Nelson, 2001). A prior knowledge about the fracture geometries such as fracture orientation and spacing can greatly improve our ability to capture flow transport behavior (Kang *et al.*, 2011; Nick *et al.*, 2011; Kang *et al.*, 2016). On the other hand, knowledge about the

distribution of subsurface fractures can place constraints on the stress state of the reservoir fields, which is critical to guide the well drilling and hydraulic fracturing in order to enhance and stimulate the production of hydrocarbon or geothermal resources (Hubbert and Willis, 1957; Olson, 1989; Barton *et al.*, 1995; Nelson, 2001; Montgomery and Smith, 2010).

Many different active source seismic exploration methods have been used to probe or image the subsurface fractures. Traditionally, subsurface fractures can be characterized based on anisotropic seismic wave propagation using methods such as Amplitude-Versus-Offset (Vavrycuk *et al.*) or Amplitude-Versus-Azimuth (AVAz) (Thomsen, 1999; Vasconcelos and Grechka, 2007; Far *et al.*, 2014) and shear wave splitting (Crampin, 1985; Tatham *et al.*, 1992; Vetri *et al.*, 2003; Long, 2013; Verdon and Wustefeld, 2013). These methods are based on the effective anisotropic medium theory, which in its simplest form assumes a single set of aligned subsurface fractures with uniform spacing and size much smaller than the seismic wavelength (David *et al.*, 1990). However, in reality, reservoirs may contain multiple sets of fractures cutting with each other. The fractures could be distributed randomly with variable geometries and multiple length scales, some of which could be larger than the probing seismic wavelength (Gale *et al.*, 2007). Furthermore, if multiple randomly distributed fractures coexist in reality, AVAz analysis may be invalid due to strong multiply-scattered seismic waves (Fang *et al.*, 2017).

In addition, scattered waves related to fractures have been used to image fractures via stacking (Willis *et al.*, 2006; Fang *et al.*, 2013) and migration (Landa *et al.*, 2011; Schoepp *et al.*, 2015; Silvestrov *et al.*, 2016). However, these scattering-based imaging/migration methods can only provide discrete fracture scattering energy. An additional interpretation step is needed to obtain local fracture spacings and orientation.

Zheng et al. (2013) proposed a double-beam method by utilizing the interference pattern of multiply scattered waves among fractures. This method forms two beams to mutually illuminate the subsurface target, so-called as double-beam method (DB for short). This method has been validated to be able to detect the fracture orientations, spacings, and compliance for multiple coexisting sets of fractures with random spacings and compliance in a non-flat reservoir layer (Zheng *et al.*, 2013; Hu and Zheng, 2017; 2018; Hu *et al.*, 2018).

Previously, only amplitude information of the double-beam interference (DBI) pattern is interpreted (Zheng *et al.*, 2013), and the DB method outputs fracture parameters (e.g., orientation, density, compliance), not discrete fracture geometry. The exact locations of fractures are not inferred due to the ignorance of the phase information. In this study, I will incorporate both amplitude and phase information of a DBI image. I will train a fully-connected neural network based on a synthetic training dataset to learn to convert the complex-valued DBI pattern into a deterministic discrete fracture network (DFN) directly. Essentially, the neural network is trained to learn a constrained inverse Fourier transform. I will show the effectiveness of the trained neural network on a synthetic test dataset.

5.3 Methods

5.3.1 Review of fracture characterization using the DB method

The DB method characterizes subsurface fractures by focusing a source-beam and a receiver-beam from the surface to a target zone in a fractured reservoir (Zheng *et al.*, 2013). The essence of the DB method is based on multiple scattering of a local incident plane wave upon a set of fractures. The scattering wavenumber \mathbf{k}^r on the receiver side and the incident wavenumber \mathbf{k}^s on the source side are related by the local fracture network geometry around the target (Rayleigh, 1907; Aki and Larner, 1970; Ishimaru, 1991).

$$\mathbf{k}_T^r = \mathbf{k}_T^s + n \frac{2\pi}{a} \hat{\phi}, \quad n = 0, \pm 1, \pm 2, \dots, \quad (5.1)$$

where \mathbf{k}_T^r and \mathbf{k}_T^s are the horizontal components of \mathbf{k}^r and \mathbf{k}^s , respectively; $\hat{\phi}$ is the fracture normal direction defined as a unit vector perpendicular to the fracture plane and a is the local fracture spacing (Figure 5.1). We focus on the case of $n = -1$ because the first-order back-scattered wave has strong energy in numerical simulation (Zheng *et al.*, 2013).

We can form the source beam and the receiver beam in the frequency domain to form the local fracture DBI pattern (Zheng *et al.*, 2013):

$$\sigma(a, \hat{\phi} | \omega, \mathbf{r}) \sim \sum_s \sum_r b_s^*(\mathbf{x}_s | \mathbf{r}, \mathbf{p}^s, w_s, \omega) b_r^*(\mathbf{x}_r | \mathbf{r}, \mathbf{p}^r, w_r, \omega) D(\mathbf{x}_s, \mathbf{x}_r, \omega). \quad (5.2)$$

Here, $b_s(\mathbf{x}_s | \mathbf{r}, \mathbf{p}^s, w_s, \omega)$ is the source beam and $b_r(\mathbf{x}_r | \mathbf{r}, \mathbf{p}^r, w_r, \omega)$ is the receiver beam, with $\mathbf{p}^s = \frac{\mathbf{k}^s}{\omega}$ and $\mathbf{p}^r = \frac{\mathbf{k}^r}{\omega}$ represent slowness vectors of source beam and receiver beam and w_s and w_r represent source and receiver Gaussian beam width. The symbol ‘*’ means the complex conjugate. $D(\mathbf{x}_s, \mathbf{x}_r, \omega)$ is the data sourced from \mathbf{x}_s and recorded at \mathbf{x}_r in the frequency domain. σ is a frequency-space dependent complex-valued 2D image at a certain probing depth. The target

fracture set does not necessarily to be vertical and its height could be quite small. This method is probing the periodicity of the top edge of fractures in the horizontal direction (similar to grating diffraction). But if the fracture height is too small, the diffraction energy may be too weak to be detected. If the background medium is homogeneous with constant velocity V_0 , the Gaussian beam solution reads:

$$b(s, q_1, q_2 | w_0, \omega_r, \omega) = \sqrt{\frac{V_0^2}{\omega_r w_0^2 + iV_0 s}} \times \exp\left[i \frac{\omega}{V_0} s - \frac{1}{2} \omega (\omega_r w_0^2 + iV_0 s)^{-1} (q_1^2 + q_2^2) \right], \quad (5.3)$$

where (s, q_1, q_2) represents the length in ray centered coordinate system, w_0 specifies the initial beam width at some reference frequency ω_r (Hill, 1990; Červený, 2002), . In the ray centered coordinate system (Červený, 2002), s measures the arc length along the ray from the target fracture, and its unit base vector is the unit tangent column vector \mathbf{t} . q_1 and q_2 are the magnitudes along unit base column vectors \mathbf{e}_1 and \mathbf{e}_2 at s . The vectors \mathbf{e}_1 and \mathbf{e}_2 are introduced with the help of the normal column vector \mathbf{n} , binormal column vector \mathbf{b} , and torsion T of the ray at s :

$$\mathbf{e}_1 = \mathbf{n} \cos(\Theta) - \mathbf{b} \sin(\Theta), \quad \mathbf{e}_2 = \mathbf{n} \cos(\Theta) + \mathbf{b} \sin(\Theta).$$

with $\Theta = \int_0^s T(\xi) d\xi$. The integral is taken along the ray. Suppose $\mathbf{x}_m = (x_{m1}, x_{m2}, x_{m3})$ is a point on the ray and its length along the ray path from the target is s_m . The coordinate (s, q_1, q_2) in the ray-centered coordinates $(\mathbf{t}, \mathbf{e}_1, \mathbf{e}_2)$ is related to the coordinate $\mathbf{x} = (x_1, x_2, x_3)$ in the standard Cartesian coordinates by the transformation matrix $[\mathbf{t}, \mathbf{e}_1, \mathbf{e}_2]$:

$$(\mathbf{x} - \mathbf{x}_m) [\mathbf{t}, \mathbf{e}_1, \mathbf{e}_2] = (s - s_m, q_1, q_2). \quad (5.4)$$

For a target, we obtained the DBI by stacking the σ of all possible pairs of source and receiver beams.

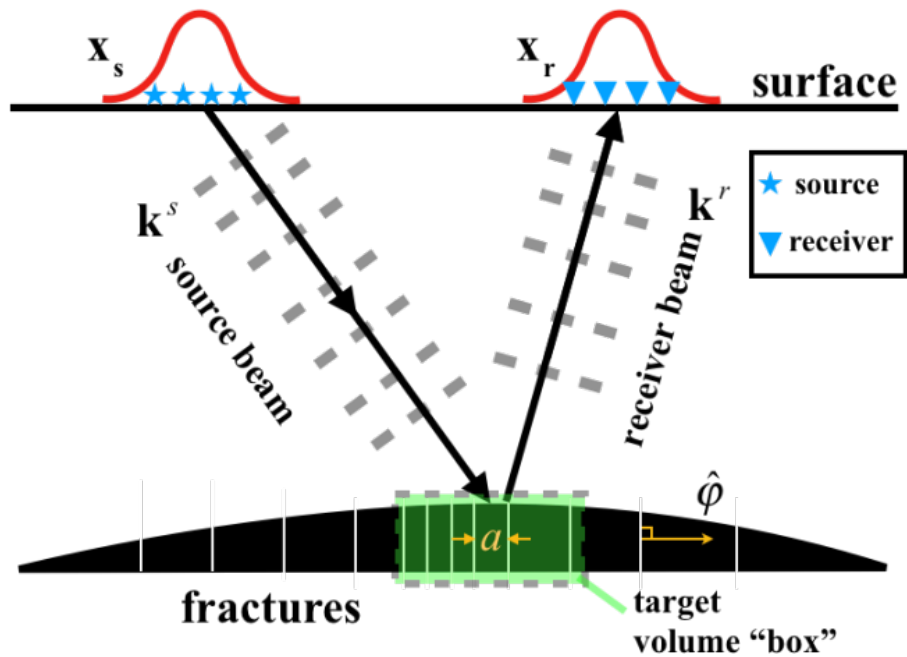


Figure 5.1. Schematic diagram of the DB imaging method. Stars and triangles represent source and receivers respectively. a is the local fracture spacing in the target area. $\hat{\phi}$ the fracture normal direction.

a) Map view of Fracture Distribution

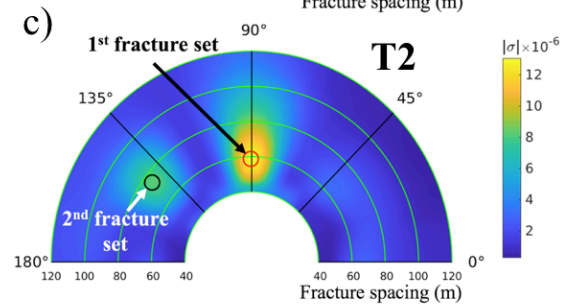
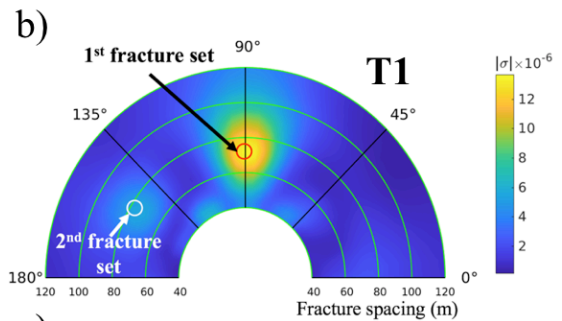
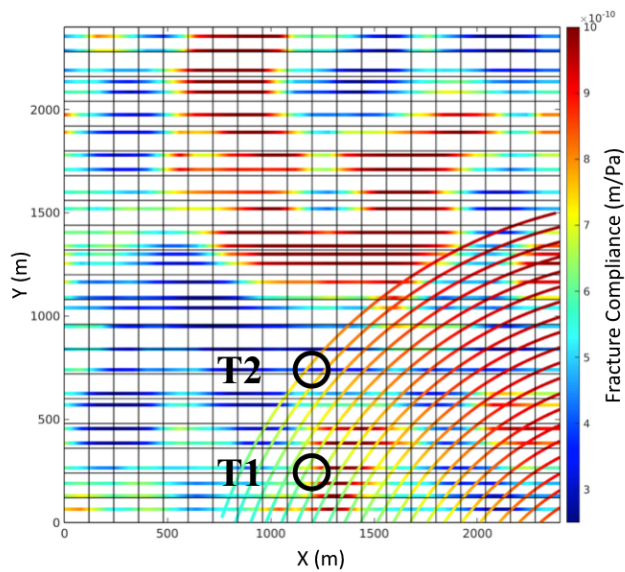


Figure 5.2. One example of the absolute value of the complex-valued DBI pattern (Hu *et al.*, 2018). (a) Map view of the fracture distribution. The horizontal and circled lines represent vertical fractures. Color represents fracture compliance. Two targets blocks T1 and T2 (each target contains two sets of fractures) are selected to generate DBI patterns in (b) and (c). The radial direction indicates the scanned fracture spacing a (i.e., 40-120 m), the tangential direction indicates scanned fracture orientation $\hat{\phi}$. If there exists a fracture set within the scanned fracture spacing and orientation range, there will be high-amplitude bright spots which represents the relative magnitude of compliance for this set of fracture. Two picked bright spots indicate two detected sets of fractures.

By interfering the source beam and receiver beam for all possible pairs of sources and receivers in the acquisition system and stacking the obtained interference patterns, we obtain a final complex-valued DBI pattern. This DBI pattern can be interpreted manually by taking the absolute value of it (Figure 5.2). The “bright spots” in the DB image indicate the most likely fracture spacing and orientations. Meanwhile, the magnitude of the bright spot indicates the fracture normal compliance.

In a perfect geometry (infinite acquisition plane, dense receivers, correct velocity models), our DB method simply implements a spatial Fourier transform from the fracture distribution to the DBI. However, in an imperfect world where the acquisition is limited in aperture, the Fourier transform is not a straightforward mathematical transform, however its core function is still similar to a Fourier transform. This physical meaning of DB method inspired us to take advantage of using neural networks to learn a constrained inverse Fourier transform algorithm, which could transform the DBI back to the DFN.

5.3.2 Translation of DBI into DFN using neural networks

Our goal is to train a neural network to convert the complex-valued DBI pattern to DFN automatically. We called it “double-beam neural network” (DBNN).

To achieve this goal, I created a labeled dataset with a volume of 10,000 samples. To create each sample in the dataset, I first generated one set or two sets of 2D fractures (lines) with random spacing and orientations and then did forward modeling to calculate DBI’s. In the forward modeling, I used Born modeling to efficiently generate waveforms corresponding to variable distributed fractures and then applied the DB method to obtain DBIs (Hu and Zheng, 2018). A DBI has 121 fracture azimuths/orientations and 34 fracture densities (e.g., spacings). Because a DBI contains both real and imaginary parts, the DBI image size is $121 \times 34 \times 2$. The DFN image size is 21×21 . Each pixel in the DFN image is either 0 or 1 with 1 denoting the existence of fracture and 0 no fracture. To train our DBNN I used DBI as input data and the corresponding DFN as the label. I split our dataset into two parts, 80% used for training and 20% used as the test set.

I applied a simple fully-connected NN with one hidden layer. The hidden layer has 1,000 neurons (Figure 5.3). The DBI and DFN images are flattened into 1-D vectors for training the neural network. Thus, the input DBI layer contains $121 \times 34 \times 2 = 8228$ neurons and the output DFN layer contains $21 \times 21 = 441$ neurons. I applied dropout (Srivastava *et al.*, 2014) to both the input and hidden layers with a dropout rate of 50% to avoid overfitting in the training dataset. I used the sigmoid function (5.5) as activation function for each layer.

$$\sigma(z) = \frac{1}{1 + e^{-z}} \quad (5.5)$$

The cost function (5.6) in the output layer is the mean squared differences between the DBNN predicted image and the true DFN image.

$$C = \sum_{i=1}^n \frac{(y_i^{pred} - y_i^{true})^2}{n} \quad (5.6)$$

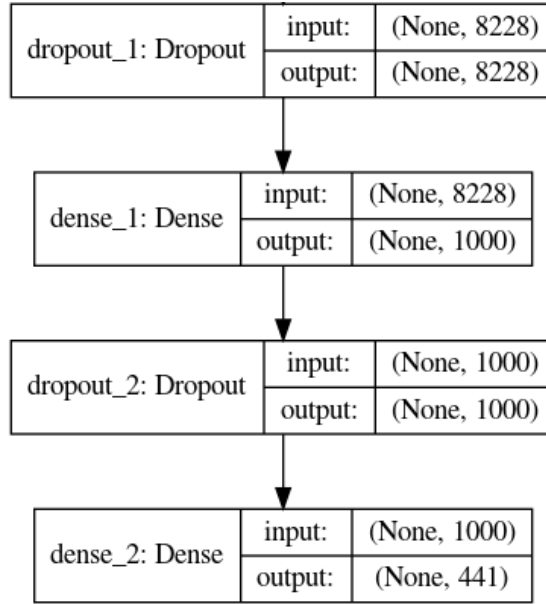


Figure 5.3. The architecture of the DBNN. The dropout is applied to both the input layer and hidden layer to avoid overfitting.

5.4 Examples

5.4.1 Simple example for DBI obtained by Born scattering

I performed the training based on the Keras (Chollet, 2015) and I used batch gradient descent and ADAM optimizer (Kingma and Ba, 2014) with a learning rate of 0.001 to train our neural network. I trained 5,000 epochs and the batch size in each epoch is 100. The cost function decreases rapidly in the first 500 iterations and gradually converges to an acceptable level. After training, I fed DBI from the test dataset into our trained neural network to make DFN predictions. I then compared

the true DFN and predicted DFN for input DBI from both training dataset and test dataset (Figure 5.5; Figure 5.6). For the training dataset, the predicted DFN's are almost the same as the true DFNs, which indicates that the DBNN has learned how to extract information in DBI pattern and translate it into DFN. For the test dataset, the DBNN also makes reasonable predictions with a comparable resolution of the training dataset.

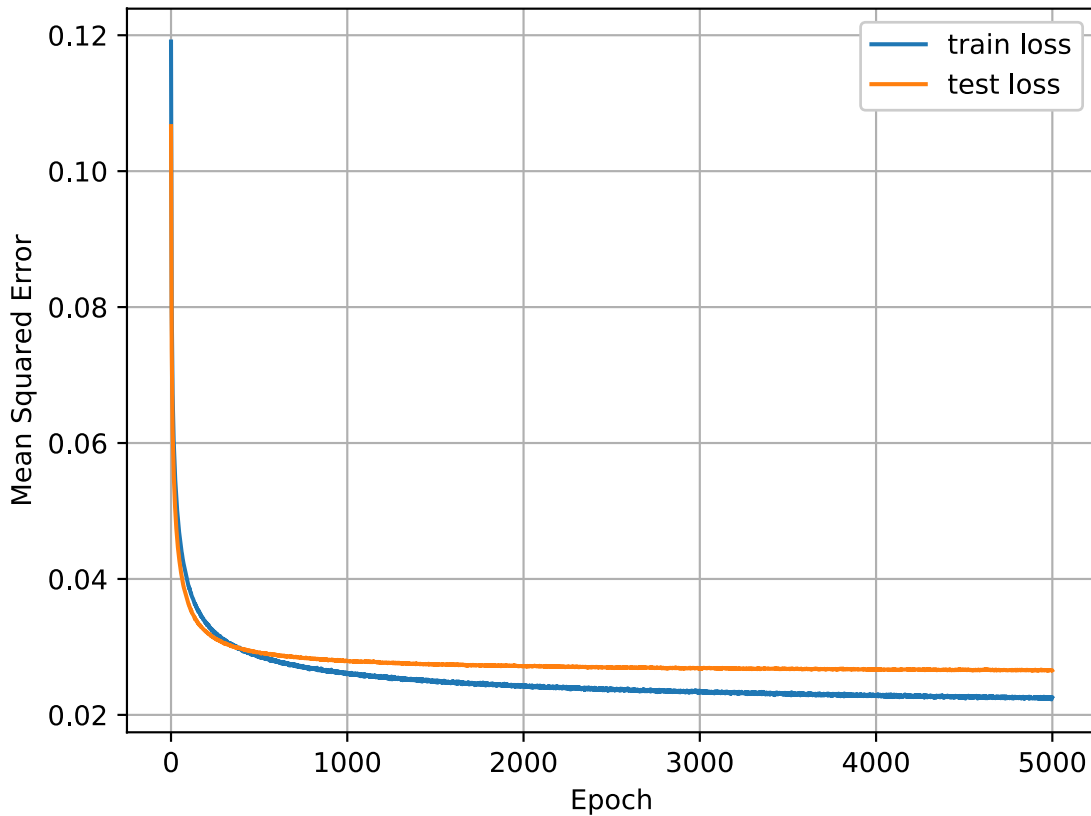


Figure 5.4. Mean square error of predictions for training dataset and test dataset in 5000 epochs during the training process.

I also trained a simpler regression model with no hidden layer, no dropout, and no activation. The regression model could generate predictions for DFNs which have a reasonable trend but relatively low resolution. The DBNN with one hidden layer and with dropout and activation has

much better resolution than the DBNN with no hidden layer and with no dropout and no activation (Figure 5.7; Figure 5.8).

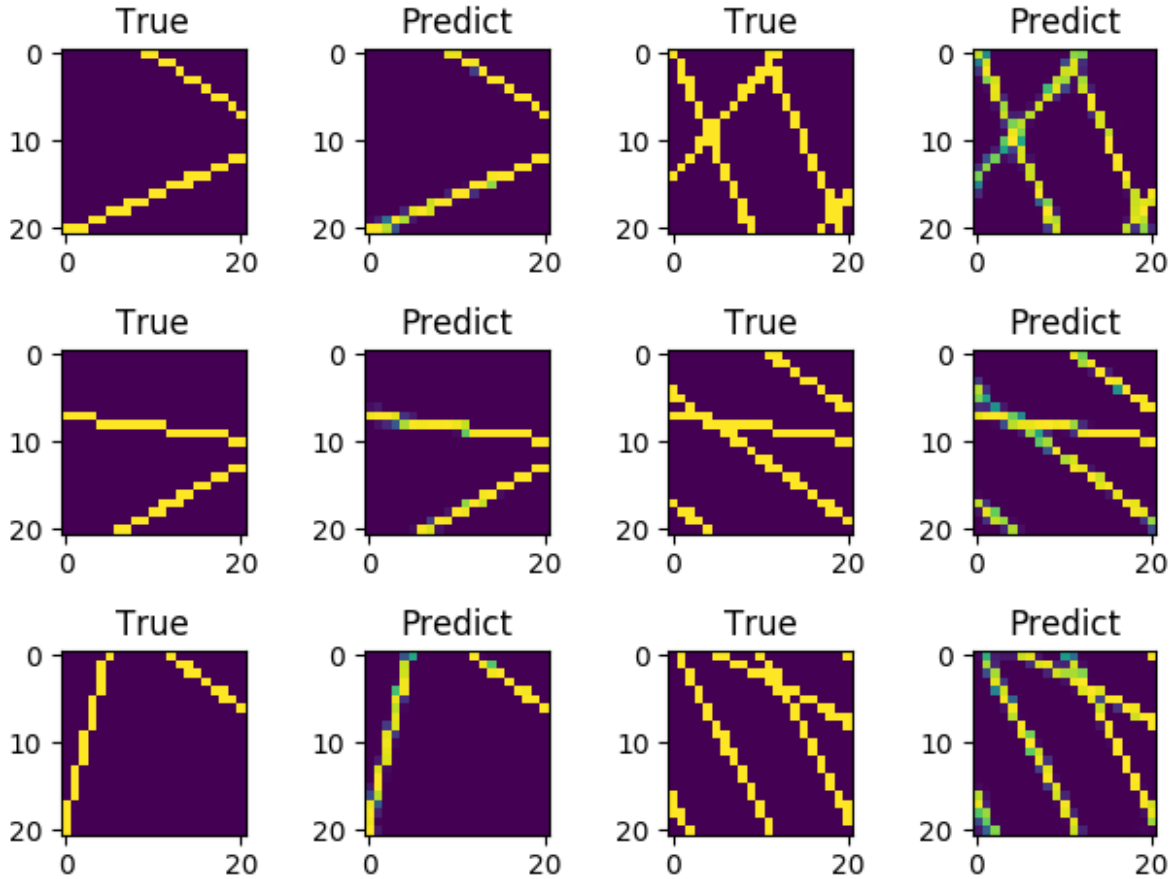


Figure 5.5. Comparison of predicted fractures and true fractures using training dataset for DBNN with one hidden layer, dropout, and activation. Yellow color represents fracture. Dark blue represents no fracture. Each fracture image has 21×21 pixels. And each pixel has a dimension of 5 meter by 5 meter.

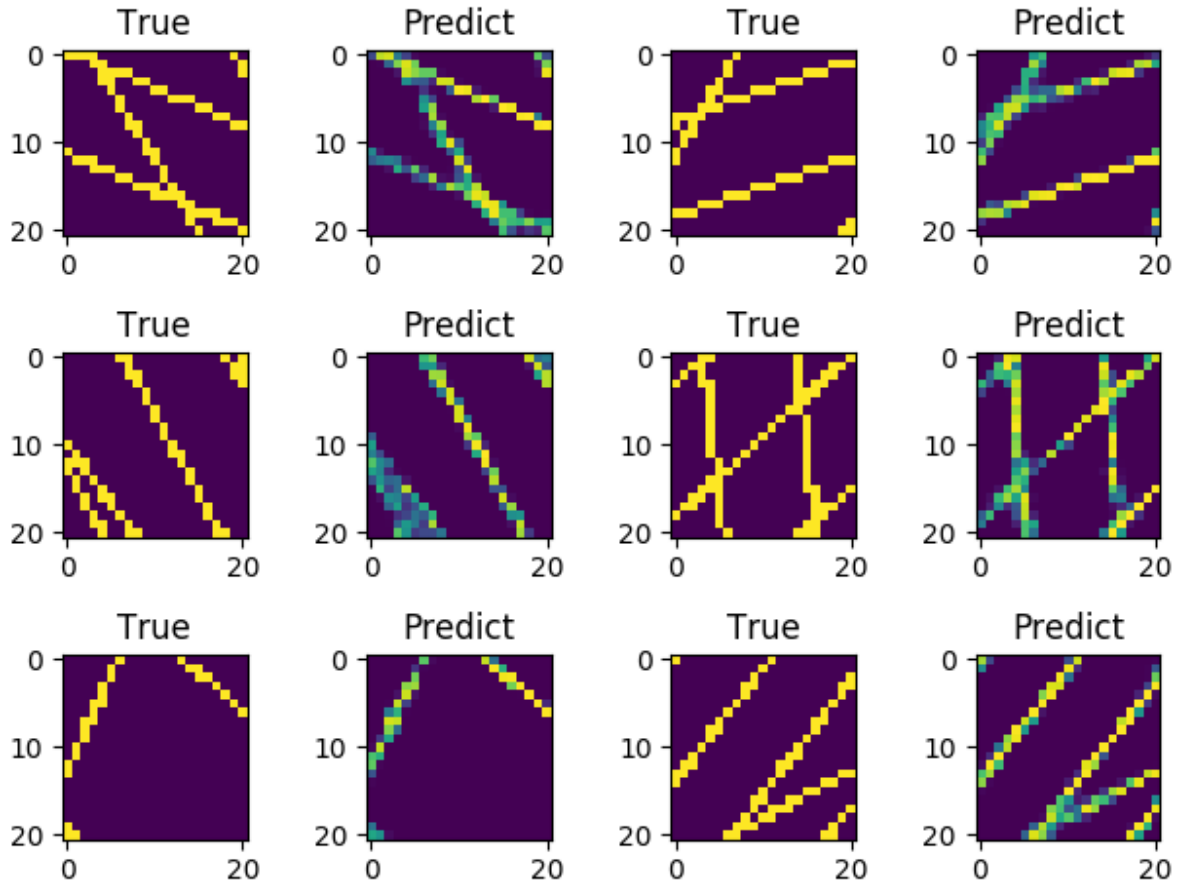


Figure 5.6. Comparison of predicted fractures and true fractures using test dataset for DBNN with one hidden layer, dropout, and activation. Yellow color represents fracture. Dark blue represents no fracture.

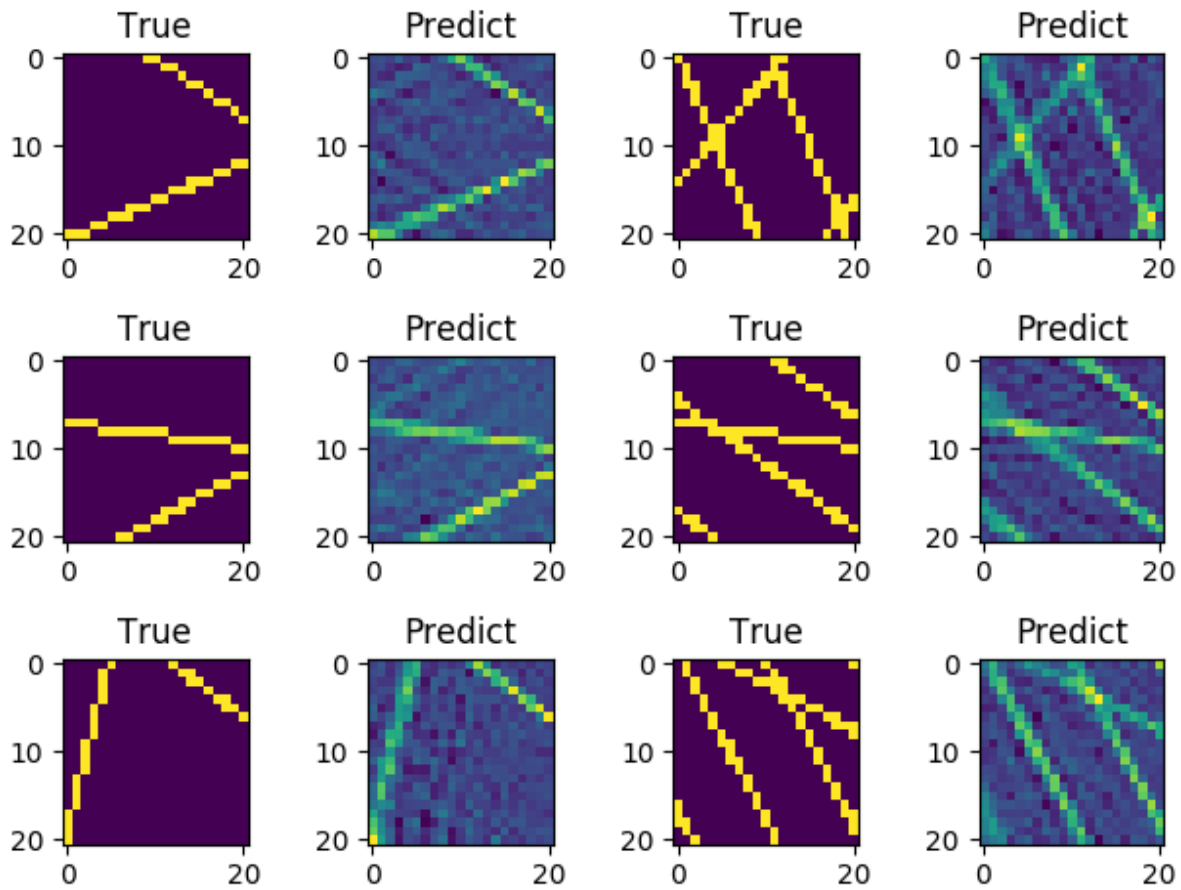


Figure 5.7. Comparison of predicted fractures and true fractures using training dataset for simpler regression DBNN model. Yellow color represents fracture. Dark blue represents no fracture.

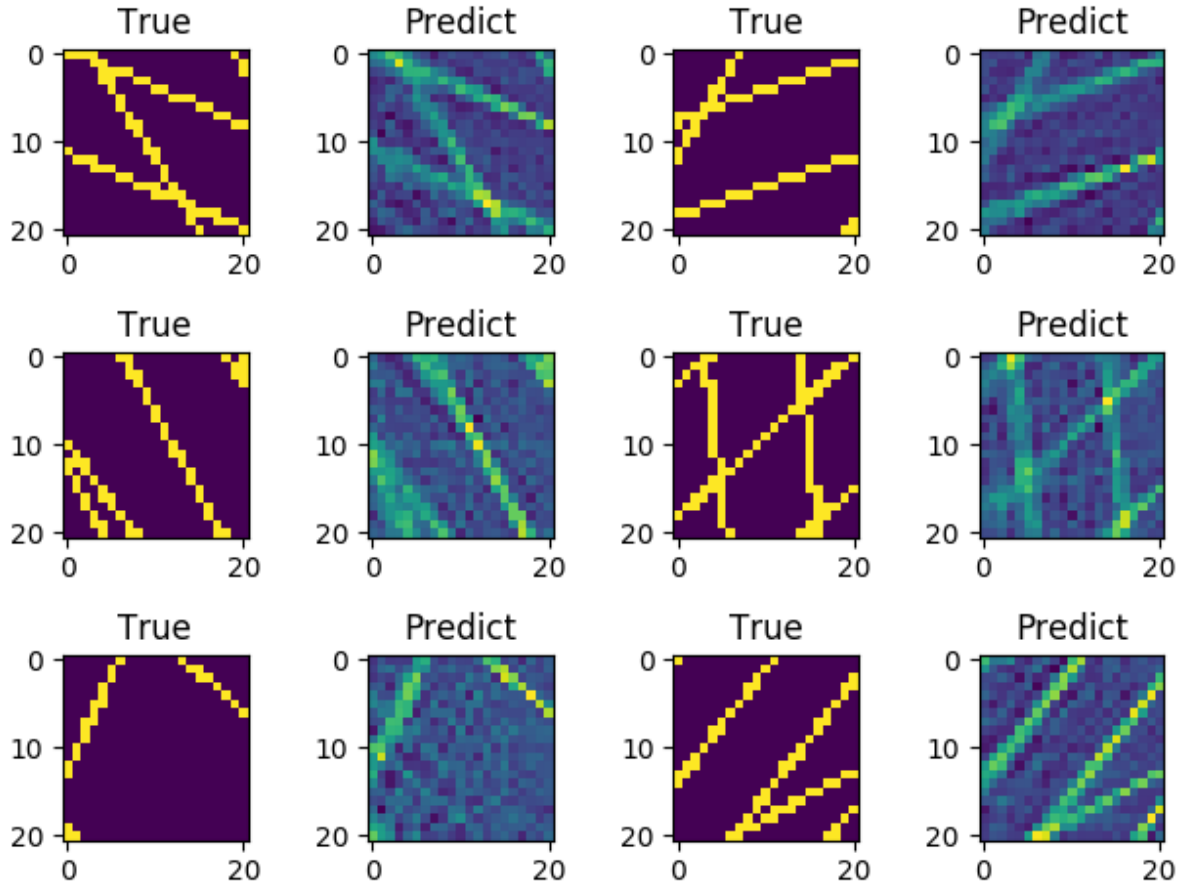


Figure 5.8. Comparison of predicted fractures and true fractures using test dataset for simpler regression DBNN model. Yellow color represents fracture. Dark blue represents no fracture.

5.4.2 Example for DBI obtained by finite-difference modeling

After I trained the neural network for DBI obtained by Born modeling, I would like to apply the trained neural network to a more realistic dataset for a more complex fracture system generated by 3-dimensional (3D) elastic finite-difference (FD) modeling. The significant difference between the FD modeling and Born modeling is that the FD modeling generates both single and multiple scatterings. We perform the 3D FD modeling for a layered model with two sets of randomly spaced vertical fractures embedded on the top of 3rd layer (Figure 5.9) (Hu *et al.*, 2018). The horizontal dimension of the fracture system is $2400m \times 2400m$ (Figure 5.9c). The whole fracture system is

divided into 21-by-21 $120m \times 120m$ target blocks. The DBI for each target block is obtained using the DB method. I then tried to predict the geometry of the fracture using the trained neural network.

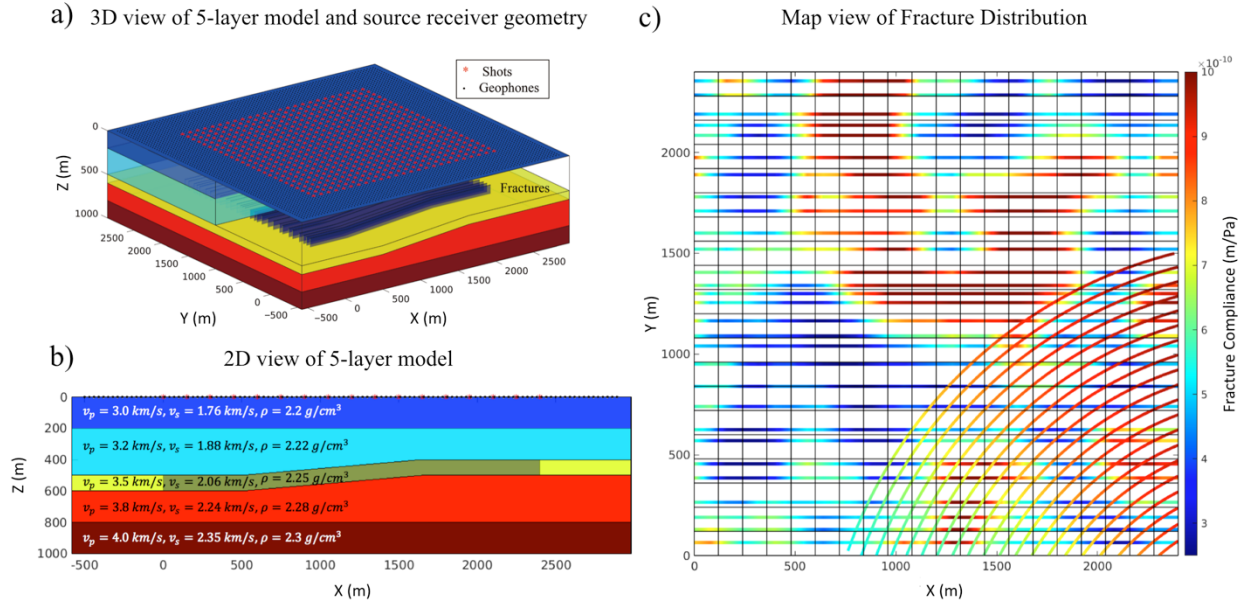


Figure 5.9 **a)** 3D view of 5-layer model for finite-difference modeling and source (red asterisks) and receiver (blue dots) geometry. Randomly spaced vertical fractures are located in a non-flat layer. **b)** 2D view of 5-layer model with P-wave velocity V_P , S-wave velocity V_S and density ρ . (Hu *et al.*, 2018) **c)** Map view of fracture distribution. The horizontal lines and circles are fractures. Red color represents high fracture compliance. Blue color represents low fracture compliance.

I fed the trained neural network with the DBI of each target block and try to predict the DFN for each block. I combined the DFN for all 441 target blocks to reconstruct the fracture system (Figure 5.10**b**). The predicted results clearly show two sets of fractures. However, compared with the true fracture distribution, the predicted locations for some fractures are not correct.

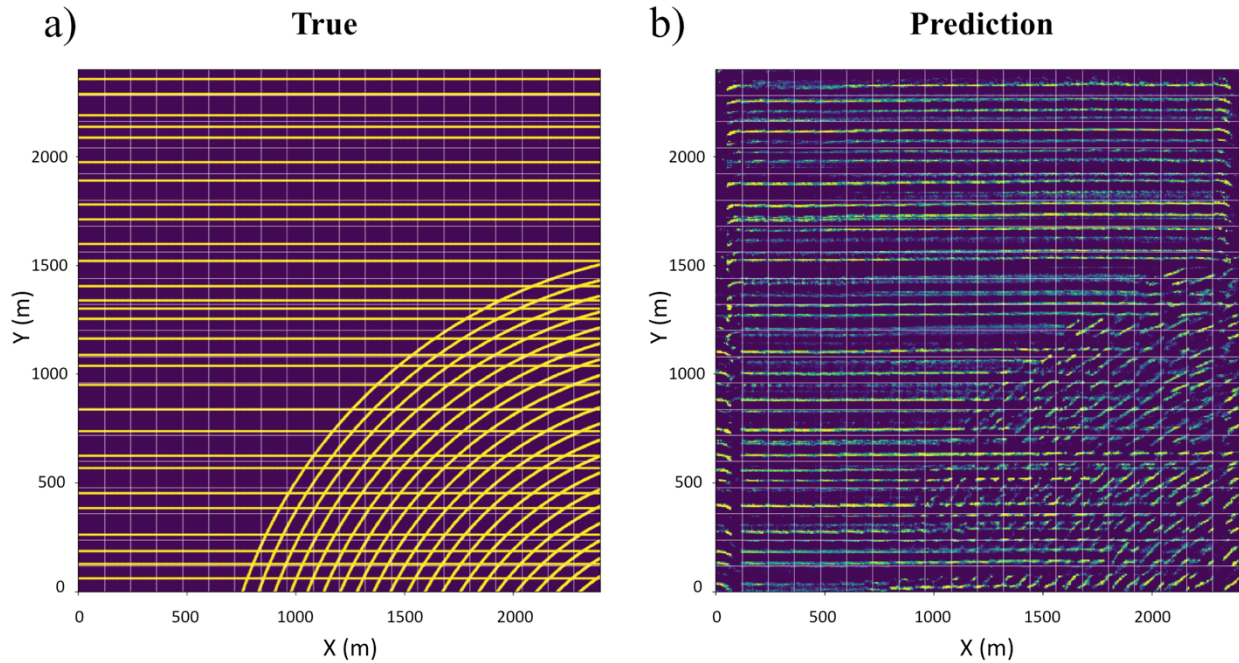


Figure 5.10 (a) True fracture distribution map (21-by-21 target blocks). Yellow color represents fractures. Dark blue represents no fracture. (b) Predicted fractures by trained neural network with DBIs obtained from FD modeling data as input.

5.5 Conclusions

I tested the feasibility of using double-beam neural network (DBNN) to directly transform complex-valued double-beam interference (DBI) patterns into discrete fracture networks (DFN) in order to achieve the detection of the fracture distribution on synthetic datasets. The trained neural network can make accurate and high-resolution predictions for the locations and geometries for multiple coexisting fracture sets. The results are promising. Besides the spacing and orientation readily obtained in the amplitude of the DBI pattern, the exact locations of fractures are also determined. I also applied the trained DBNN on DBI obtained from FD modeled dataset and successfully predict two sets of fractures. However, the predicted locations are not correct for some

fractures. More research needs to be done to improve the precision of detecting fracture distribution.

6 Bibliography

- Aki, K. (1973), Scattering of P waves under the Montana Lasa, *Journal of Geophysical Research*, **78**, 1334-1346.
- Aki, K., and K. L. Larner (1970), Surface motion of a layered medium having an irregular interface due to incident plane SH waves, *Journal of Geophysical Research (1896-1977)*, **75**, 933-954.
- Aki, K., and P. G. Richards (2002), *Quantitative seismology*, University Science Books.
- Allegre, C. J., and D. L. Turcotte (1986), Implications of a two-component marble-cake mantle, *Nature*, **323**, 123-127.
- Barton, C. A., D. Moos, and M. D. Zoback (1995), Fluid flow along potentially active faults in crystalline rock, *Geology*, **23**, 683-686.
- Bercovici, D. (2007), Mantle dynamics past, present, and future: an introduction and overview, in *Treatise on Geophysics*, edited by S. Gerald, vol. pp. 1-30 Vol. Series editor Elsevier, Amsterdam.
- Bina, C. R., and B. J. Wood (1987), Olivine-spinel transitions: Experimental and thermodynamic constraints and implications for the nature of the 400-km seismic discontinuity, *Journal of Geophysical Research: Solid Earth*, **92**, 4853-4866.
- Brownlee, S. J., B. R. Hacker, G. E. Harlow, and G. Seward (2013), Seismic signatures of a hydrated mantle wedge from antigorite crystal-preferred orientation (CPO), *Earth and Planetary Science Letters*, **375**, 395-407.
- Červený, V. (2002), Expansion of a Plane Wave into Gaussian Beams, *Stud Geophys Geod*, **46**, 43-54.

- Chang, S.-J., A. M. G. Ferreira, J. Ritsema, H. J. van Heijst, and J. H. Woodhouse (2015), Joint inversion for global isotropic and radially anisotropic mantle structure including crustal thickness perturbations, *Journal of Geophysical Research: Solid Earth*, **120**, 4278-4300.
- Chen, X., and K. Aki (1991), General coherence functions for amplitude and phase fluctuations in a randomly heterogeneous medium, *Geophys J Int*, **105**, 155-162.
- Cheng, C. H. (1993), Crack models for a transversely isotropic medium, *J Geophys Res-Sol Ea*, **98**, 675-684.
- Chernov, L. A. (1960), *Wave propagation in a random medium*, McGraw-Hill, New York.
- Chollet, F. (2015), *keras*, edited.
- Cormier, V., Y. Tian, and Y. Zheng (2018), Heterogeneity spectrum of Earth's upper mantle obtained from the coherence of teleseismic P waves, *Communications in Computational Physics*.
- Cormier, V. F. (2000), D " as a transition in the heterogeneity spectrum of the lowermost mantle, *J Geophys Res-Sol Ea*, **105**, 16193-16205.
- Crampin, S. (1985), Evaluation of anisotropy by shear-wave splitting, *Geophysics*, **50**, 142-152.
- Crampin, S., and S. Peacock (2008), A review of the current understanding of seismic shear-wave splitting in the Earth's crust and common fallacies in interpretation, *Wave Motion*, **45**, 675-722.
- David, C., Y. Gueguen, and G. Pampoukis (1990), Effective medium theory and network theory applied to the transport-properties of rock, *J Geophys Res-Solid*, **95**, 6993-7005.
- Dziewonski, A. M., and D. L. Anderson (1981), Preliminary reference Earth model, *Physics of the Earth and Planetary Interiors*, **25**, 297-356.
- Dziewonski, A. M., T. A. Chou, and J. H. Woodhouse (1981), Determination of earthquake source parameters from waveform data for studies of global and regional seismicity, *Journal of Geophysical Research: Solid Earth*, **86**, 2825-2852.

- Eakin, C. M., M. D. Long, A. Scire, S. L. Beck, L. S. Wagner, G. Zandt, and H. Tavera (2016), Internal deformation of the subducted Nazca slab inferred from seismic anisotropy, *Nature Geoscience*, **9**, 56-+.
- Eakin, C. M., M. D. Long, L. S. Wagner, S. L. Beck, and H. Tavera (2015), Upper mantle anisotropy beneath Peru from SKS splitting: constraints on flat slab dynamics and interaction with the Nazca Ridge, *Earth and Planetary Science Letters*, **412**, 152-162.
- Efron, B., and R. J. Tibshirani (1994), *An Introduction to the Bootstrap*, Taylor & Francis.
- Ekström, G., M. Nettles, and A. M. Dziewonski (2012), The global CMT project 2004-2010: Centroid-moment tensors for 13,017 earthquakes, *Phys. Earth Planet. Inter.*, **200**, 1-9.
- Evison, F. F. (1963), Earthquakes and faults, *B Seismol Soc Am*, **53**, 873.
- Fang, X., M. C. Fehler, Z. Zhu, Y. Zheng, and D. R. Burns (2013), Reservoir fracture characterization from seismic scattered waves, *Geophys J Int.*
- Fang, X., Y. Zheng, and M. Fehler (2017), Fracture clustering effect on amplitude variation with offset and azimuth analyses, *Geophysics*, **82**, N13-N25.
- Far, M. E., B. Hardage, and D. Wagner (2014), Fracture parameter inversion for Marcellus Shale, *Geophysics*, **79**, C55-C63.
- Farley, K. A., J. H. Natland, and H. Craig (1992), Binary mixing of enriched and undegassed (primitive?) mantle components (He, Sr, Nd, Pb) in Samoan lavas, *Earth and Planetary Science Letters*, **111**, 183-199.
- Frohlich, C. (1990), Note concerning non-double-couple source components from slip along surfaces of revolution, *Journal of Geophysical Research: Solid Earth (1978–2012)*, **95**, 6861-6866.
- Frohlich, C. (1994), Earthquakes with non-double-couple mechanisms, *Science*, **264**, 804-809.

- Frohlich, C. (2006), *Deep earthquakes*, Cambridge University Press.
- Frohlich, C., and S. D. Davis (1999), How well constrained are well-constrained T, B, and P axes in moment tensor catalogs?, *Journal of Geophysical Research: Solid Earth (1978–2012)*, **104**, 4901-4910.
- Fukao, Y., and M. Obayashi (2013), Subducted slabs stagnant above, penetrating through, and trapped below the 660 km discontinuity, *Journal of Geophysical Research: Solid Earth*, **118**, 5920-5938.
- Gale, J., R. Reed, and J. Holder (2007), Natural fractures in the Barnett Shale and their importance for hydraulic fracture treatments, 603-622 pp.
- Gilbert, F. (1971), Excitation of the normal modes of the earth by earthquake sources, *Geophys J Roy Astr S*, **22**, 223-226.
- Goff, J. A., K. Holliger, and A. Levander (1994), Modal fields: A new method for characterization of random seismic velocity heterogeneity, *Geophysical Research Letters*, **21**, 493-496.
- Green, H. W. (2007), Shearing instabilities accompanying high-pressure phase transformations and the mechanics of deep earthquakes, *Proceedings of the National Academy of Sciences of the United States of America*, **104**, 9133-9138.
- Green, H. W., 2nd, W. P. Chen, and M. R. Brudzinski (2010), Seismic evidence of negligible water carried below 400-km depth in subducting lithosphere, *Nature*, **467**, 828-831.
- Gudmundsson, Ó., and M. Sambridge (1998), A regionalized upper mantle (RUM) seismic model, *Journal of Geophysical Research: Solid Earth (1978–2012)*, **103**, 7121-7136.
- Hacker, B. R., S. M. Peacock, G. A. Abers, and S. D. Holloway (2003), Subduction factory 2. Are intermediate-depth earthquakes in subducting slabs linked to metamorphic dehydration reactions?, *Journal of Geophysical Research: Solid Earth*, **108**.

- Hart, S. R. (1988), Heterogeneous mantle domains: signatures, genesis and mixing chronologies, *Earth and Planetary Science Letters*, **90**, 273-296.
- Haskell, N. A. (1953), The dispersion of surface waves on multilayered media, *B Seismol Soc Am*, **43**, 17-34.
- Haugland, S. M., J. Ritsema, P. E. van Keken, and T. Nissen-Meyer (2018), Analysis of PKP scattering using mantle mixing simulations and axisymmetric 3D waveforms, *Physics of the Earth and Planetary Interiors*, **276**, 226-233.
- Helnwein, P. (2001), Some remarks on the compressed matrix representation of symmetric second-order and fourth-order tensors, *Computer Methods in Applied Mechanics and Engineering*, **190**, 2753-2770.
- Henry, C., J. H. Woodhouse, and S. Das (2002), Stability of earthquake moment tensor inversions: effect of the double-couple constraint, *Tectonophysics*, **356**, 115-124.
- Hill, N. R. (1990), Gaussian beam migration, *Geophysics*, **55**, 1416-1428.
- Holyoke, C. W., A. K. Kronenberg, J. Newman, and C. Ulrich (2014), Rheology of magnesite, *J Geophys Res-Sol Ea*, **119**, 6534-6557.
- Houston, H. (2015), Deep earthquakes, in *Treatise on Geophysics*, edited, vol. pp. 329-354 Vol. Series editor Elsevier, Amsterdam.
- Hu, H., and Y. Zheng (2017), 3D Seismic characterization of fractures in a dipping reservoir layer by double beams, *SEG Expanded Abstracts*.
- Hu, H., and Y. Zheng (2018), 3D seismic characterization of fractures in a dipping layer using the double-beam method, *Geophysics*, **83**, V123-V134.
- Hu, H., Y. Zheng, X. Fang, and M. C. Fehler (2018), 3D seismic characterization of fractures with random spacing using the double-beam method, *Geophysics*, **83**, M63-M74.

- Hu, J. S., M. Faccenda, and L. J. Liu (2017), Subduction-controlled mantle flow and seismic anisotropy in South America, *Earth and Planetary Science Letters*, **470**, 13-24.
- Hubbert, M. K., and D. G. Willis (1957), Mechanics of hydraulic fracturing, *T Am I Min Met Eng*, **210**, 153-163.
- Hunt, D. L., and L. H. Kellogg (2001), Quantifying mixing and age variations of heterogeneities in models of mantle convection: Role of depth-dependent viscosity, *J Geophys Res-Sol Ea*, **106**, 6747-6759.
- Ishimaru, A. (1991), Wave propagation and scattering in random media and rough surfaces, *Proceedings of the IEEE*, **79**, 1359-1366.
- Jiang, G., D. Zhao, and G. Zhang (2008), Seismic evidence for a metastable olivine wedge in the subducting Pacific slab under Japan Sea, *Earth and Planetary Science Letters*, **270**, 300-307.
- Johnston, D. E., and C. A. Langston (1984), The effect of assumed source structure on inversion of earthquake source parameters - the Eastern Hispaniola earthquake of 14 September 1981, *B Seismol Soc Am*, **74**, 2115-2134.
- Julian, B. R., A. D. Miller, and G. R. Foulger (1998), Non-double-couple earthquakes 1. Theory, *Reviews of Geophysics*, **36**, 525-549.
- Jung, H., W. Mo, and H. W. Green (2009), Upper mantle seismic anisotropy resulting from pressure-induced slip transition in olivine, *Nature Geoscience*, **2**, 73-77.
- Jung, H., M. Park, S. Jung, and J. Lee (2010), Lattice preferred orientation, water content, and seismic anisotropy of orthopyroxene, *Journal of Earth Science*, **21**, 555-568.
- Kaneshima, S. (1990), Origin of crustal anisotropy - shear-wave splitting studies in Japan, *J Geophys Res-Solid*, **95**, 11121-11133.

- Kang, P. K., M. Dentz, and R. Juanes (2011), Predictability of anomalous transport on lattice networks with quenched disorder, *Physical Review E*, **83**, 030101.
- Kang, P. K., Y. Zheng, X. Fang, R. Wojcik, D. McLaughlin, S. Brown, M. C. Fehler, D. R. Burns, and R. Juanes (2016), Sequential approach to joint flow-seismic inversion for improved characterization of fractured media, *Water Resources Research*, **52**, 903-919.
- Karato, S., H. Jung, I. Katayama, and P. Skemer (2008), Geodynamic significance of seismic anisotropy of the upper mantle: New insights from laboratory studies, *Annu Rev Earth Pl Sc*, **36**, 59-95.
- Kawakatsu, H., and S. Yoshioka (2011), Metastable olivine wedge and deep dry cold slab beneath southwest Japan, *Earth and Planetary Science Letters*, **303**, 1-10.
- Kawasaki, I., and T. Tanimoto (1981), Radiation patterns of body waves due to the seismic dislocation occurring in an anisotropic source medium, *B Seismol Soc Am*, **71**, 37-50.
- Kellogg, L. H., and D. L. Turcotte (1987), Homogenization of the mantle by convection mixing and diffusion, *Earth and Planetary Science Letters*, **81**, 371-378.
- Kellogg, L. H., and D. L. Turcotte (1990), Mixing and the distribution of heterogeneities in a chaotically convecting mantle, *Journal of Geophysical Research*, **95**, 421-432.
- Kingma, D. P., and J. Ba (2014), Adam: a method for stochastic optimization, *CoRR*, **abs/1412.6980**.
- Kirby, S. H. (1987), Localized polymorphic phase transformations in high-pressure faults and applications to the physical mechanism of deep earthquakes, *Journal of Geophysical Research: Solid Earth* (1978-2012), **92**, 13789-13800.

- Kirby, S. H., S. Stein, E. A. Okal, and D. C. Rubie (1996), Metastable mantle phase transformations and deep earthquakes in subducting oceanic lithosphere, *Reviews of Geophysics*, **34**, 261-306.
- Kirkpatrick, S. (1984), Optimization by simulated annealing: Quantitative studies, *Journal of Statistical Physics*, **34**, 975-986.
- Kirkpatrick, S., C. D. Gelatt, and M. P. Vecchi (1983), Optimization by simulated annealing, *Science*, **220**, 671-680.
- Knopoff, L., and M. J. Randall (1970), The compensated linear-vector dipole: A possible mechanism for deep earthquakes, *Journal of Geophysical Research*, **75**, 4957-4963.
- Kubo, A., E. Fukuyama, H. Kawai, and K. i. Nonomura (2002), NIED seismic moment tensor catalogue for regional earthquakes around Japan: quality test and application, *Tectonophysics*, **356**, 23-48.
- Kuge, K., and H. Kawakatsu (1993), Significance of non-double couple components of deep and intermediate-depth earthquakes: implications from moment tensor inversions of long-period seismic waves, *Physics of the Earth and Planetary Interiors*, **75**, 243-266.
- Kuge, K., and T. Lay (1994), Systematic non-double-couple components of earthquake mechanisms: The role of fault zone irregularity, *Journal of Geophysical Research: Solid Earth*, **99**, 15457-15467.
- Landa, E., A. Klokov, and R. Baina (2011), Point and edge diffractions in three dimensions, 73rd EAGE Conference and Exhibition incorporating SPE EUROPEC 2011,
- Leonard, M. (2010), Earthquake fault scaling: self-consistent relating of rupture length, width, average displacement, and moment release, *B Seismol Soc Am*, **100**, 1971-1988.

- Levander, A., R. W. England, S. K. Smith, R. W. Hobbs, J. A. Goff, and K. Holliger (1994), Stochastic characterization and seismic response of upper and middle crustal rocks based on the Lewisian gneiss complex, Scotland, *Geophys J Int*, **119**, 243-259.
- Levin, V., J. Park, M. Brandon, J. Lees, V. Peyton, E. Gordeev, and A. Ozerov (2002), Crust and upper mantle of Kamchatka from teleseismic receiver functions, *Tectonophysics*, **358**, 233-265.
- Li, J., H. Hu, and Y. Zheng (2019), Physics-guided machine learning identification of discrete fractures from double beam images, in *SEG Technical Program Expanded Abstracts 2019*, edited, vol. pp. 2433-2437 Vol. Series editor.
- Li, J., and Y. Zheng (2019), Generation of a stochastic binary field that fits a given heterogeneity power spectrum, *Geophys J Int*, **217**, 294-300.
- Li, J., Y. Zheng, L. Thomsen, T. J. Lapen, and X. Fang (2018), Deep earthquakes in subducting slabs hosted in highly anisotropic rock fabric, *Nature Geoscience*, **11**, 696-700.
- Lloyd, S. P. (1982), Least squares quantization in PCM, *IEEE Trans. Information Theory*, **28**, 129-136.
- Long, M. D. (2013), Constraints on subduction geodynamics from seismic anisotropy, *Reviews of Geophysics*, **51**, 76-112.
- Long, M. D., and T. W. Becker (2010), Mantle dynamics and seismic anisotropy, *Earth and Planetary Science Letters*, **297**, 341-354.
- Long, M. D., C. B. Biryol, C. M. Eakin, S. L. Beck, L. S. Wagner, G. Zandt, E. Minaya, and H. Tavera (2016), Overriding plate, mantle wedge, slab, and slab contributions to seismic anisotropy beneath the northern Central Andean Plateau, *Geochem Geophys Geosy*, **17**, 2556-2575.

- Long, M. D., and P. G. Silver (2008), The subduction zone flow field from seismic anisotropy: A global view, *Science*, **319**, 315-318.
- Long, M. D., and P. G. Silver (2009), Shear wave splitting and mantle anisotropy: measurements, interpretations, and new directions, *Surveys in Geophysics*, **30**, 407-461.
- Lynner, C., and M. D. Long (2014), Sub-slab anisotropy beneath the Sumatra and circum-Pacific subduction zones from source-side shear wave splitting observations, *Geochemistry, Geophysics, Geosystems*, **15**, 2262-2281.
- Lynner, C., and M. D. Long (2015), Heterogeneous seismic anisotropy in the transition zone and uppermost lower mantle: evidence from South America, Izu-Bonin and Japan, *Geophys J Int*, **201**, 1545-1552.
- Lynner, C., M. D. Long, C. J. Thissen, K. Paczkowski, and L. G. J. Montesi (2017), Evaluating geodynamic models for sub-slab anisotropy: Effects of olivine fabric type, *Geosphere*, **13**, 247-259.
- Mainprice, D., and B. Ildefonse (2009), Seismic anisotropy of subduction zone minerals-contribution of hydrous phases, *Front Earth Sci Ser*, 63-+.
- Mallick, S., and L. N. Frazer (1991), Reflection/transmission coefficients and azimuthal anisotropy in marine seismic studies, *Geophys J Int*, **105**, 241-252.
- Montgomery, C. T., and M. B. Smith (2010), Hydraulic fracturing: History of an enduring technology, *Journal of Petroleum Technology*, **62**, 26-40.
- Muller, G., M. Roth, and M. Korn (1992), Seismic-wave traveltimes in random media, *Geophys J Int*, **110**, 29-41.

- Nakajima, J., and A. Hasegawa (2004), Shear-wave polarization anisotropy and subduction-induced flow in the mantle wedge of northeastern Japan, *Earth and Planetary Science Letters*, **225**, 365-377.
- Nelson, R. A. (2001), Geologic analysis of naturally fractured reservoirs, 2nd ed., in *Geologic Analysis of Naturally Fractured Reservoirs (Second edition)*, edited by R. A. Nelson, vol. pp. 101-124 Vol. Series editor Gulf Professional Publishing, Woburn.
- Nick, H. M., A. Paluszny, M. J. Blunt, and S. K. Matthai (2011), Role of geomechanically grown fractures on dispersive transport in heterogeneous geological formations, *Physical Review E*, **84**, 056301.
- Nowacki, A., J. M. Kendall, J. Wookey, and A. Pemberton (2015), Mid-mantle anisotropy in subduction zones and deep water transport, *Geochemistry, Geophysics, Geosystems*, **16**, 764-784.
- Olson, J. (1989), Inferring paleostresses from natural fracture patterns - a new method, *Geology*, **17**, 345-348.
- Peng, X. (2019), Fracture characterization using multicomponent elastic waves, Master thesis, University of Houston, Houston.
- Raleigh, C. B., and M. S. Paterson (1965), Experimental deformation of serpentinite and its tectonic implications, *Journal of Geophysical Research*, **70**, 3965-3985.
- Randall, M. J., and L. Knopoff (1970), The mechanism at the focus of deep earthquakes, *Journal of Geophysical Research*, **75**, 4965-4976.
- Rayleigh, L. (1907), On the dynamical theory of gratings, *Proceedings of the Royal Society of London. Series A, Containing Papers of a Mathematical and Physical Character*, **79**, 399-416.

- Richardson, E., and T. H. Jordan (2002), Low-frequency properties of intermediate-tocus earthquakes, *B Seismol Soc Am*, **92**, 2434-2448.
- Romanowicz, B. (2003), Global mantle tomography: Progress status in the past 10 years, *Annu Rev Earth Pl Sc*, **31**, 303-328.
- Romanowicz, B. (2018), A deep-earthquake puzzle resolved, *Nature Geoscience*.
- Sanborn, C. J., V. F. Cormier, and M. Fitzpatrick (2017), Combined effects of deterministic and statistical structure on high-frequency regional seismograms, *Geophys J Int*, **210**, 1143-1159.
- Satake, K. (1985), Effects of station coverage on moment tensor inversion, *B Seismol Soc Am*, **75**, 1657-1667.
- Sato, H., and M. Fehler (1998), *Seismic wave propagation and scattering in the heterogeneous Earth*, Springer-Verlag, New York.
- Schoepp, A., S. Labonte, and E. Landa (2015), Multifocusing 3D diffraction imaging for detection of fractured zones in mudstone reservoirs: Case history, *Interpretation-J Sub*, **3**, Sf31-Sf42.
- Scholer, M., J. Irving, and K. Holliger (2010), Estimation of the correlation structure of crustal velocity heterogeneity from seismic reflection data, *Geophys J Int*, **183**, 1408-1428.
- Schubnel, A., F. Brunet, N. Hilairet, J. Gasc, Y. Wang, and H. W. Green (2013), Deep-focus earthquake analogs recorded at high pressure and temperature in the laboratory, *Science*, **341**, 1377.
- Shimizu, K., A. E. Saal, C. E. Myers, A. N. Nagle, E. H. Hauri, D. W. Forsyth, V. S. Kamenetsky, and Y. L. Niu (2016), Two-component mantle melting-mixing model for the generation of mid-ocean ridge basalts: Implications for the volatile content of the Pacific upper mantle, *Geochim Cosmochim Ac*, **176**, 44-80.

- Silver, P. G., and W. W. Chan (1991), Shear wave splitting and subcontinental mantle deformation, *Journal of Geophysical Research: Solid Earth*, **96**, 16429-16454.
- Silvestrov, I., R. Baina, and E. Landa (2016), Poststack diffraction imaging using reverse-time migration, *Geophys Prospect*, **64**, 129-142.
- Smith, G. P., D. A. Wiens, K. M. Fischer, L. M. Dorman, S. C. Webb, and J. A. Hildebrand (2001), A complex pattern of mantle flow in the Lau backarc, *Science*, **292**, 713.
- Song, T.-R. A., and H. Kawakatsu (2012), Subduction of oceanic asthenosphere: Evidence from sub-slab seismic anisotropy, *Geophysical Research Letters*, **39**.
- Srivastava, N., G. Hinton, A. Krizhevsky, I. Sutskever, and R. Salakhutdinov (2014), Dropout: a simple way to prevent neural networks from overfitting, *J. Mach. Learn. Res.*, **15**, 1929-1958.
- Stagno, V., Y. Tange, N. Miyajima, C. A. McCammon, T. Irifune, and D. J. Frost (2011), The stability of magnesite in the transition zone and the lower mantle as function of oxygen fugacity, *Geophysical Research Letters*, **38**, L19309.
- Stixrude, L., and C. Lithgow-Bertelloni (2012), Geophysics of chemical heterogeneity in the mantle, *Annu Rev Earth Pl Sc*, **40**, 569-595.
- Syracuse, E. M., P. E. van Keken, and G. A. Abers (2010), The global range of subduction zone thermal models, *Physics of the Earth and Planetary Interiors*, **183**, 73-90.
- Tada, T., and K. Shimazaki (1994), How much does a high-velocity slab contribute to the apparent non-double-couple components in deep-focus earthquakes, *B Seismol Soc Am*, **84**, 1272-1278.
- Tatham, R. H., M. D. Matthews, K. K. Sekharan, C. J. Wade, and L. M. Liro (1992), A physical model study of shear-wave splitting and fracture intensity, *Geophysics*, **57**, 647-652.
- Thomsen, L. (1986), Weak elastic anisotropy, *Geophysics*, **51**, 1954-1966.

- Thomsen, L. (1995), Elastic anisotropy due to aligned cracks in porous rock, *Geophys Prospect*, **43**, 805-829.
- Thomsen, L. (1999), Converted-wave reflection seismology over inhomogeneous, anisotropic media, *Geophysics*, **64**, 678-690.
- Thomson, A. R., M. J. Walter, S. C. Kohn, and R. A. Brooker (2016), Slab melting as a barrier to deep carbon subduction, *Nature*, **529**, 76-+.
- van Keken, P. E., E. H. Hauri, and C. J. Ballentine (2002), Mantle mixing: The generation, preservation, and destruction of chemical heterogeneity, *Annu Rev Earth Pl Sc*, **30**, 493-525.
- Vasconcelos, I., and V. Grechka (2007), Seismic characterization of multiple fracture sets at Rulison Field, Colorado, *Geophysics*, **72**, B19-B30.
- Vavrycuk, V. (2004), Inversion for anisotropy from non-double-couple components of moment tensors, *J Geophys Res-Sol Ea*, **109**.
- Vavrycuk, V. (2005), Focal mechanisms in anisotropic media, *Geophys J Int*, **161**, 334-346.
- Vavrycuk, V., P. Adamova, J. Doubravova, and H. Jakoubkova (2017), Moment tensor inversion based on the principal component analysis of waveforms: Method and application to microearthquakes in West Bohemia, Czech Republic, *Seismol Res Lett*, **88**, 1303-1315.
- Verdon, J. P., and A. Wustefeld (2013), Measurement of the normal/tangential fracture compliance ratio (ZN/ZT) during hydraulic fracture stimulation using S-wave splitting data, *Geophys Prospect*, **61**, 461-475.
- Vetri, L., E. Loinger, J. Gaiser, A. Grandi, and H. Lynn (2003), 3D/4C Emilio: Azimuth processing and anisotropy analysis in a fractured carbonate reservoir, *The Leading Edge*, **22**, 675-679.

- Veveakis, E., K. Regenauer-Lieb, and R. F. Weinberg (2015), Ductile compaction of partially molten rocks: the effect of non-linear viscous rheology on instability and segregation, *Geophys J Int*, **200**, 519-523.
- Vinnik, L., G. Kosarev, and L. I. Makeyeva (1984), Anisotropy in the lithosphere from the observations of SKS and SKKS *Proc. Acad. Sci. USSR* **278**, 1335-1339, (in Russian).
- Vinnik, L. P., and R. Kind (1993), Ellipticity of teleseismic S-particle motion, *Geophys J Int*, **113**, 165-174.
- Virieux, J. (1986), P-SV wave propagation in heterogeneous media: Velocity-stress finite-difference method, *Geophysics*, **51**, 889-901.
- Weinberg, R. F., E. Veveakis, and K. Regenauer-Lieb (2015), Compaction-driven melt segregation in migmatites, *Geology*, **43**, 471-474.
- Willis, M. E., D. R. Burns, R. Rao, B. Minsley, M. N. Toksoz, and L. Vetri (2006), Spatial orientation and distribution of reservoir fractures from scattered seismic energy, *Geophysics*, **71**, O43-O51.
- Winterstein, D. F. (1990), Velocity anisotropy terminology for geophysicists, *Geophysics*, **55**, 1070-1088.
- Woodhouse, J. H. (1981), The excitation of long period seismic waves by a source spanning a structural discontinuity, *Geophysical Research Letters*, **8**, 1129-1131.
- Wookey, J., J. M. Kendall, and G. Barruol (2002), Mid-mantle deformation inferred from seismic anisotropy, *Nature*, **415**, 777-780.
- Wu, R.-S., and S. M. Flatté (1990), Transmission fluctuations across an array and heterogeneities in the crust and upper mantle, in "Seismic Wave Scattering and Attenuation" ed. by Wu and Aki., *Pure Appl Geophys*, **132**, 175-196.

- Xu, W. B., C. Lithgow-Bertelloni, L. Stixrude, and J. Ritsema (2008), The effect of bulk composition and temperature on mantle seismic structure, *Earth and Planetary Science Letters*, **275**, 70-79.
- Yang, J., Z. Mao, J. F. Lin, and V. B. Prakapenka (2014), Single-crystal elasticity of the deep-mantle magnesite at high pressure and temperature, *Earth and Planetary Science Letters*, **392**, 292-299.
- Yeong, C. L. Y., and S. Torquato (1998), Reconstructing random media, *Physical Review E*, **57**, 495-506.
- Yuan, K., and C. Beghein (2013), Seismic anisotropy changes across upper mantle phase transitions, *Earth and Planetary Science Letters*, **374**, 132-144.
- Zhao, D. (2004), Global tomographic images of mantle plumes and subducting slabs: insight into deep Earth dynamics, *Physics of the Earth and Planetary Interiors*, **146**, 3-34.
- Zheng, Y., and R.-S. Wu (2005), Measurement of phase fluctuations for transmitted waves in random media, *Geophysical Research Letters*, **32**, L14314.
- Zheng, Y., and R. S. Wu (2008), Theory of transmission fluctuations in a depth-dependent background medium, in *Earth Heterogeneity and Scattering Effects on Seismic Waves*, edited by H. Sato and M. Fehler, vol. 50, pp. 21-41, *Advances in Geophysics*, Series Vol. 50 Series editor R. Dmowska.
- Zheng, Y. C., X. D. Fang, M. C. Fehler, and D. R. Burns (2013), Seismic characterization of fractured reservoirs by focusing Gaussian beams, *Geophysics*, **78**, A23-A28.
- Zhou, H.-w. (1990), Mapping of P-wave slab anomalies beneath the Tonga, Kermadec and New Hebrides arcs, *Physics of the Earth and Planetary Interiors*, **61**, 199-229.